

POLITECNICO DI TORINO

Master's Degree in Mechanical Engineering



In collaboration with **DELGROSSO**
S.R.L.

Master's Degree Thesis

Modeling and CFD analysis of an oil filter for automotive applications

Academic Supervisors

Prof. Massimo RUNDO

Eng. Paola FRESIA

Company Supervisors

Eng. Ivano NICASTRO

Eng. Eleonora PROCOPIO

Candidate

Luigi MASTAI

October 2021

Alla mia famiglia, ancora della mia vita.

Summary

Nowadays, the use of computational fluid dynamics (CFD) to predict internal or external flows behaviour of different components has sharply risen. Since it moves from analytical and empirical models to computer based simulations, CFD techniques span a wide range of industrial and non-industrial application areas.

The field of filtration process is part of CFD's investigations, because it is important to understand and solve pressure loss issues inside the filter element and increase the efficiency of filter medium. This master thesis aims to study the design and pressure drop prediction of an oil filter for automotive field, designed and created by CLEAN FILTERS DELGROSSO S.R.L. by simulation of flow pattern using CFD tool Considering that a simulation of the entire component results very challenging for computer's hardware capabilities, the fluid dynamic analysis has been divided into three steps for the sake of simplicity.

For each step, the goal of simulation was the pressure losses. The first part of the component to be simulated is the filter head, after that the filter medium is characterized and analyzed, and finally the perforated metal support is connected to the filter medium and investigated. The characterization of filter medium properties has been carried out through a porometer 3G and permeability measuring device (personally designed for the research). Following the definition of fluid dynamic model using SolidEdge with FloEFD extension, a parametric study has been performed in order to explore different geometric solutions. Finally, the results have been compared to experimental data provided by DELGROSSO S.R.L.

Future developments of this work could be the simulation of the whole filter and a microscopic particle study of contaminated oil through the filter medium fibers.

DELGROSSO
S.R.L.

Table of Contents

List of Tables	VI
List of Figures	VII
1 Introduction	1
1.1 Filtration	1
1.2 Contamination	2
1.3 Hydraulic fluids	3
1.4 Types of filters	4
2 Mechanical component: Oil Filter	6
2.1 Description	6
2.2 General working principle	8
2.3 Working fluid	10
3 Computational Fluid Dynamics	12
3.1 Governing Equations	13
3.1.1 Continuity equation	13
3.1.2 Momentum equation	14
3.1.3 Turbulence model	15
3.1.4 Darcy's Law	15
3.2 Finite volume method	16
4 Part I: Filter Head	17
4.1 Geometry	17
4.2 Domain	18
4.3 Boundary conditions	19
4.4 Mesh	20
4.5 Results	21
4.6 Parametric study	21

5	Part II: Filter Medium	25
5.1	Filter medium material	25
5.1.1	Depth filtration	27
5.2	Geometry	28
5.3	Properties of porous medium	32
5.3.1	Porosity	32
5.3.2	Permeability	35
5.4	Permeabilimeter	37
5.4.1	Working principle	42
5.4.2	Experimental results	44
5.4.3	Experiment simulation	46
5.5	Domain	53
5.6	Boundary Conditions	55
5.7	Mesh	55
5.8	Results	57
6	Part III: Perforated Support	66
6.1	Geometry	66
6.2	Domain	67
6.3	Boundary Conditions	69
6.4	Mesh	69
6.5	Results	76
7	Experimental test equipment	80
7.1	Description	80
7.2	Hydraulic circuit	82
7.3	Evaluation of experimental characteristics	82
7.3.1	Procedure	87
7.4	Data analysis	88
8	Conclusions	95
A	Operating fluid properties: AeroShell Fluid 41	96
B	Permeabilimeter: Technical drawings	100
C	How to import porosity and permeability parameters to FloEFD	105
	Bibliography	110

List of Tables

4.1	Mesh choice	20
4.2	Pressure losses sensitivity to parametric study	24
5.1	Experimental data summary (Source: DELGROSSO S.R.L. Porometer Data)	36
5.2	Microcal 20 DPC table sensitivity	39
5.3	Permeabilimeter experimental data (Source: DELGROSSO S.R.L. Permeabilimeter Data)	44
5.4	Mesh specifications of filter medium	57
6.1	Mesh specifications of perforated support case	71
7.1	Components of the hydraulic circuit S2	83

List of Figures

1.1	Full-flow oil system (Source: <i>Filters and Filtration Handbook</i>)	5
2.1	Oil filter components	7
2.2	Oil filter: Top view (left) and front section view (right)	8
2.3	Working principle of the oil filter	9
2.4	Aeroshell Fluid 41 properties	11
4.1	Filter head: Top view (left) and front section (right)	17
4.2	(a) Computational domain; (b) Fluid domain	18
4.3	Boundary conditions	19
4.4	Mesh independence study	20
4.5	Filter head mesh cut plot refinement	21
4.6	(a) Velocity distribution cut plot ; (b) Pressure distribution cut plot ; (c) Flow trajectory speed color plot	22
4.7	(a) Δp vs D_{hole} plot ; (b) Δp vs N_{holes} plot ; (c) Δp vs h plot	24
5.1	Pleated resin treated filter media	26
5.2	Depth filtration mechanisms (Source: <i>Handbook of Non-Woven Filter Media</i>)	28
5.3	Assembly of the filter element	29
5.4	Filter medium	31
5.5	Pore complexity (Source: <i>Handbook of Non-Woven Filter Media</i>)	33
5.6	Flow vs pressure data for measured wet and dry runs (Source: DELGROSSO S.R.L. Experimental Data)	34
5.7	Porometer 3G test bench	35
5.8	Air permeability test (Source: DELGROSSO S.R.L.)	37
5.9	Test bench of the permeabilimeter	38
5.10	Microcal 20 DPC	39
5.11	Permeabilimeter CAD model	40
5.12	Permeabilimeter exploded view	41
5.13	Section of syringe housing	42

5.14	Detail of the designed flanges	43
5.15	Permeability curve	45
5.16	Section view of the simulated permeabilimeter CAD model	47
5.17	Mesh refinement of the simulated permeabilimeter model	47
5.18	Simulated permeability curve	48
5.19	Cut plot of pressure gradient for the simulated permeabilimeter	48
5.20	Cut plot of flow trajectories for the simulated permeabilimeter	48
5.21	Comparison between the empirical curve and the simulated curve	49
5.22	Different media permeability curves; MEDIA 16 is the selected media	51
5.23	Zoomed view of cellulose media classification	52
5.24	Filter medium computational domain	53
5.25	Filter medium fluid domain	54
5.26	Filter medium CFD model in section and top view with boundary condition in evidence	58
5.27	Filter medium CFD model in section with isotropic porous media condition in evidence	59
5.28	Lateral and top views of the obtained auto-refined mesh	59
5.29	Additional bodies used to define local mesh regions (a) Ref.level = 6 , (b) Ref.level = 5, (c) Ref.level = 4	60
5.30	Plots of the mesh convergence study for filter medium: (a) Pressure loss in function of number of elements (b) Computational time in function of number of elements	61
5.31	Mesh Refinement	62
5.32	Filter medium velocity gradient cut plot	63
5.33	Filter medium pressure gradient cut plot	64
5.34	Filter medium flow trajectories	65
6.1	Perforated support of the real filter	67
6.2	Section of the perforated support	68
6.3	Section of the perforated support with filter medium	68
6.4	Perforated support computational domain	69
6.5	Section view of the perforated support fluid domain	70
6.6	Perforated support model in section and top view with boundary condition in evidence	72
6.7	Perforated support model in section and top view with boundary condition in evidence	73
6.8	Detail of mesh refinement of a hole	73
6.9	Solid bodies added as local mesh (a) Ref.level = 5, (b) Ref.level = 4	74

6.10	Plots of the mesh convergence study for perforated support case: (a) Pressure loss in function of number of elements (b) Computational time in function of number of elements	75
6.11	Perforated support case velocity gradient cut plot	77
6.12	Perforated support case pressure gradient cut plot	78
6.13	Velocity flow trajectories of the perforated support case	79
6.14	Zoom of fluid flow through a hole	79
7.1	DELGROSSO S.R.L Multipass Test bench	81
7.2	Hydraulic circuit S2 (Source: DELGROSSO S.R.L.)	85
7.3	Filter test workstation	86
7.4	Experimental Oil Filter	86
7.5	Filter 8×6 mm experimental curve	89
7.6	Filter 8×8 mm experimental curve	90
7.7	Filter 8×10 mm experimental curve	90
7.8	Experimental data vs Simulated data of filter 8×6 mm	91
7.9	Experimental data vs Simulated data of filter 8×8 mm	91
7.10	Experimental data vs Simulated data of filter 8×10 mm	92
7.11	Parametric comparison between experimental and simulated data at 100l/min	92
7.12	Parametric comparison between experimental and simulated data as a percentage	93
7.13	Pressure drop vs velocity of a single hole plot	94
C.1	Insert Porous Medium condition tool	106
C.2	Porous media: Create/Edit tool	107
C.3	Porous media: Inserting parameters	108
C.4	Porous media: Inserting permeability curve	109

Chapter 1

Introduction

1.1 Filtration

Generally, the word of *filtration* refers to a specific process of the general *separation* term, which describes the act of separating one or more distinct phases from another in a process which uses physical differences in the phases (such as particle size, density, etc.) [1]. Specifically, filtration is a separation procedure where solid contaminants are caught and separated from the working fluid. A filter is basically a device for separating one substance from another and to do that it requires the placing of a filter medium which must trap the solid particles in some way. Obviously, the filter must be designed in order to support the filter medium in the best way to achieve the desired purpose.

The technique of filtration is entirely based on particle size or droplet size (and partially on its shape), such that particles below the pore size of the filter medium will pass through it, while larger particles remain trapped. Filter designs rely on the ability to have high filter medium surface in a restricted volume. Filtration is a very widely used process, from the domestic sector (coffee filters) to the automotive sector (air, fuel, oil, coolant filters). Concerning the latter field, it is very important to protect hydraulic circuits and components from damaging contamination. For instance, abrasive particles could damage sensitive components like pumps, valves and motors. Without doubt, it is impossible to delete solid contamination completely, but thanks to filter devices it can be effectively controlled.

1.2 Contamination

Contaminants are normally present in all fluids, natural or artificial. When the level of contamination inside the fluid is higher than desired, it becomes compulsory to remove the impurities from the working fluid. In the automotive field many different types of contamination may be present, causing various problems in the hydraulic circuits.

These contaminants are [2]:

- Particulate (such as dust, dirt, sand, rust, fibers, elastomers);
- Wear metals, silicon and excessive additives (Al, Cr, Cu, Fe, Na, Zn, Ba, P);
- Water;
- Sealants;
- Corrosion products;
- Acids and other chemicals;

The impurities listed above, came from a high number of contaminated sources such as:

- New Hydraulic Fluid: even though new fluid is fresh from the drum, it is not clean. Its water content is typically 200 to 300 ppm;
- Primary contamination: caused during the manufacture, assembly and testing of hydraulic components;
- External contamination: dirt can enter the hydraulic fluid supply through leaking seals, reservoir breather caps, and worn cylinder rod seals;
- Induced: contaminants can enter the system during maintenance procedures;
- In-Operation: the major source of contamination come from the wear-generated contaminants from mechanical components;
- Replacement of failed components.

1.3 Hydraulic fluids

Hydraulic fluid is one of the most important aspect when considering filter component. The fluid is the vector that transmits energy within a fluid power circuit and provides lubrication and protection to the mechanical components inside the circuit. When selecting a new filter assembly, it is important to take into consideration the kind of fluid that is going to be filtered. For this purpose, a good classification of fluids is required. The most popular criterion of classification divides the fluids into the following families [3]:

- Mineral oils: commonly used oil deriving fluids;
- Fire resistant fluids: fluids with high flash point;
- Synthetic fluids: modified chemical products to obtain specific features;
- Ecological fluids: fluids with high biodegradability characteristics.

It is also important to think about the properties of a hydraulic fluid. These parameters can adversely affect the performance of the system, causing delay in the controls, excessive temperature rise, wear, efficiency reduction, etc. The main properties that characterize hydraulic fluids and affect their choice are:

- Lubricity: the property that keeps friction low and maintains an adequate film between moving parts;
- Density (ρ): the ratio of the mass of fluid to its volume. Mathematically, it is expressed as:

$$\rho = \frac{m}{V} \left[\frac{\text{kg}}{\text{m}^3} \right] \quad (1.1)$$

- Dynamic Viscosity (μ): the fluid's resistances to gradual deformation due to shear stresses;
- Kinematic Viscosity (ν): ratio of the viscosity of the fluid to its density. This value varies with temperature and pressure variations. Mathematically, it is expressed as:

$$\nu = \frac{\mu}{\rho} \left[\frac{\text{m}^2}{\text{s}} \right] \quad (1.2)$$

- Viscosity Index (VI): the ability to maintain viscosity when the temperature changes;
- Filter-ability Index (FI): the ability to cross the filter materials;

- Compressibility module (c_0): identifies the change in fluid volume with respect to the change in pressure at isothermal conditions;
- Wear protection: the ability to avoid corrosion of metal elements inside the system.

1.4 Types of filters

As mentioned in paragraph 1.1, filters cover a wide range of nowadays applications, hence it is impossible to have only one classification. Since the main object of this thesis is an oil filter, only the oleo-dynamic classification is considered. The common classification of filters is determined by their position in the plant [3]:

- Suction filters: positioned before the pump and responsible for protecting the pump from dirty contaminants;
- Delivery (or Pressure) filters: positioned between the pump and most sensitive regulating and controlling components, such as servo valves or proportional valves;
- Return filters: positioned on the return line to the tank;
- Combined filters: designed to be applied to systems with two or more circuits;
- Off-line filters: placed in a closed circuit independent from the main circuit (used in very large systems);
- Venting filters: positioned on the tank. Its function is to filter the air that enters the tank to compensate for fluid level variations.

In the Figure 1.1 is described a typical full-flow oil filtration system. It is in line between the pump and bearings, or other point to which the oil is distributed, this means that is a delivery filter circuit.

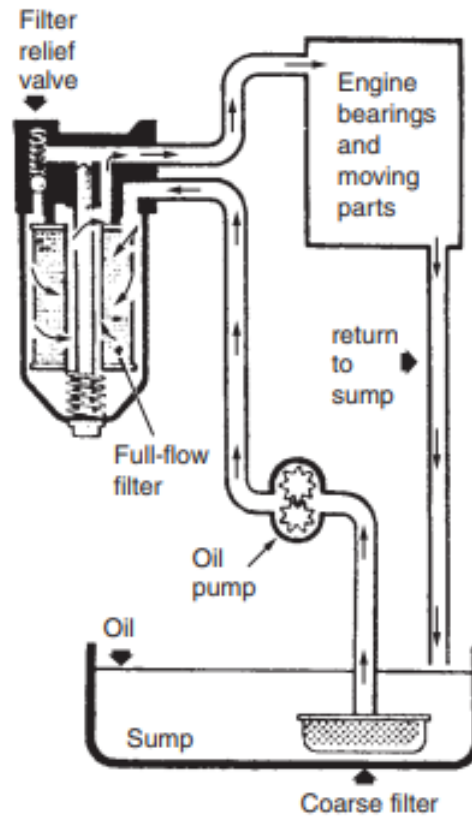


Figure 1.1: Full-flow oil system
(Source: *Filters and Filtration Handbook*)

Chapter 2

Mechanical component: Oil Filter

This chapter will describe briefly and in a simplified way, all the mechanical components and parameters that make up the analyzed oil filter and its working principle.

2.1 Description

The type of oil filter, object of this thesis, is the cartridge filter (Figure 2.1). This type of filter includes a cylindrical housing, in which there is a filter medium (the cartridge) [1]. Typically, the cartridge filter is installed as a unit, but when the continuity of fluid is essential, more than one cartridge in parallel is used (usually two for a duplex system). The component designed and developed by CLEAN FILTER DELGROSSO S.R.L is a full flow oil filter for automotive field. Figure 2.1 lists all of the components that make up the filter in question. Specifically:

1. Cylindrical housing
2. Pressure spring
3. Filter medium
4. Perforated metal support
5. Metal threaded plate ($G3/8$) with $N_{holes} = 8$ and $D_{hole} = 8$ mm

In addition to these components there is a gasket-bearing and, sometimes there is a by-pass valve. The reference CAD filter is shown in Figure 2.1 with filter

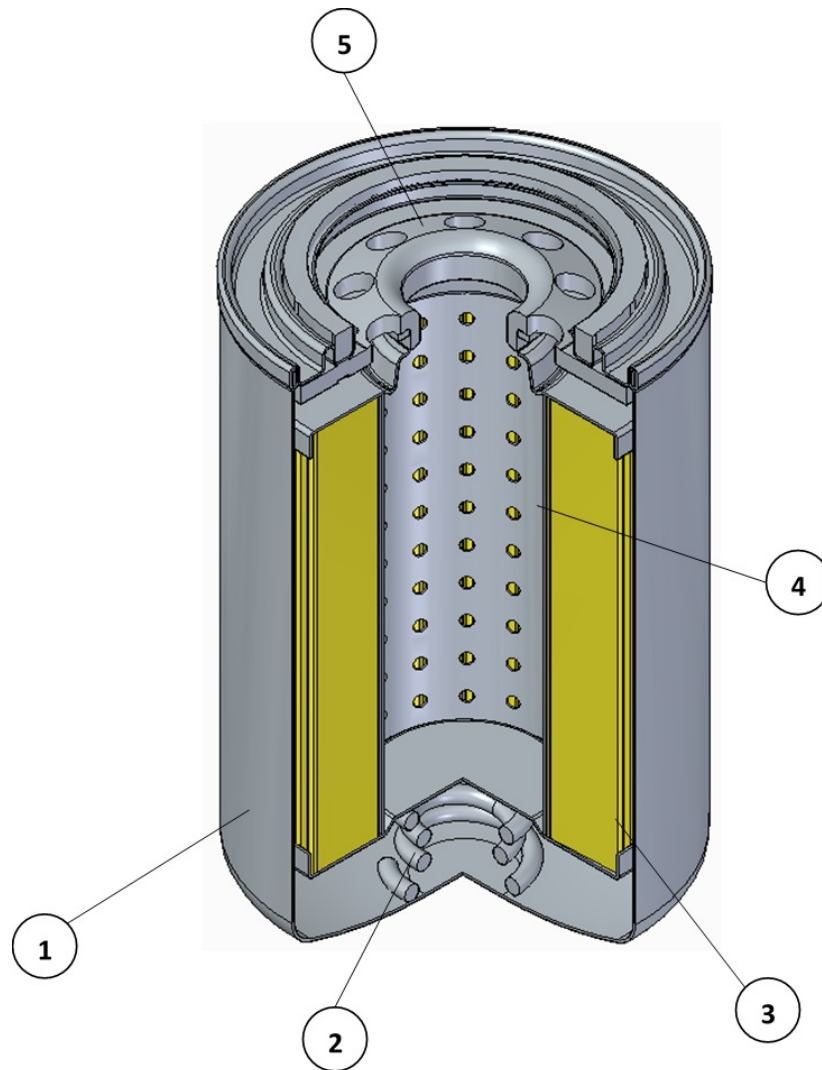


Figure 2.1: Oil filter components

medium provided by DELGROSSO (see chapter 5). Since the aim of this thesis is the parametric study, besides CFD, it is necessary to specify what parameters have to be changed. They are represented in Figure 2.2:

- Number of holes;
- Hole diameter (D_{hole});
- Distance between the threaded plate and top surface of filter media (h)

- Surface of filter medium (number of folds)
- Filter medium's height (HC)

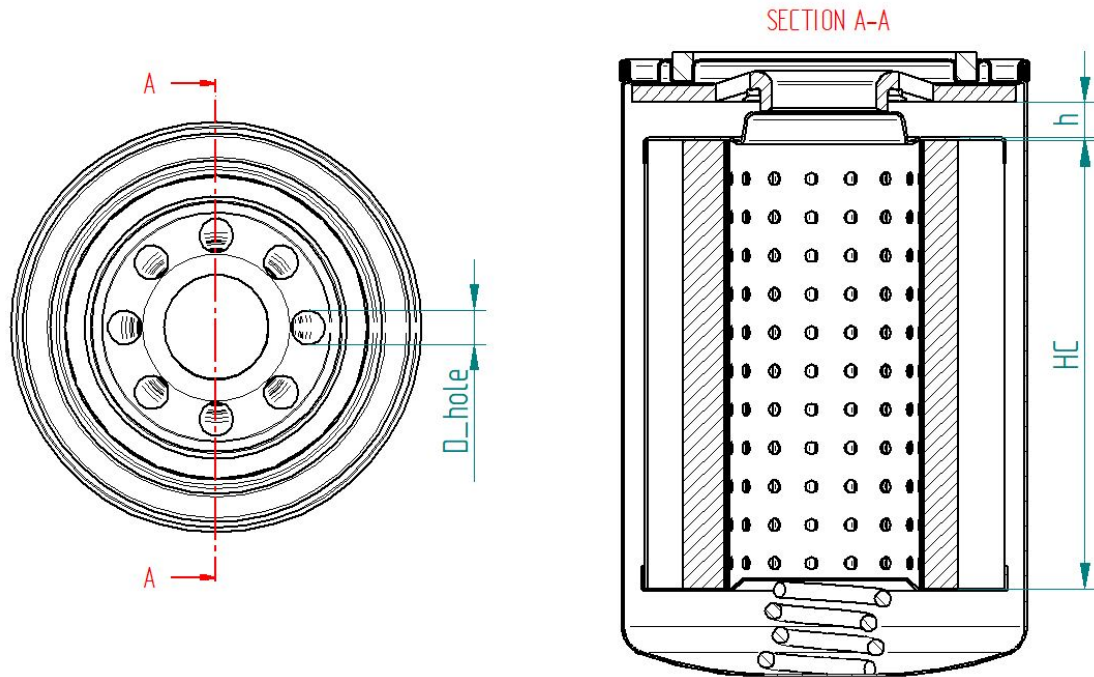


Figure 2.2: Oil filter: Top view (left) and front section view (right)

2.2 General working principle

The working fluid enters with a given volume flow rate through the inner holes on the top of the threaded plate going towards the filter media. Once the filter medium has been reached, surface and depth filtration happen (see chapter 5). In order to increase the efficiency of the filtration process, filter media is folded in on itself and fluid flow takes advantage. During this phase, fluid speed decreases enabling the entrapment of contaminant particles resulting in an increase of pressure drop and better filtration. Once the fluid has passed the filter element, it crosses the perforated metal support by increasing its velocity and climbs toward the outlet hole (see Figure 2.3)

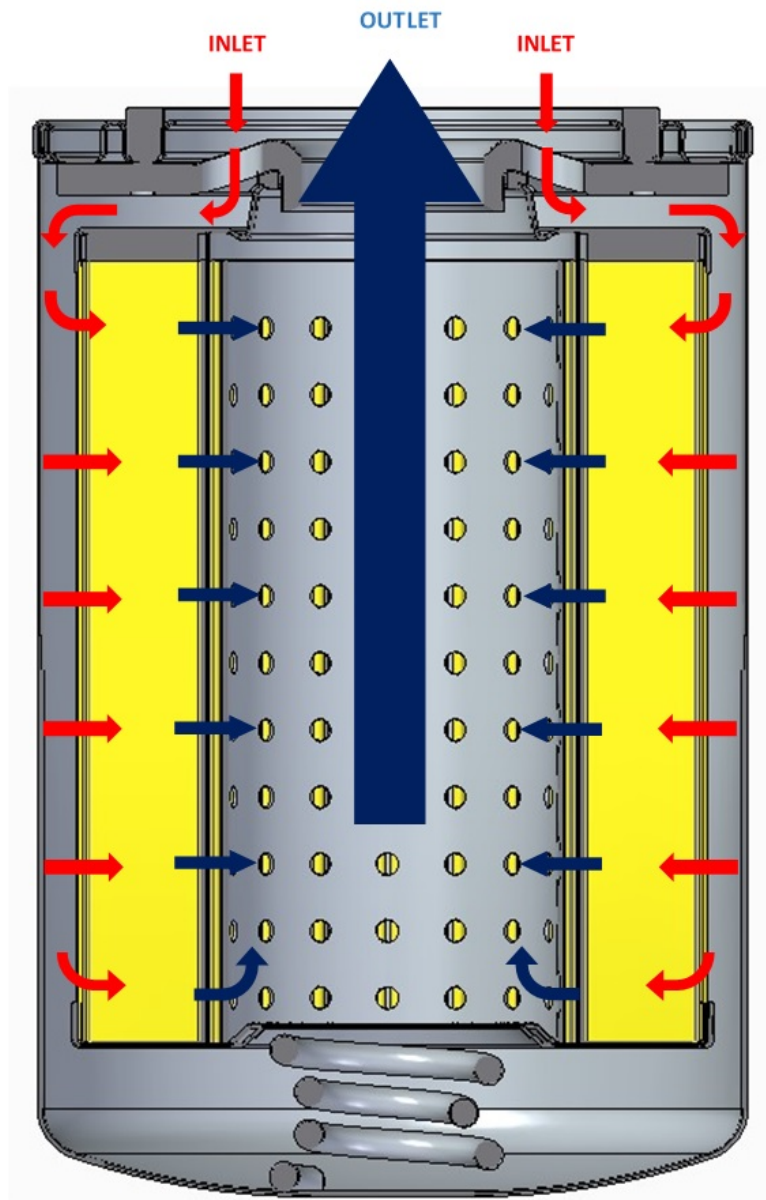


Figure 2.3: Working principle of the oil filter

2.3 Working fluid

The working fluid chosen for the simulations is the *Aeroshell Fluid 41*. It is a mineral hydraulic oil manufactured to a very high level of cleanliness. It contains additives which provide the following properties [4]:

- Low freezing point
- Minimum viscosity change with temperature;
- Good corrosion and oxidation stability;
- Good seal compatibility;
- Shear stability;
- Improved cleanliness;
- Fire resistance;
- Good anti-foam properties;
- Good low and/or high temperature stability;

Figure 2.4 lists all of the chemical and physical properties of the working fluid *Aeroshell Fluid 41*.

PROPERTIES	MIL-PRF-5606J	TYPICAL
Oil type	Mineral	Mineral
Kinematic viscosity @ 100°C (212°F) @ 40°C (104°F) @ -40°C (-40°F) @ -54°C (-65°F)	mm ² /s 4.90 min 13.2 min 600 max 2500 max	4.9 - 5.30 13.2 - 14.3 460 - 600 2200 - 2500
Flashpoint	°C (°F) 82 (179) min	90 - 95 (194 - 203)
Pourpoint	°C (°F) -60 (-76) max	-60 (-76) max
Total acid number	mgKOH/g 0.20 max	0.02 - 0.05
Evaporation loss 6 hrs @ 71°C (160°F)	%m 20 max	10 - 15.4
Water content	ppm 100 max	50 - 75
Relative density @ 15.6°C (60°F)	Report	0.868 - 0.873
Colour	Red	Red
Particle contamination, number of particles per 100ml in size range		
5 to 15 µm	8000 max	1200 max
16 to 25 µm	1425 max	1425 max
26 to 50 µm	253 max	253 max
51 to 100 µm	45 max	45 max
over 100 µm	8 max	8 max
Particle count	5	5 max
Copper corrosion	2e max	2b
Steel on steel wear scar diam	mm 1.0 max	0.6 - 0.95
Rubber swell, I rubber 168 hrs @ 70°C (158°F)	% 19 to 30	Passes
Low temperature stability 72hrs @ -54°C (-65°F)	Must pass	Passes
Gravimetric analysis	mg/100ml 1.0 max	Passes
Foaming tendency	Must pass	Passes
Barium content	ppm 10 max	Nil

A viscosity/temperature curve is shown at the end of this section.

Figure 2.4: Aeroshell Fluid 41 properties

Chapter 3

Computational Fluid Dynamics

Computational fluid dynamics (CFD) is the science that allows predicting fluid flow, heat transfer, mass transfer and related phenomena by solving the governing equations using numerical methods (discretization). CFD simulations approximate with high reliability the behaviour of the defined working fluid under certain boundary conditions. Generally, all CFD software contains three main elements [5]:

- Pre-processor
- Solver
- Post-processor

In the first phase, there is the definition of the computational domain by generating a grid (or mesh) of control volumes. Physical and chemical phenomena are modelled and appropriate boundary conditions are selected. Second phase is carried out by the software solver that through the finite volume method (described in section 3.2) solves all constitutive equations iteratively until the convergence of the desired parameter is reached. Finally, in the last phase there is a visualization and post-processing of the obtained results (2D and 3D surface plots, fluid animations, vector plots). All the analyses have been performed on a machine with 16 Gb RAM, but only 12 Gb were directly involved by the FloEFD Software, which means that the computational domain can be divided by a maximum of 3 millions of cells.

3.1 Governing Equations

The fundamental equations of fluid dynamics represent the mathematical statements of the conservation laws of the following universal laws of conservation:

- Conservation of Mass (continuity equation)
- Conservation of Momentum (Newton's second law)
- Conservation of Energy (first law of thermodynamics)

In addition to these equations (called Navier - Stokes - Fourier equations), it is necessary to describe the fluid's behaviour in terms of macroscopic properties, such as velocity, pressure, density and temperature. Moreover the fluid must be considered as a continuum. Since the analysis of the fluid flow is at a macroscopic length scale, the molecular structure of matter and its motions may be ignored [6].

3.1.1 Continuity equation

In order to derive the mass conservation equation, it is necessary to write down a mass balance of an infinitesimal fixed control volume passed by a fluid flow (*Eulerian approach*). It yields:

$$\frac{\partial \rho}{\partial t} + \nabla \cdot \rho \mathbf{u} = 0 \quad (3.1)$$

where:

- ρ : density $\left[\frac{\text{kg}}{\text{m}^3} \right]$
- u : fluid velocity $\left[\frac{\text{m}}{\text{s}} \right]$
- t : time [s]

The Equation 3.1 is the continuity equation in the *unsteady* condition with a *compressible* fluid. The first left term represents the rate of change in time of density, while the second describes the convective term. A flow in which the density of each fluid element remains constant is called *incompressible*, and the Equation 3.1 reduces to:

$$\frac{\partial \rho}{\partial t} = 0 \Rightarrow \nabla \cdot \mathbf{u} = 0 \quad (3.2)$$

3.1.2 Momentum equation

The momentum equation provides a mathematical expression of Newton's second law applied to a fluid passing through an infinitesimal and fixed control volume. It states that the rate of change of momentum of a fluid particle equals the sum of forces on the particle. The external forces taken in consideration are:

- surface forces:
 - pressure forces
 - viscous forces
- body forces:
 - gravity force
 - centrifugal force
 - Coriolis force
 - electromagnetic force

Generally, the contribution of body forces is considered as a source term, while surface forces are defined in terms of stress tensor. The differential form of the momentum equation is represented in the following Equation 3.3:

$$\frac{\partial(\rho\mathbf{u})}{\partial t} + \nabla \cdot \rho\mathbf{u}\mathbf{u} = \rho\mathbf{g} + \nabla \cdot \Pi \quad (3.3)$$

The liquid considered for this work behaves like a *Newtonian fluid* (oil, water, gas), in which the viscous stresses are proportional to the rate of deformation. With this assumption it is possible to derive a deformation law that relates stress tensor to the pressure and velocity components. This relation becomes:

$$\Pi = -p\delta_{ij} + \tau \quad (3.4)$$

where the term τ represents the viscous stress tensor given by

$$\tau = -\mu(\nabla\mathbf{u} + \nabla\mathbf{u}^T) + \left(\frac{2}{3}\mu - \kappa\right)(\nabla \cdot \mathbf{u})\mathbf{I} \quad (3.5)$$

In general, the parameter κ (bulk viscosity) is negligible. By substituting the Equation 3.5 in the Equation 3.4 and then in Equation 3.3, the final equation becomes:

$$\frac{\partial(\rho\mathbf{u})}{\partial t} + \nabla \cdot \rho\mathbf{u}\mathbf{u} = -\nabla p - \nabla \cdot \tau + \rho\mathbf{g} \quad (3.6)$$

3.1.3 Turbulence model

FloEFD is the software used to perform all CFD simulations. It is capable of predicting both laminar and turbulent flows. In theory, fluid flow behaviour depends on the *Reynolds* number, consisting in the ratio between inertial and viscous forces (Equation 3.7):

$$Re = \frac{\rho u D}{\mu} \quad (3.7)$$

When:

$$\begin{cases} Re < 2100, & \text{laminar} \\ 2100 < Re < 4300, & \text{transition} \\ Re > 4300, & \text{turbulent} \end{cases} \quad (3.8)$$

In practice, the values that establish flow conditions are quite different from the theory. In fact, the laminar flow occurs when $Re < 10$ and strictly turbulent flow occurs with $Re > 10^5$. Most of the fluid flows encountered in engineering practice are turbulent, while from an oleo-dynamic point of view, laminar flow prevail. FloEFD employs one system of equations to describe both laminar and turbulent flows. Moreover, transition from a laminar to turbulent state and/or vice versa is possible. In order to predict turbulent flows, a complex system of equations are used, where time-averaged effects of the flow turbulence on the flow parameters are considered. Extra terms known as the Reynolds stresses appear in these equations for which additional information must be provided. To close this system of equations, FloEFD employs transport equations for the turbulent kinetic energy and its dissipation rate, the so-called $k - \epsilon$ model [7].

3.1.4 Darcy's Law

Considering that the aim of this thesis is to simulate fluid flows inside a porous media, the equations mentioned above are not enough to describe accurately the fluid dynamic phenomenon. The *single phase flow* of an incompressible viscous fluid through a porous media is governed by the continuity and momentum equation by taking the Darcy model. We make the assumptions that the mass fluxes due to dispersion and diffusion are so small that they are negligible. Denote by Φ the *porosity* of the porous medium (explained in detail in chapter 5) and by q the external sources and sinks, the mass conservation equation, becomes [8]:

$$\frac{\partial(\Phi\rho)}{\partial t} = -\nabla \cdot (\rho\mathbf{u}) + q \quad (3.9)$$

According to Darcy's law (Darcy,1856), there is a linear relationship between the fluid velocity and the pressure gradient (Equation 3.10):

$$\mathbf{u} = -\frac{\mathbf{k}}{\mu}(\nabla p - \rho\mathbf{g}) \quad (3.10)$$

where \mathbf{k} is the *absolute permeability* tensor (see paragraph 5.3.2) and \mathbf{g} is the gravity acceleration. Darcy's law is used for slow flows where the *Re* number is scarce. In order to consider fluid with higher velocity, the Brinkman equation has to be introduced. It is an extension of the traditional Darcy's law and considers fast-moving fluids in porous media with the kinetic potential from fluid velocity, pressure, and gravity driving the flow (Equation 3.11).

$$-\beta\nabla^2\mathbf{u} + \mathbf{u} = -\frac{\mathbf{k}}{\mu}(\nabla p - \rho\mathbf{g}) \quad (3.11)$$

3.2 Finite volume method

The numerical solution technique employed in FloEFD is based on the finite volume method (FVM). The presence of non linear terms in Navier-Stokes equations leads to a volume integral, which has to be approximated by a linearization procedure. In the FVM volume integrals in a partial differential equation that contain a divergence term are converted to surface integrals using the divergence theorem. These terms are then evaluated as fluxes at the surfaces of each finite volume. For the sake of simplicity, it is possible to sum up FVM in three steps:

1. Grid generation: the domain is divided into discrete control volumes
2. Discretization: the integration of the governing equations to yield a discretized equation at the CV nodal point
3. Solution of equations

All physical parameters are referred to the control volume mass center.

Chapter 4

Part I: Filter Head

This chapter will depict the activities of the internship at DELGROSSO S.R.L. where the main focus was to model and simulate the head of the component described in chapter 2.

4.1 Geometry

The control volume should have been assembled by the components that were shown in the original CAD model, however there are lots of elements that have no influence on the fluid-dynamic phenomenon, therefore a new CAD model has been drawn (Figure 4.1).

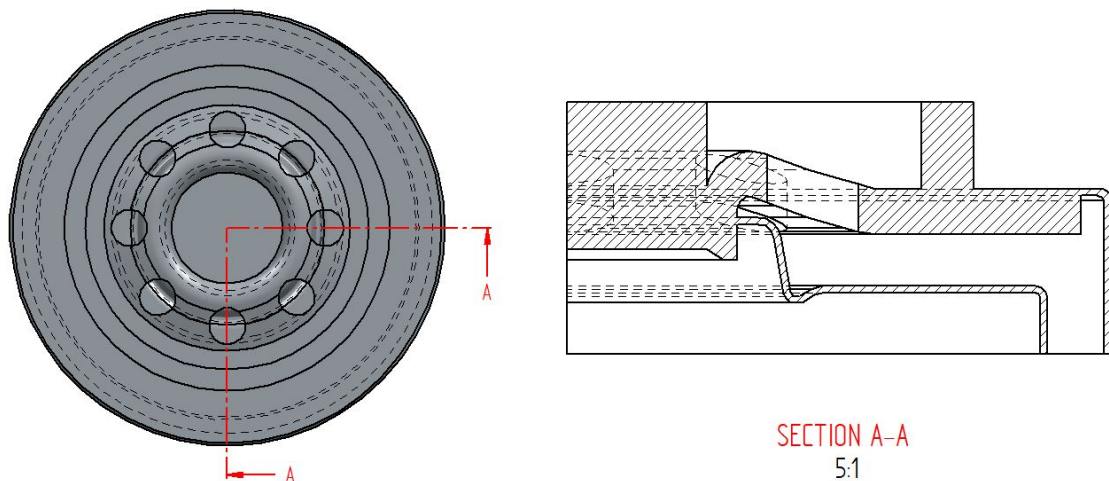
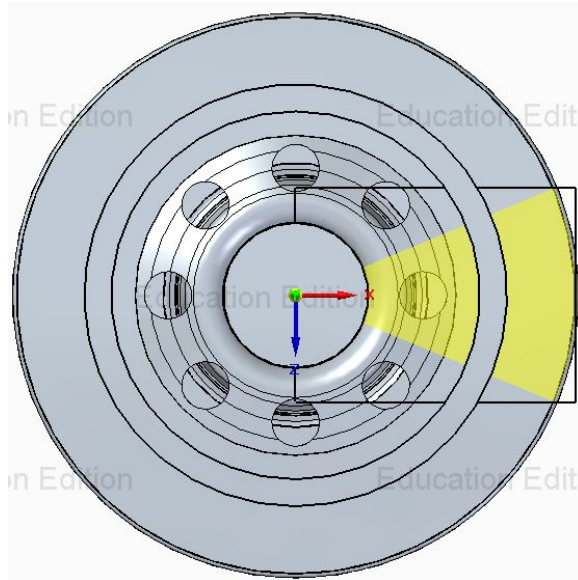


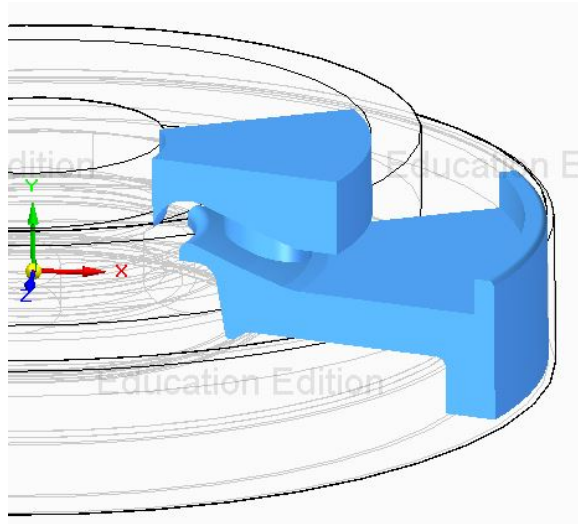
Figure 4.1: Filter head: Top view (left) and front section (right)

4.2 Domain

Once the CAD component is created, the choice of computational and fluid domain has to be determined. In order to reduce the computational time, the axial-symmetric domain of only one hole is selected (Figure 4.2).



(a)



(b)

Figure 4.2: (a) Computational domain; (b) Fluid domain

4.3 Boundary conditions

After the domain selection, it is required to set-up the model and boundary conditions. The CFD simulations hypotheses of the model are:

- Steady state condition
- Negligible gravitational effects
- Working fluid temperature: $T = 273.15$ K.
- Adiabatic surfaces (No heat transfer)
- Surface roughness ($Ra = 45\mu m$), irrelevant for the analysis
- "laminar-turbulent" study in FloEFD settings
- $k - \epsilon$ turbulence model

The goal of the simulations is to compute the pressure loss between the upstream surfaces (inner holes) and the downstream exit. Therefore the following boundary conditions have been selected (4.3):

- Volume Inlet flow: $Q = 12.5 \frac{1}{\text{min}}$ (red arrows)
- Static Outlet pressure: $p_{out} = 101,325$ Pa (blue arrows)

The first boundary condition imposes the fluid flows inside a single inner hole, considering the full assembly flow rate being $100 \frac{1}{\text{min}}$.

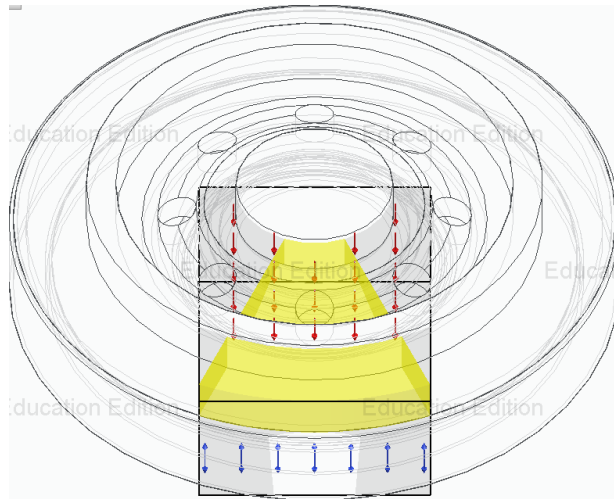


Figure 4.3: Boundary conditions

4.4 Mesh

As it was previously stated in chapter 3, it is very important to correctly discretize the domain. FloEFD provides the possibility to generate the mesh both automatically and manually. In this thesis work, all meshes (global and local) will be created manually. In order to guarantee the most accurate results a *mesh independence study* (Figure 4.4) has been performed, i.e. a study where all the simulations goals are independent from the selected mesh refinement level and are obtained with the lowest number of cells and calculation time possible. Several attempts of the simulation run have been made, using different mesh configurations. The parameters changed during simulations were local and global refinement level. In Figure 4.5 and in Table 4.1 it is possible to observe the final refinement levels achieved after the mesh independence study which corresponds to:

$$N_{cells,head} = 1,528,937$$



Figure 4.4: Mesh independence study

Mesh	Type	Refining Grade	Small Solid	Curv.	Tol.
Global	Automatic	0	4	4	4
Hole Mesh	Local	5	4	4	4
Upper Mesh	Local	4	4	4	4
Lower Mesh	Local	4	4	4	4
Exit Mesh	Local	2	4	4	4

Table 4.1: Mesh choice

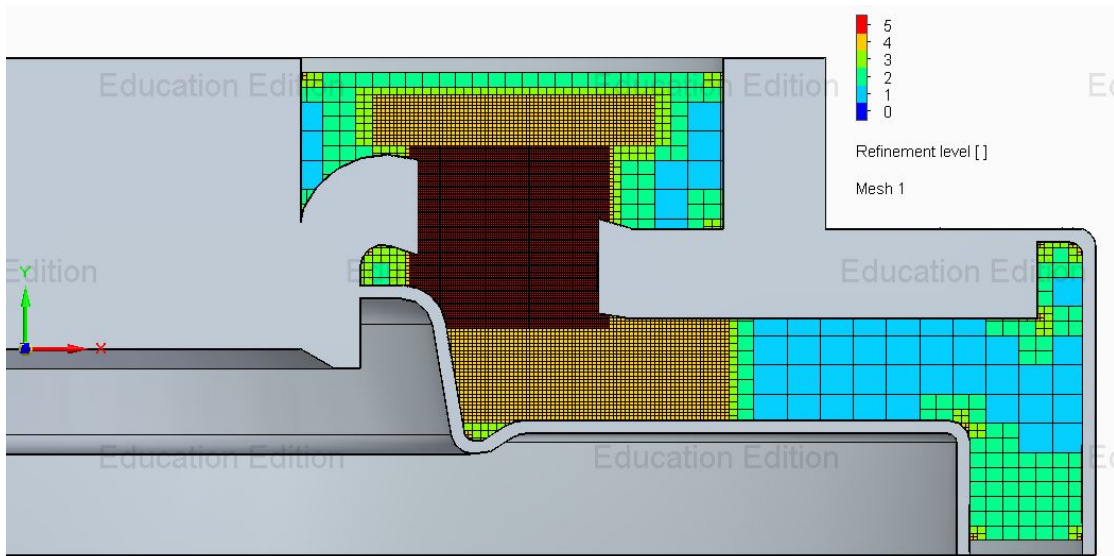


Figure 4.5: Filter head mesh cut plot refinement

4.5 Results

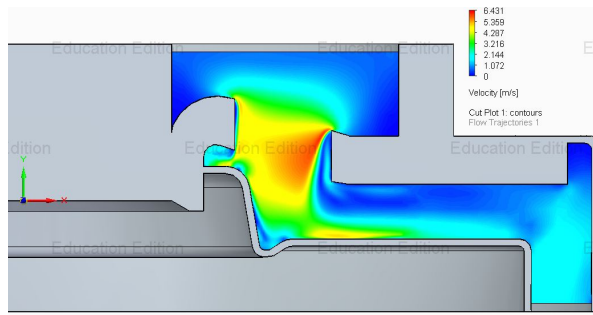
This paragraph displays all of results obtained from the CFD simulations of the filter head under discussion (Figure 4.6). It is possible to observe that the maximum pressure gradient (Figure 4.6b) occurs when fluid passes through the holes. This is because velocity profiles suddenly increase its values due to the area restriction (Figure 4.6a) causing high pressure drop.

4.6 Parametric study

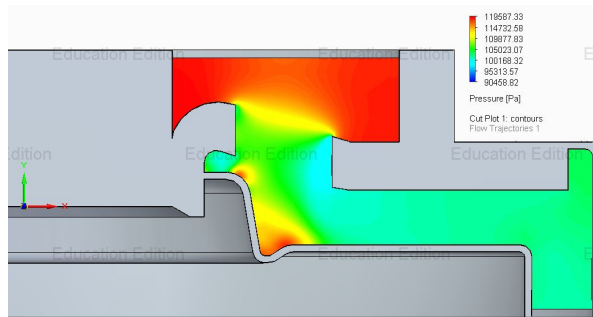
The latest part of the internship was the parametric study on the filter head in question. The parameters involved in the study were:

- Hole diameter
- Number of holes
- Distance between the threaded plate and top surface of filter media

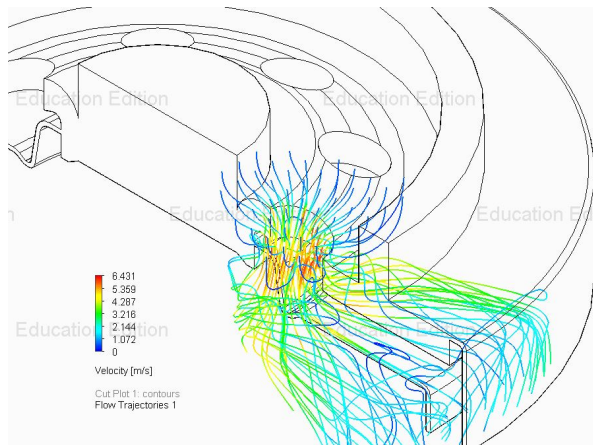
For each simulation only one parameter of interest was changed, leaving the other two unchanged and the pressure losses were computed. The variation of the model geometry and the constructive parameters, involves a variation of both the fluid domain and the computational domain, with a subsequent increase in the number of cells and therefore in the calculation time. The reference



(a)



(b)



(c)

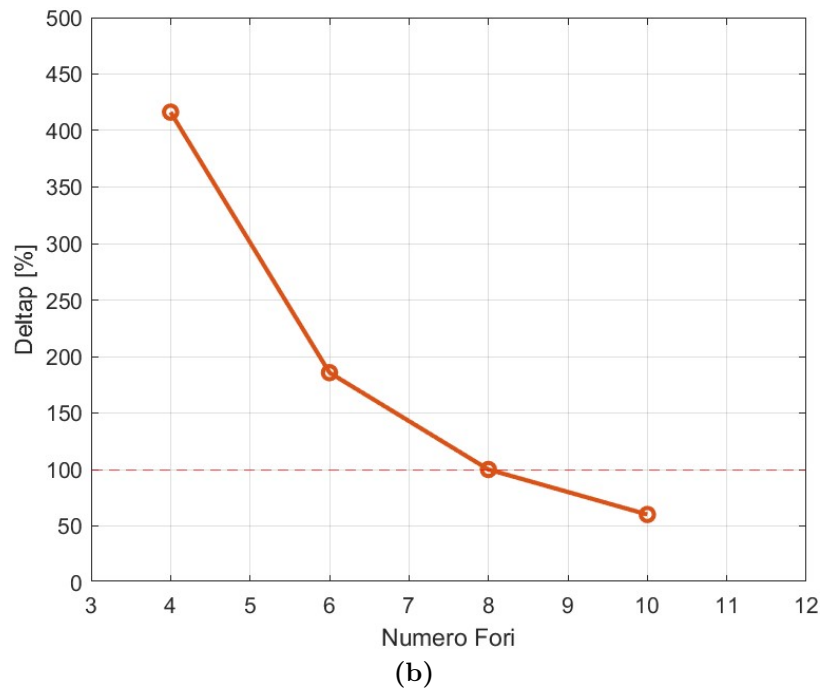
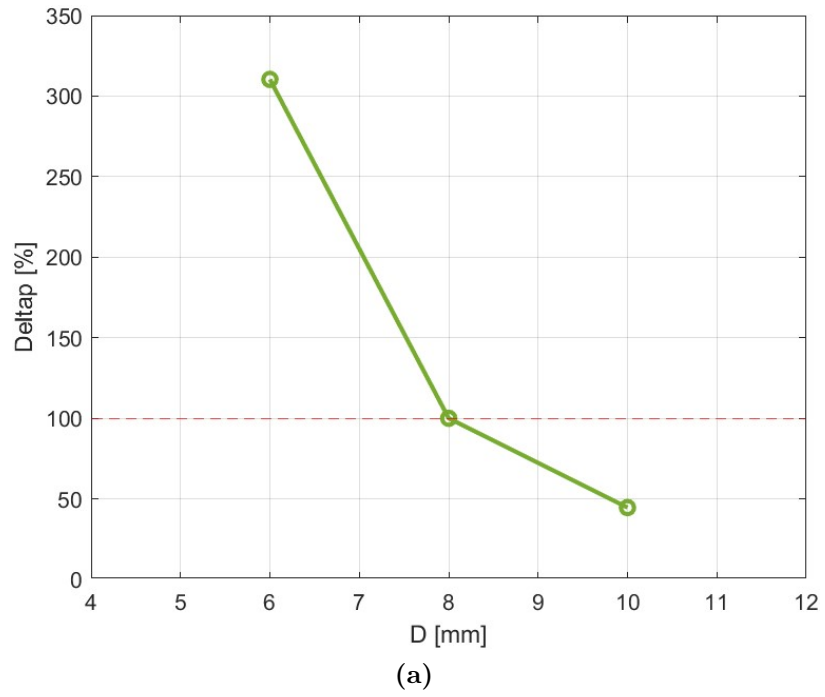
Figure 4.6: (a) Velocity distribution cut plot ; (b) Pressure distribution cut plot ; (c) Flow trajectory speed color plot

model was the starting component with:

$$N_{holes} = 8 \wedge D_{hole} = 8 \text{ mm} \wedge h = 4.5 \text{ mm} \Rightarrow \Delta p = 100 \%$$

The following Figure 4.7 represents all plots obtained from the parametric study

with the boundary conditions explained in section 4.3.



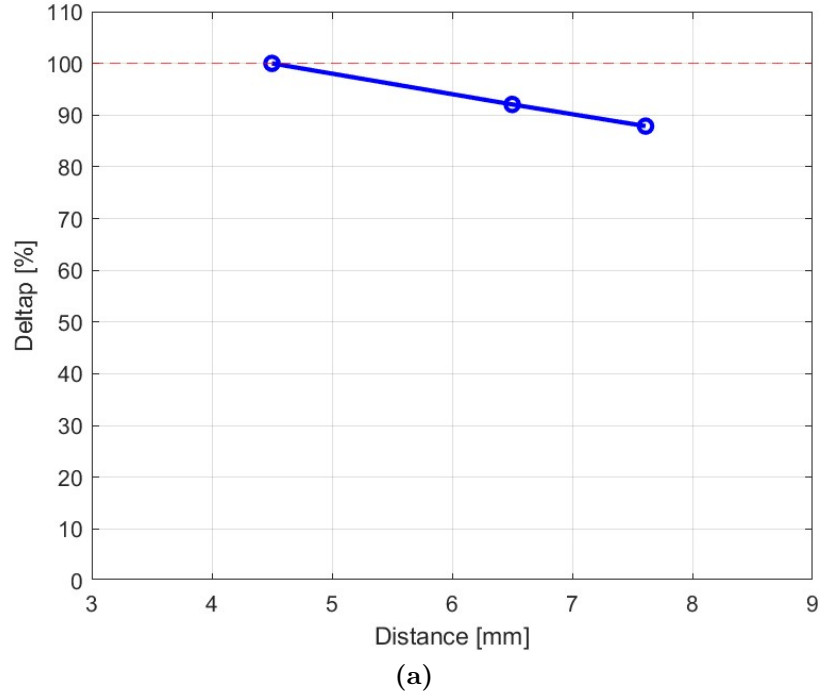


Figure 4.7: (a) Δp vs D_{hole} plot ; (b) Δp vs N_{holes} plot ; (c) Δp vs h plot

It is easily observable how the constructive parameters listed and analyzed previously have an important weight on the filter head pressure drop. In particular, the hole diameter and the number of holes. The Table 4.2 shows a sum up of the parametric study previously discussed.

D_{hole}	N_{holes}	h	Δp
↑	constant	constant	↓↓↓
constant	↑	constant	↓↓
constant	constant	↑	↓

Table 4.2: Pressure losses sensitivity to parametric study

Chapter 5

Part II: Filter Medium

This chapter is the core of the entire thesis work. It will describe the fluid dynamic modeling process and the characterization of the filter element properties. When thinking about filters, it is usual to compare them to elements with very fine meshes which retain particles with a "grid system" (those larger than the grid do not get through). In reality, the situation is more complex. In oil filter, most of the time, there is no grid, but filter medium is made up of cellulose fibers suitably impregnated with resins, arranged in a disordered manner to form a structure with a high porosity. Though it is important to have a wide porous surface in order to ensure proper filtration, it is also important to have a compact design to avoid unnecessary encumbrance, therefore a pleated geometry of the filter medium has been used. The most common type of oil filter used in automotive field is the cartridge filter, that has the peculiarity to be easily replaceable.

5.1 Filter medium material

As it was described in chapter 2, a cartridge filter is selected for oil filtration purposes, and a cartridge unit is installed. The cartridge may be formed of a single layer of medium if the material is sufficiently rigid to be self-supporting (such as sintered metal or wire-wound). In this case, the cartridge comprises a rigid perforated metal core supporting a *pleated resin treated filter media* [9]. The fiber composition is chosen to provide for filtration properties such as bulk, permeability, and pore size, whereas the resins are chosen to provide processability, strength, endurance, and stability. It is important for the paper to be stiff and yet flexible enough to go through the pleating process and not degrade in the thermal aspects of this process. Obviously, at the end of all treatments, the medium has to have enough strength and rigidity to resist both against the

pressure of the fluid flowing through them and the thermo-chemical environment to which they are exposed. The chosen filter media is the one mentioned in chapter 2 and its properties will be listed later.

Phenol impregnation was performed on the filter medium to provide stiffness and high modulus. Generally, pleated resin filter media are corrugated. Through this whole process, the material obtains different properties such as additional stiffness and a higher area of filtration due to the fact that the corrugations provide flow channels to the interior pleat folds. Moreover, corrugations act as pleat separators for the pleat folds (Figure 5.1)

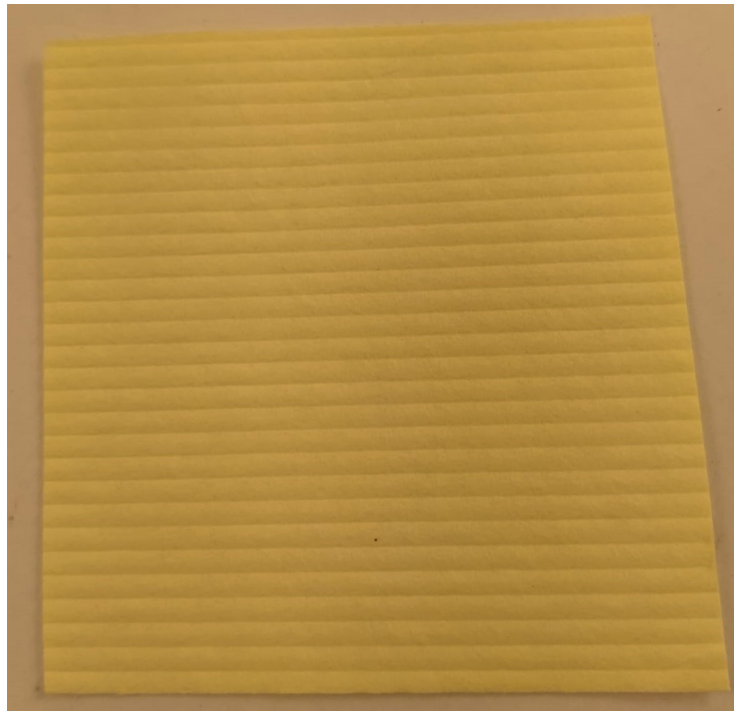


Figure 5.1: Pleated resin treated filter media

Each kind of filter model defines the type of filtration process that occurs. The four basic mechanisms that characterize the filtration process are:

- (a) *Surface straining*: The particles larger than the pores diameter cannot pass through.
- (b) *Depth straining*: The particles penetrate the pores until they reach a necking point where the diameter becomes smaller than the particle and at this point the particle is trapped in the pore [9].
- (c) *Depth filtration*: The process is similar to depth straining, but the only difference is that the particle is removed even if it is smaller than the diameter

at any point in the pore structure through a specific mechanism.

- (d) *Cake filtration*: A thick layer (cake) of particles accumulates on the surface of the medium, and then acts as the filter medium for subsequent filtration.

The (a) process is generally associated with regular pore openings, such as woven mesh fabrics material, while the others are applied to felts and nonwoven material, where the pore's diameters are variable in depth. Needless to say, any real filtration process involve a combination of the above mechanisms. For the selected cartridge filter, the depth filtration procedure is the one being used.

5.1.1 Depth filtration

As it was mentioned above, depth filtration includes a mixture of complex physical mechanisms concerning the capture of the particle. It is very important to highlight that for the vast majority of the filtration processes, the fluid flow in the region of the filter medium is laminar and the assumption is that particles tend to follow smooth streamlines. All mechanisms are illustrated in Figure 5.2 and they are:

- *Inertial impaction*: The particle has high inertia (sufficient momentum) to come off from the air streamlines and impact the fiber.
- *Interception*: The particle does not have sufficient inertia to break away from the streamline, however it will still come very close to the fiber and it will attach on it. A mathematical model is described by Lastow and Podgorsky.
- *Diffusion*: The particle is very small and random and probabilistic motion (Brownian motion) will cause the attachment.
- *Electrostatic attraction*: The surface charge of the particle may be opposite to that of a fibre or pore in the filter medium, causing its path to divert onto the medium where it will remain and Van der Waals' forces will come into play.
- *Gravity*: Larger and denser particles may settle out in within a filtration system and potentially accumulate and affect the performance of the system.

The selected medium is a nonwoven fabric and the pore structure is of sufficient small size that the concerns of high Reynolds number and related turbulence

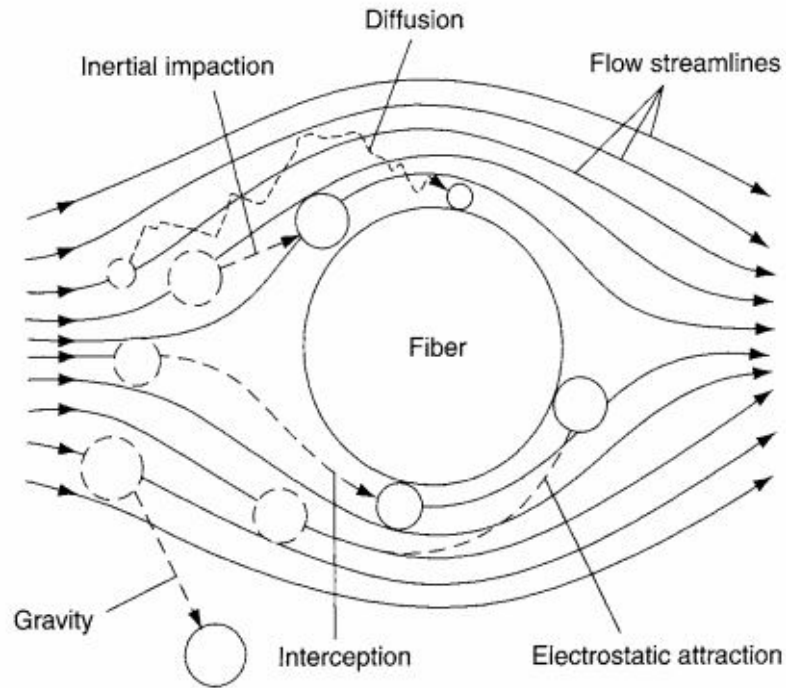


Figure 5.2: Depth filtration mechanisms
(Source: *Handbook of Non-Woven Filter Media*)

generally do not apply, Darcy's law in Equation 3.10 can be further simplified to

$$u = \frac{k \Delta p}{\mu L} \quad (5.1)$$

where Δp [Pa] is the pressure drop across the thickness L [m] of the fabric.

5.2 Geometry

As shown in section 4.1, a new CAD model of the filter element has to be drawn in order to simplify the control volume and simulate the fluid-dynamic phenomenon. The contribution of the filter medium on the total pressure drop is not only caused by its purpose, but is also due to the complex pattern of the fluid flow within the pleat such as pleat deformation and pleat collapsing. The properly designed assembly is composed by (Figure 5.3):

1. Housing
2. Upper cover

3. Filter Medium

4. Base

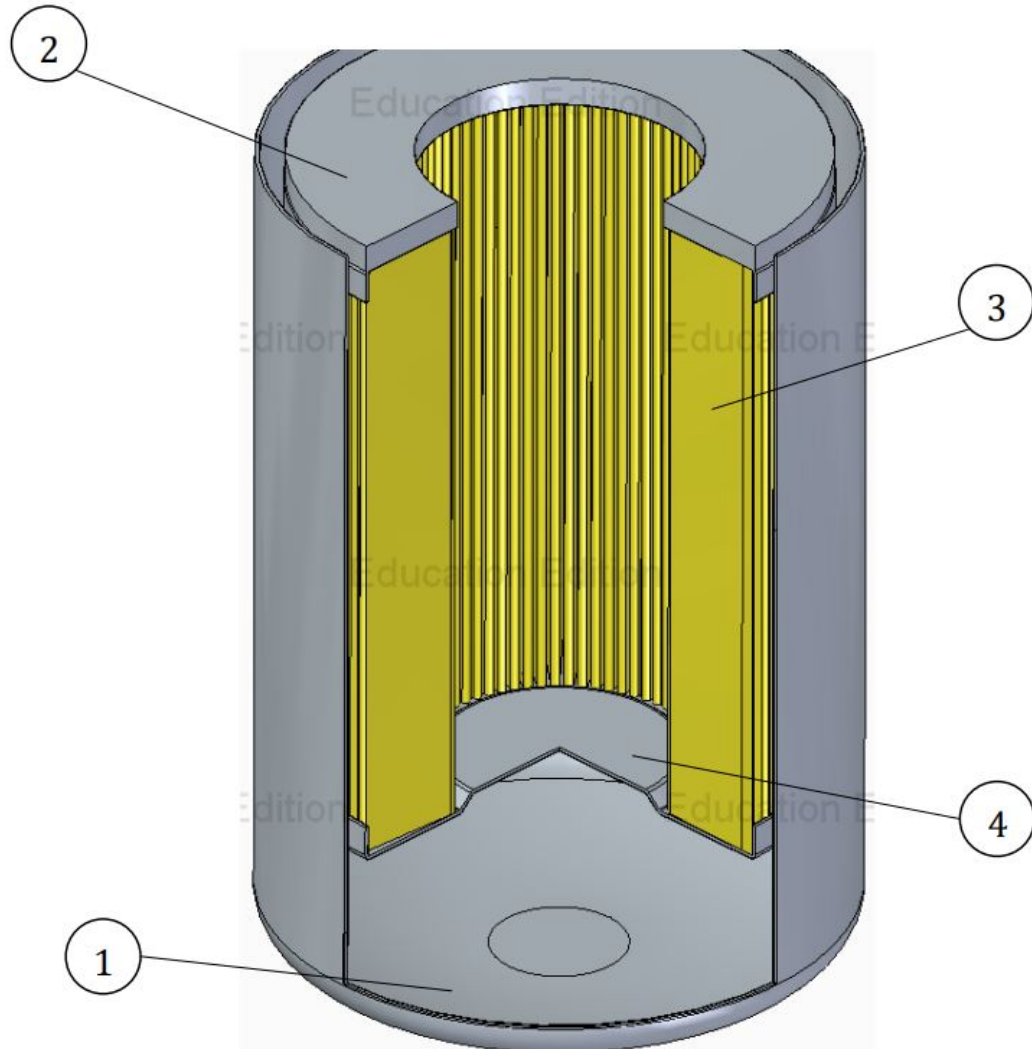


Figure 5.3: Assembly of the filter element

It is important to note that the upper cover has been slightly extended so as to consider the same development of the fluid flow seen in chapter 4 simulation. Differently from previous fluid-dynamic analysis, the porous media condition has to be assigned to the specific body in Figure 5.4. Through this condition, a lot of computational time can be saved and no filter medium mesh is required. In the following sections all porous medium parameters required by FloEFD software will be explained, while the procedure to assign porous medium condition

is illustrated in Appendix C.

The filter medium that is being used in the thesis has the following properties (Figure 5.4):

- $HC = 105 \text{ mm}$
- $HP = 19 \text{ mm}$
- $N_{Folds} = 60 \pm 3$
- $S_{filtration} = 2,394 \text{ cm}^2$
- $Thickness = 0.55 \text{ mm}$
- $D_{exit} = 25 \text{ mm}$

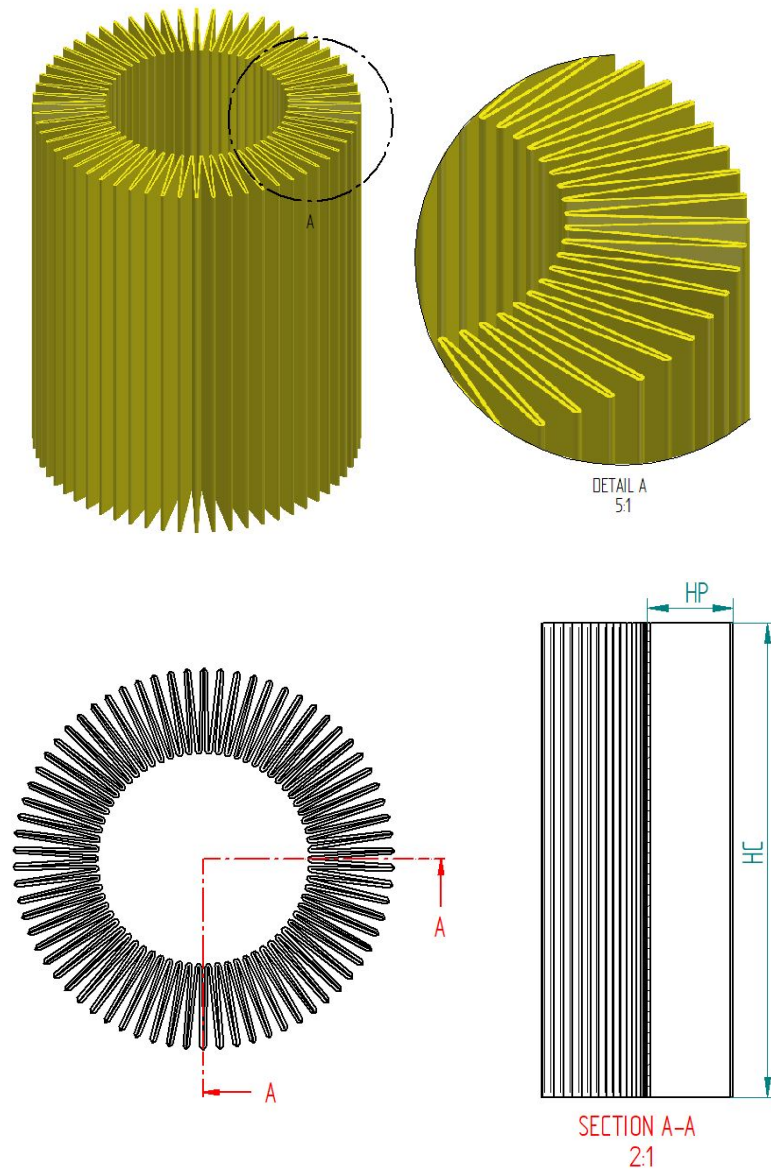


Figure 5.4: Filter medium

5.3 Properties of porous medium

A porous medium can be characterized at both microscopic and macroscopic level. At the microscopic level the structure is expressed so as to cover understanding of surface phenomena such as the adsorption of macro molecules from polymer solutions and the blockage of pores. From the fluid-dynamic point of view, the macroscopic approach is necessary and sufficient to describe phenomena such as fluid flow, heat and mass transfer. FloEFD treats porous media as distributed resistances to fluid flow, so they cannot occupy the whole fluid region or fill the dead-end holes. In order to perform a reliable calculation, some parameters of the *porous media* model have to be specified. These macroscopic parameters used to quantify and describe the flow of a single phase fluid are [10]:

- *Basis weight*: the weight of the media per unit area.
- *Thickness*: the surface-to-surface distance of the flat paper.
- *Stiffness*: the ability to resist an applied bending force.
- *Burst strength*: the hydro static pressure to produce rupture of sample paper.
- *Tensile strength*
- *Filtration efficiency*: the ability of the filter media to capture particles of different size.
- *Porosity*: the physical structure of the pores and its surrounding.
- *Permeability*: it represents how easily the fluid flows through the medium.

The next paragraph will describe in details both *porosity* and *permeability*, since they have to be specified inside the FloEFD software in order to start all CFD simulations.

5.3.1 Porosity

Using porous media simplification reduces CAD and mesh complexity, and saves computational time and expenses. The first parameter that has to be specified is the porosity. As it was mentioned before, the filter medium pore structure is extremely complex. Since one of the most important factors is how much available space there is between the fibers, that is necessary to store contaminants or for fluid flow, the porosity definition is introduced. In a nonwoven, there are some ingredients such as fiber, resin and additives that can contribute to the solid volume of the structure.

Quantitatively, porosity is defined as the ratio between the void volume and the total (bulk) volume (5.2)

$$\Phi_{absolute} = \frac{V_{pore}}{V_{bulk}} \quad (5.2)$$

Depending on the complexity of the porous medium structure, many of the void spaces are interconnected, while some pore spaces are isolated. From an engineering point of view and for practical reasons, the *effective porosity* is defined as:

$$\Phi_{eff} = \frac{V_{eff}}{V_{bulk}} \quad (5.3)$$

where V_{eff} is the volume occupied by the interconnected pores. Figure 5.5 illustrates the various pore complexity. Moreover, porosity may be expressed as either fractions or percentages.

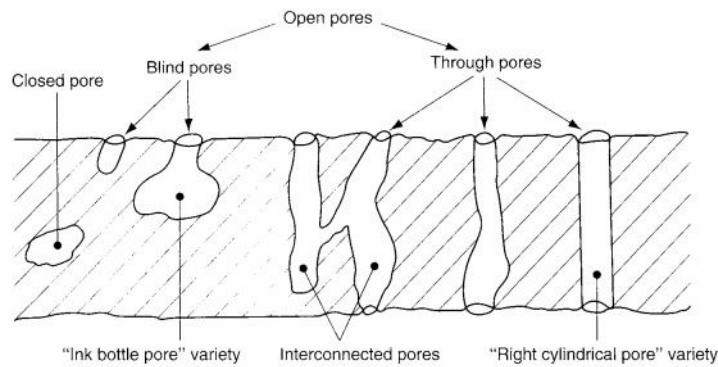


Figure 5.5: Pore complexity
(Source: *Handbook of Non-Woven Filter Media*)

Along with the definition of porosity, the pore size and structure are important factors as well. They can be determined through the Capillary Flow Porometry (CFP) technique which consider the fibers inside the filter medium like cylindrical capillaries. The technique is based on the following scheme:

1. The sample is wet with an inert and nontoxic liquid (DELGROSSO S.R.L. uses *Porofil*)
2. Increasing inert gas pressure is applied to one side of the sample.
3. The liquid will be expelled from each through each pore according to its size (larger first).
4. A *gas flow rate vs pressure* plot is given from the porometer.

Figure 5.6 shows the results from a porometer test performed by DELGROSSO S.R.L. with Porometer 3G Quantachrome (Figure 5.7) on the sample of the same filter medium material under discussion. From data from the wet curve

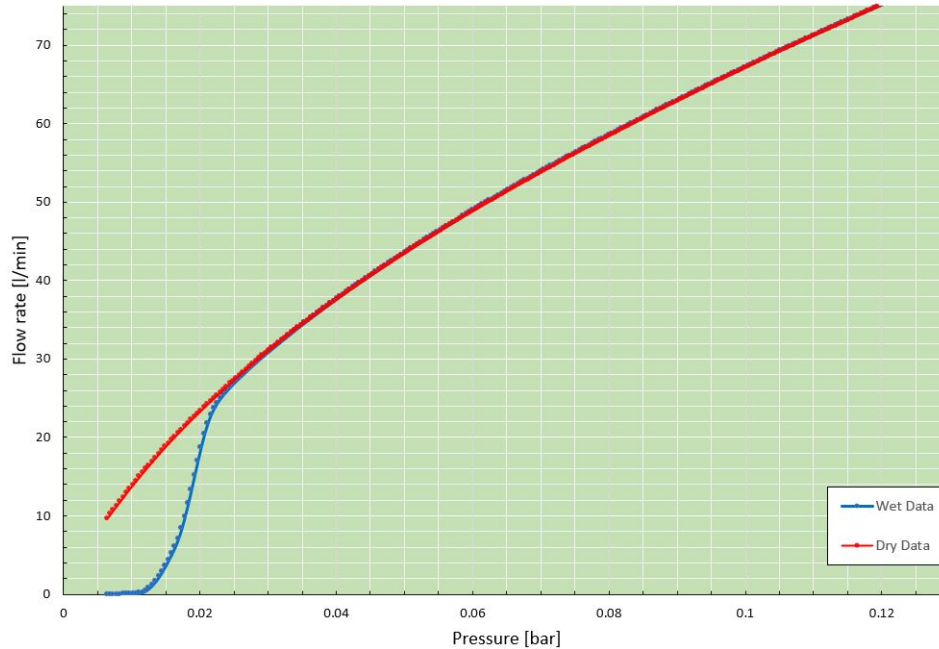


Figure 5.6: Flow vs pressure data for measured wet and dry runs
(Source: DELGROSSO S.R.L. Experimental Data)

and the dry curve informations about the porous network can be obtained, such as:

- Bubble point: maximum pore diameter calculated when the first "bubble" appears due to the gas pressure i.e the first inflection point of the wet curve
- Smallest pore size: calculated at the pressure at which the dry and wet curve meet each other
- Mean flow pore diameter: Pore size at which 50 % of the total gas flow can be accounted
- Pore size distribution
- Gas permeability
- Cumulative filter flow
- Differential filter flow

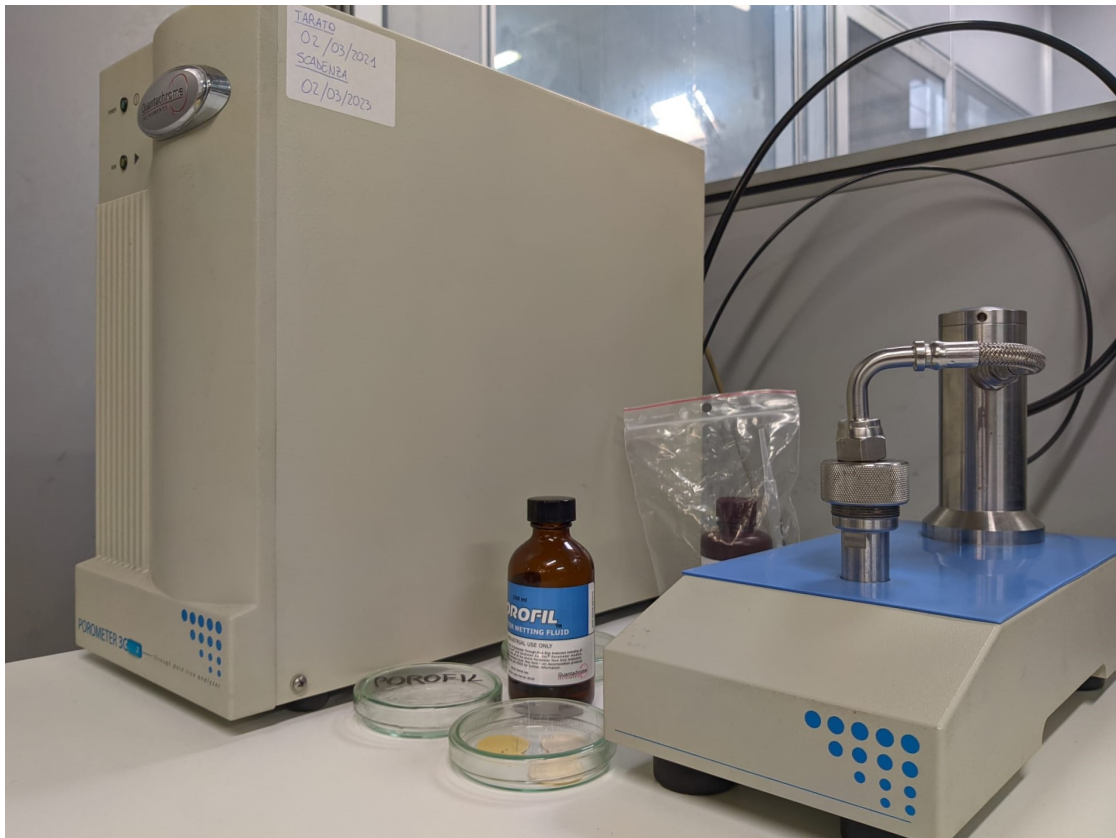


Figure 5.7: Porometer 3G test bench

- Porosity (Open area Data)

Table 5.1 shows all the necessary parameters to describe the pore structure of the filter medium. Please note that the bold value is the required parameter by FloEFD for simulations.

5.3.2 Permeability

Permeability is the most difficult parameter to derive mathematically in the filtration field. It represents a measure of the ease of a fluid passing through the filter medium and it can be defined by means of the well-known Darcy's law seen in section 3.1.4 where \mathbf{k} is the permeability tensor. The problem of predicting permeability is the selection of an appropriate model expressing \mathbf{k} in terms of other, measurable filter media properties. Historically, the first approach was based on the Kozeny-Carman model. The model assumes that the flow through a porous media can be represented by a bundle of capillary tubes of different radii whose orientation is at 45° to the surface of the medium and 45° to the

Quantachrome Porometer 3G Summary Report	
Maximum Pore Size	65.3103 μm
Mean Pore Size (MFP)	54.7081 μm
Minimum Pore Size	42.9431 μm
Bubble Point Pressure	0.0098 <i>bar</i>
Bubble Point Flow Rate	0.0067 <i>l/min</i>
Pore Density	5034 $/cm^2$
Porosity	12.077 %

Table 5.1: Experimental data summary
(Source: DELGROSSO S.R.L. Porometer Data)

flow approaching the medium. Moreover, the expended energy by the fluid in contact with the capillary surface is equal to the expended energy by the flowing fluid in contact with the real internal surface of the medium. Equation 5.4 shows how k is calculated.

$$k = \frac{1}{KS_0^2} \frac{\Phi_0^3}{(1 - \Phi_0)^2} \quad (5.4)$$

where K is the Kozeny constant that account for tortuosity of the pore structure, Φ_0 is the permeable porosity expressed as a decimal fraction of the total medium volume and S_0 is the effective surface area per unit volume of solid material. Obviously, in literature many models have been developed by reworking the Kozeny-Carman model such as Paterson, Walsh and Brace.

Due to the complexity of these equations and the microscopic approach, it is not convenient, from an engineering perspective, to calculate the permeability coefficient. Therefore, permeability behaviour is better expressed by a series of experimentally curves that show the pressure drop in relation to the fluid flow that goes through a filter medium. Generally, air is the fluid most used in the evaluation of permeability, since it does not require extremely complicated measuring equipment. An example of permeability curve (for air) is given in Figure 5.8 that shows the curve obtained from a permeability test performed on a sample of $D = 112.9 \text{ mm}$ of the filter material with thickness $t = 0.7 \text{ mm}$. The slope of the curve (straight line), by assuming μ , t , ρ and S as constants, represents the inverse of the permeability coefficient k . Moreover, an increase of the filter area will reduce the pressure drop across the filtration system, because there will be less velocity gradient.

In order to perform fluid dynamic simulations, it is necessary to assign in FloEFD the *porosity* and *permeability* parameters to the specific body which represents the filter medium element. The *porosity* value was found in the previous section.

5.4 Permeabilimeter

The permeability of a pure liquid is not as easy to be determined as the air permeability, but it requires the help of different devices that operate with the same principle as seen before. Considering that DELGROSSO S.R.L. does not have a specific equipment to measure liquid permeability, the objective of this thesis is to also design, in collaboration with the company, a simplified device in order to obtain a reliable value of the parameter under discussion. The permeability measurement instrument will be called *permeabilimeter* and the test bench (Figure 5.9) will be constituted by the following parts:

1. Quick coupling (G1/8)
2. Cap
3. O-Ring 29.82×2.62 ($\times 2$)
4. O-Ring 39.34×2.62 ($\times 2$)

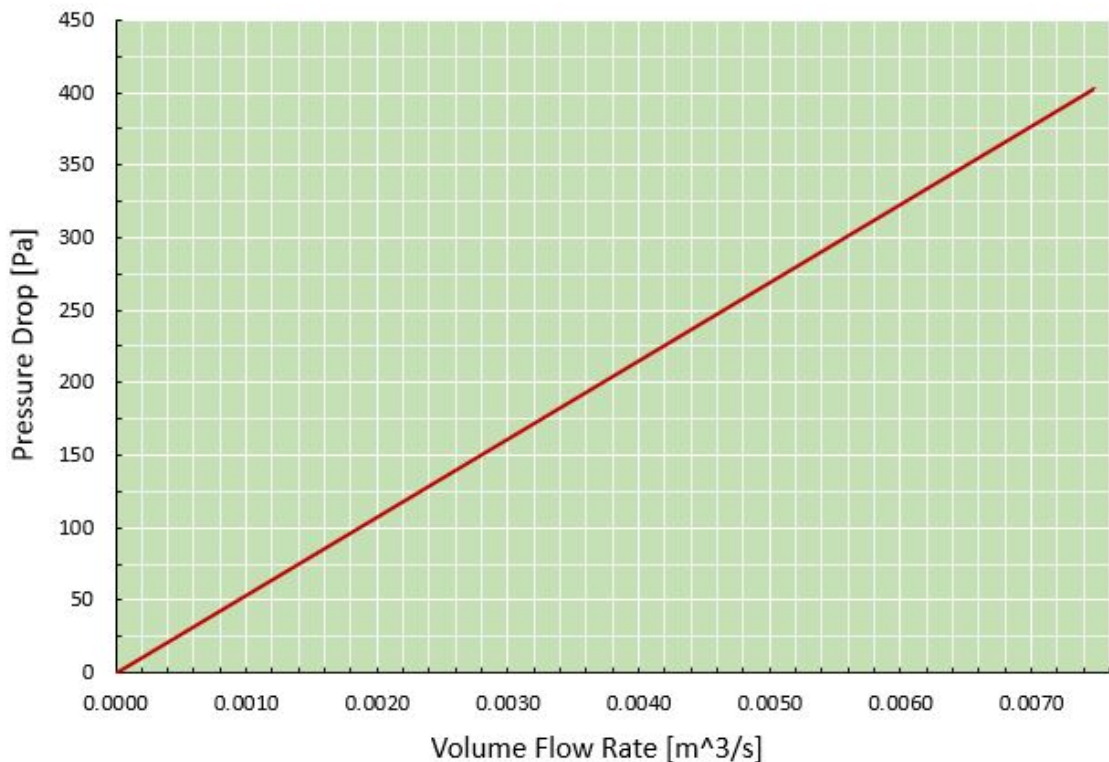


Figure 5.8: Air permeability test
(Source: DELGROSSO S.R.L.)

5. Transparent syringe ($V = 100$ ml)
6. Housing of Syringe
7. Pressure transducer ($G1/8$)
8. O-Ring 25×4
9. Filter medium sample ($D = 19$ mm, $t = 0.7$ mm)
10. Exhaust Pipe

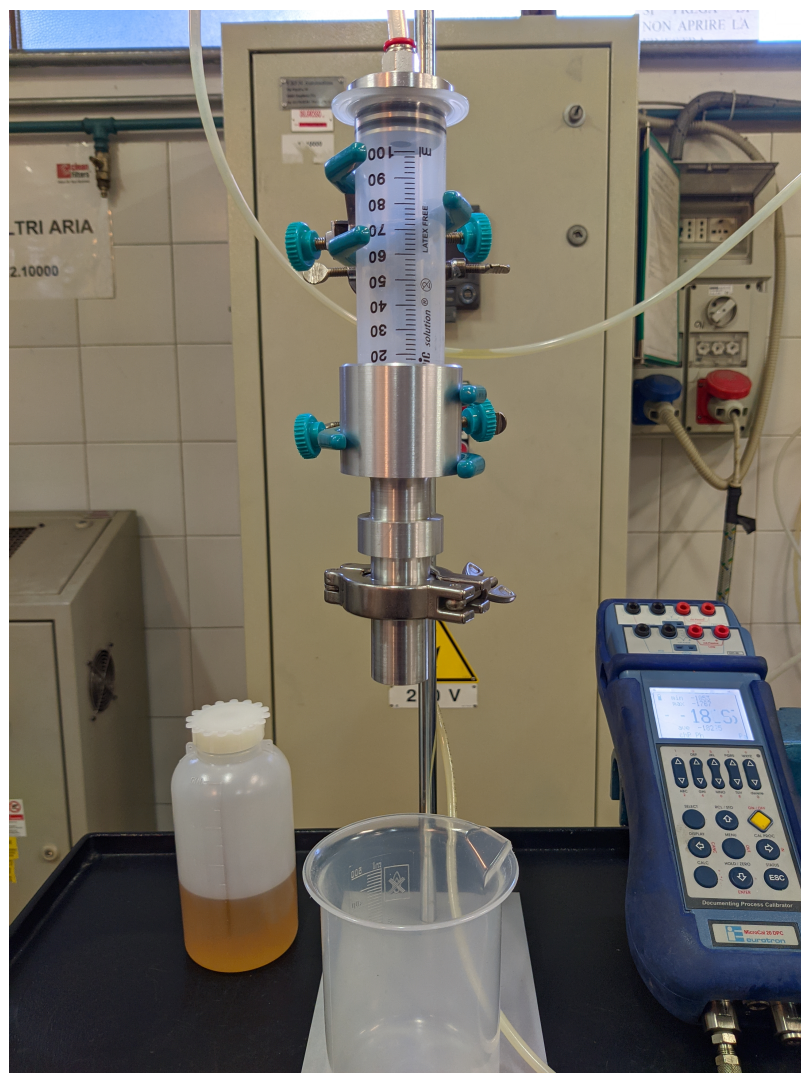


Figure 5.9: Test bench of the permeabilimeter

The pressure drop is measured by a *Microcal 20 DPC* shown in Figure 5.10 with the resolution Table 5.2.



Figure 5.10: Microcal 20 DPC

<i>RANGE</i>	<i>RESOLUTION</i>	<i>ACCURACY</i>
-100 ÷ 100 mbar	0.001 mbar	±0.025 % F.S
-500 ÷ 500 mbar	0.01 mbar	±0.025 % F.S
-0.95 ÷ 2 bar	0.01 mbar	±0.025 % F.S
0 ÷ 2 bar (ABS)	0.01 mbar	±0.025 % F.S
-0.95 ÷ 7 bar	0.1 mbar	±0.025 % F.S
-0.95 ÷ 20 bar	0.1 mbar	±0.025 % F.S
0 ÷ 20 bar (ABS)	0.1 mbar	±0.025 % F.S

Table 5.2: Microcal 20 DPC table sensitivity

Figure 5.11 and Figure 5.12 show the CAD models of both the entire assembly and all of the exploded components. In Appendix B there are all the technical drawings. In the next paragraph it will be explained the working principle of the measurement instrument and its components.

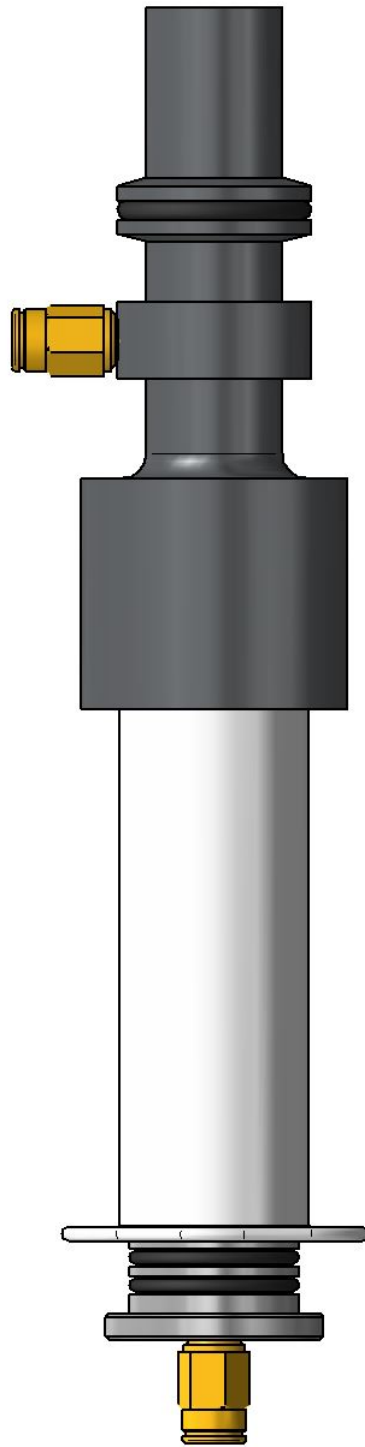


Figure 5.11: Permeabilimeter CAD model

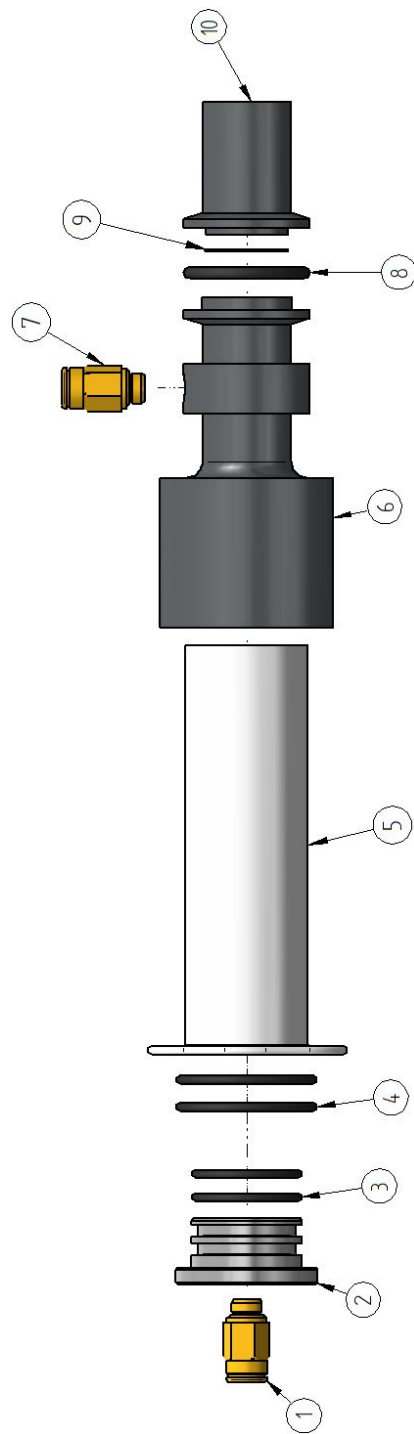


Figure 5.12: Permeabilimeter exploded view

5.4.1 Working principle

As it was previously stated, the purpose of this experiment is to provide a reliable value of permeability through the curve ΔP vs Q .

Before starting the experiment, the instrument has to be filled with *AeroShell Fluid 41* (ASF 41). Through the quick coupling (1) located on the cap (2), compressed air is injected into the system (5,6), pushing the mass of fluid previously inserted. The airflow is controlled through the use of a needle valve upstream the cap. Since the capacity of the syringe (5) is calibrated at 100 ml, it is possible to calculate volumetric flow rate of ASF 41 that is flowing, through the Equation 5.5

$$Q_{syr} = \frac{V_{100\div 20}}{t} \quad (5.5)$$

where t is the time measured with a chronometer.

Then, the fluid flow goes into the housing (6) that is designed with a specific area restriction (Figure 5.13) in order to obtain the same velocity gradient across the filtration area as the one in the oil filter object of this thesis. When the mass

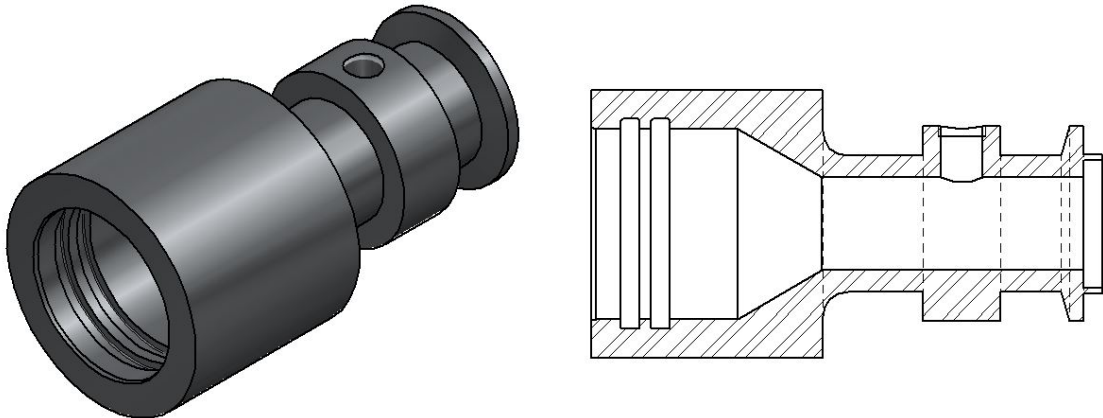


Figure 5.13: Section of syringe housing

of fluid reaches the filter sample (9) is filtered causing a pressure drop, which is measured by the pressure transducer (7). Finally, the fluid is ejected from the exhaust pipe (10). Static O-rings (3,4,8) are used in order to block any leakages of fluid, both air and ASF 41. Moreover, a V-band is used to align and hold together the housing (6) and the exhaust pipe (10), while properly designed flanges sustain the filter sample. Figure 5.14 shows the details of the particular geometry of the flange, specifically in yellow the filter sample (9) and in blue the sealing gasket.

It is important to repeat the test more than one time, in particular five times for each value of volumetric flow rate. As a result, the desired ΔP vs Q curve will

have fewer experimental errors (systematic and random) because they will be extrapolated from the average value of the obtained data.

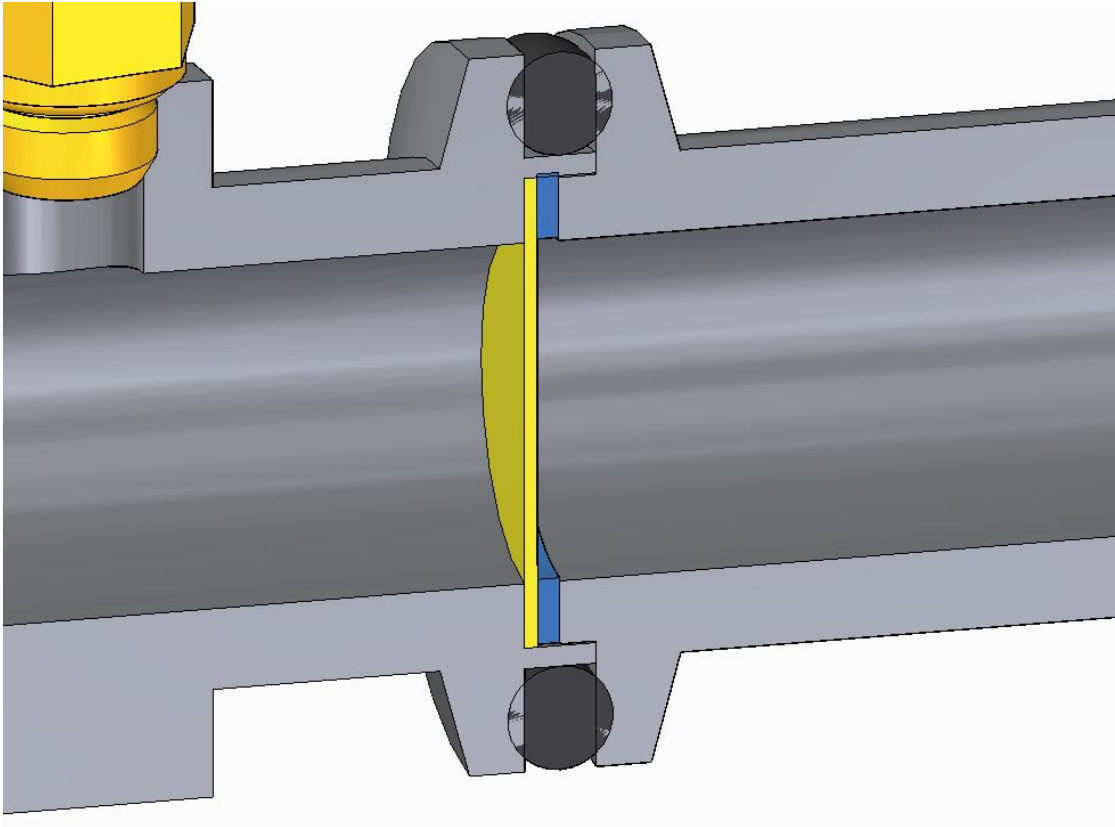


Figure 5.14: Detail of the designed flanges

The steps to follow in order to perform correctly the experimental test are:

- Step 1: Assemble partially the apparatus by not considering the V-band and exhaust pipe
- Step 2: Rotate the entire apparatus of 180 °counterclockwise
- Step 3: Fill it with ASF 41
- Step 4: Relocate the system at the initial position
- Step 5: Insert the remaining components
- Step 6: Reset pressure value on the Microcal
- Step 7: Activate the air compressor

Step 8: Measure the time that fluid takes to flow from 100 to 20 mark of the syringe

Step 9: Read pressure drop value

Step 10: Register Q and ΔP values on Excel

Step 11: Restart from Step 1

Step 12: Change airflow in order to have new Q

5.4.2 Experimental results

Once the experimental tests are performed, the following Table 5.3 and its curve (Figure 5.15) are obtained.

Permeabilimeter experimental data		
N.Test	Q_{mean} [l/min]	Δp_{mean} [kPa]
0	0	0
1	0.53	1.81
2	2.35	8.79
3	3.64	11.55
4	6.67	22.09
5	6.96	24.31
6	7.27	24.67
7	13.33	45.74

Table 5.3: Permeabilimeter experimental data
(Source: DELGROSSO S.R.L. Permeabilimeter Data)

Finally, it is possible to characterize the filter medium material, objective of this thesis, in order to start the fluid-dynamic simulations. Appendix C describes the procedure that need to be adopted in order to correctly enter the obtained data. Moreover, for the sake of simplicity, the permeability type of the chosen porous medium is the *isotropic*, which means that the medium permeability is not dependant on direction.

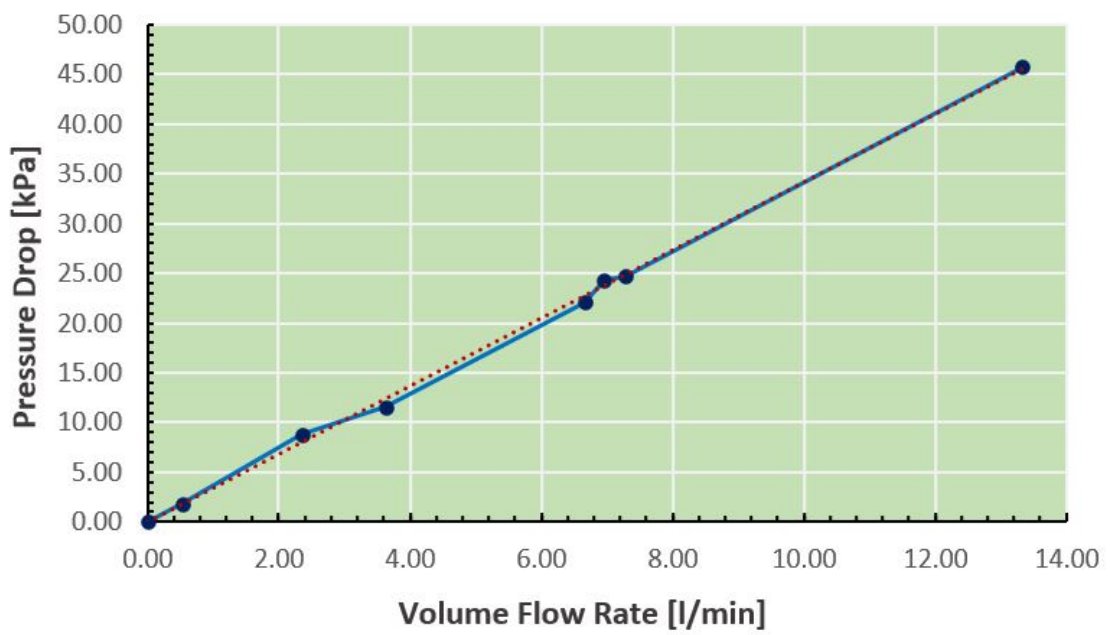


Figure 5.15: Permeability curve

5.4.3 Experiment simulation

The idea is to simulate the entire instrumental apparatus seen before and then compare it with the experimental results. The geometry of permeabilimeter assembly results complex because of the presence of elements such as the O-rings, the syringe and the V-band which do not fit perfectly within the model and there could be some leakages. Therefore, a simplified model has to be drawn, in particular all components listed in section 5.4 are linked between each other. Figure 5.16 shows a section of the simulated permeabilimeter CAD model. Since the geometry is not more complex, the fluid and computational domain includes the entire component and the auto-refined mesh option is used to define the mesh (Figure 5.17). The boundary conditions applied are:

- Volumetric flow rate to the inner surface of the intake lid
- Environment pressure to the inner surface of the outlet lid
- Porous medium condition to the filter sample

Afterwards, different simulations are carried out for different values of volumetric flow rate obtaining the curve in Figure 5.18 and the plots in Figure 5.19 and Figure 5.20. However Figure 5.21 shows the comparison between the empirical and the simulated curve. The difference between the simulated and experimental results is very small, which increase the model reliability. Moreover, the instrument is used to characterize other kinds of filter media and they are shown in Figure 5.22 classified by their composition. Figure 5.23 shows a zoomed view of the working point of the cellulose media selected for this thesis work.

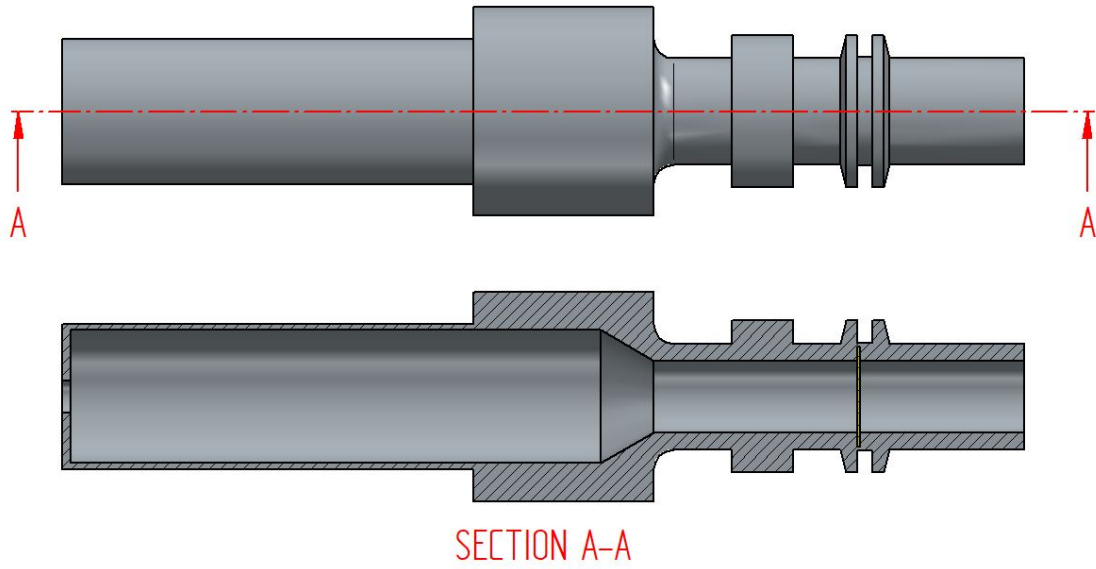


Figure 5.16: Section view of the simulated permeabilimeter CAD model

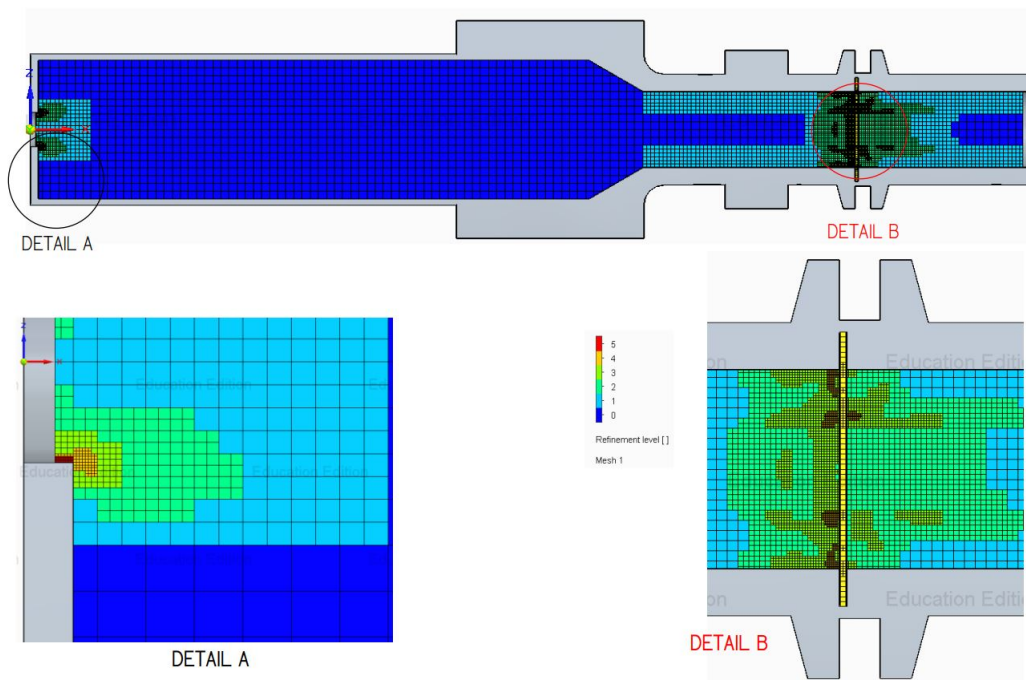


Figure 5.17: Mesh refinement of the simulated permeabilimeter model

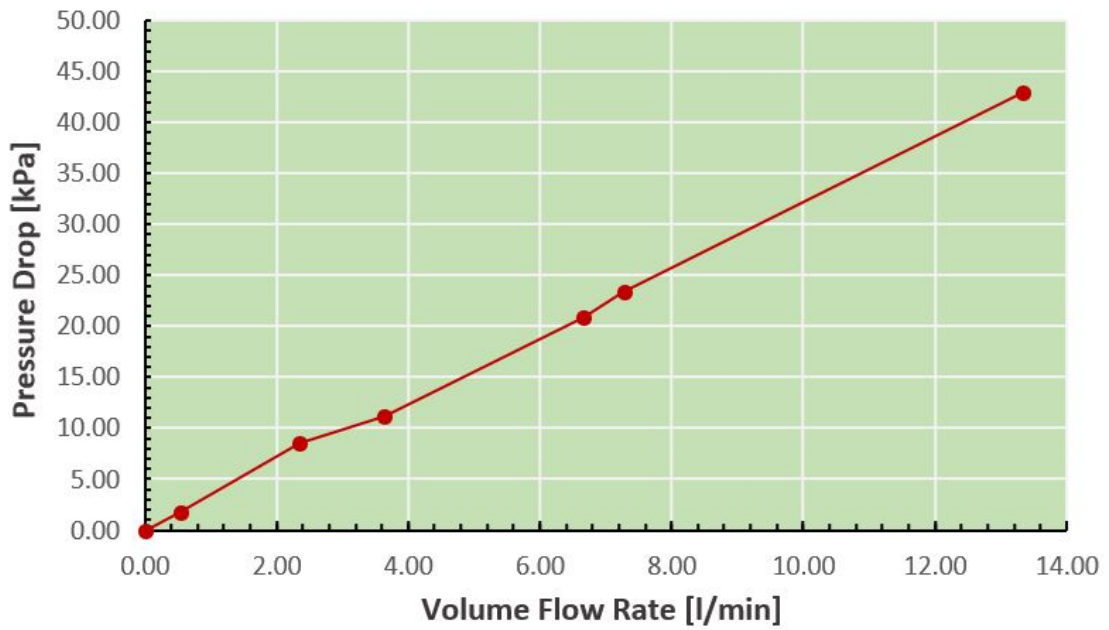


Figure 5.18: Simulated permeability curve

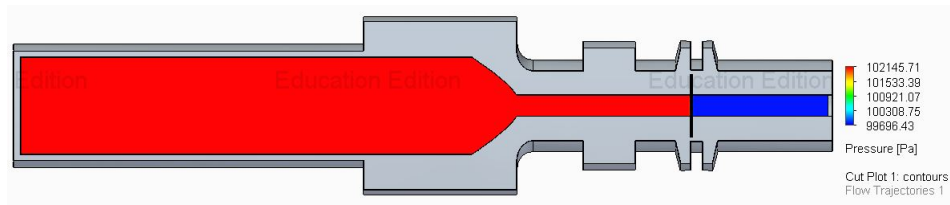


Figure 5.19: Cut plot of pressure gradient for the simulated permeabilimeter

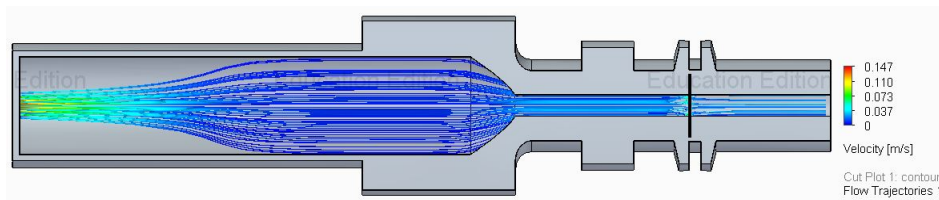


Figure 5.20: Cut plot of flow trajectories for the simulated permeabilimeter

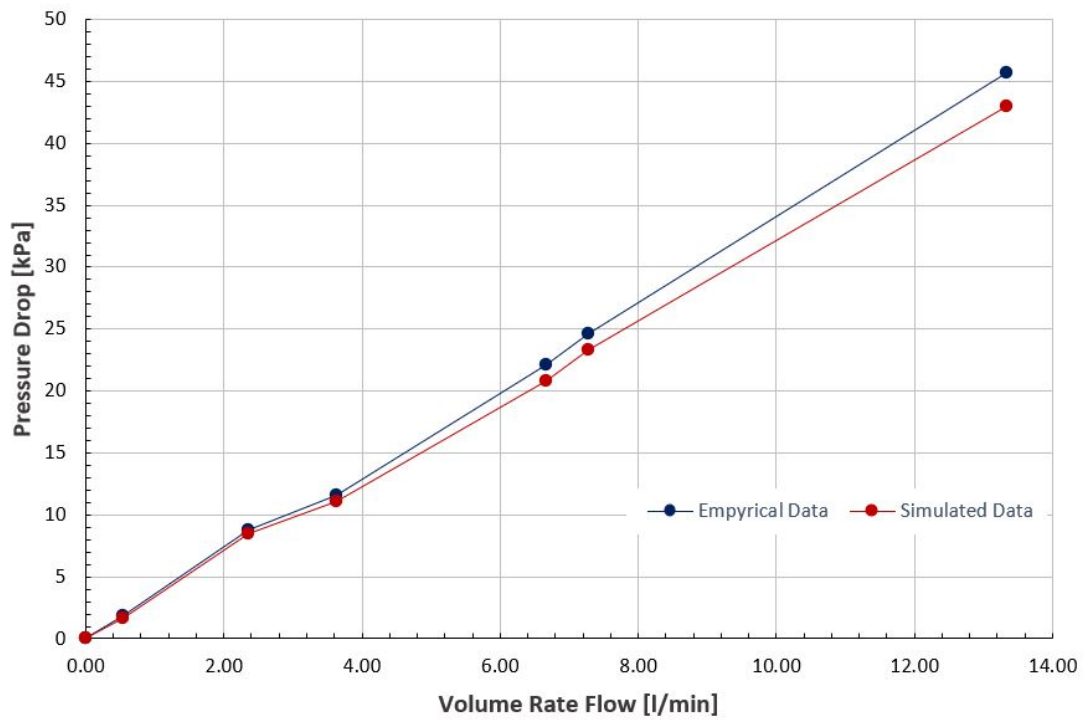
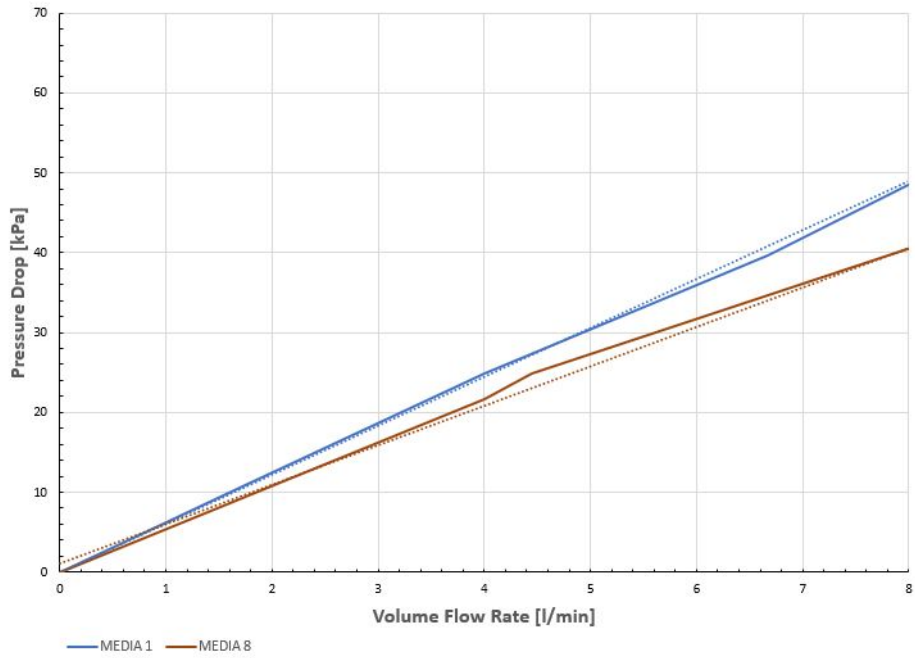
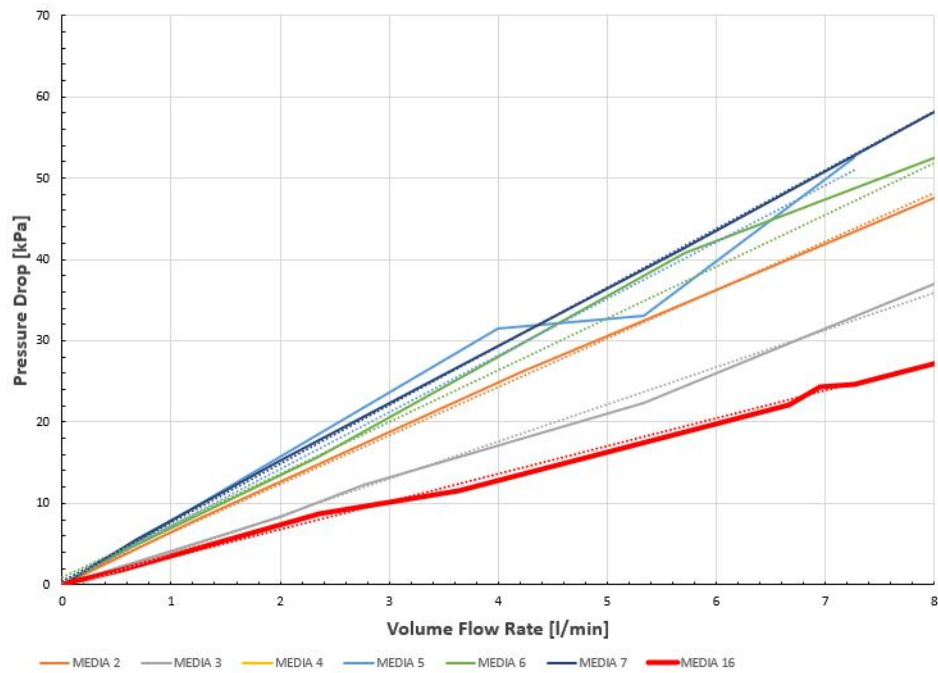


Figure 5.21: Comparison between the empirical curve and the simulated curve

Cellulose and Sintered Fibers



Cellulose



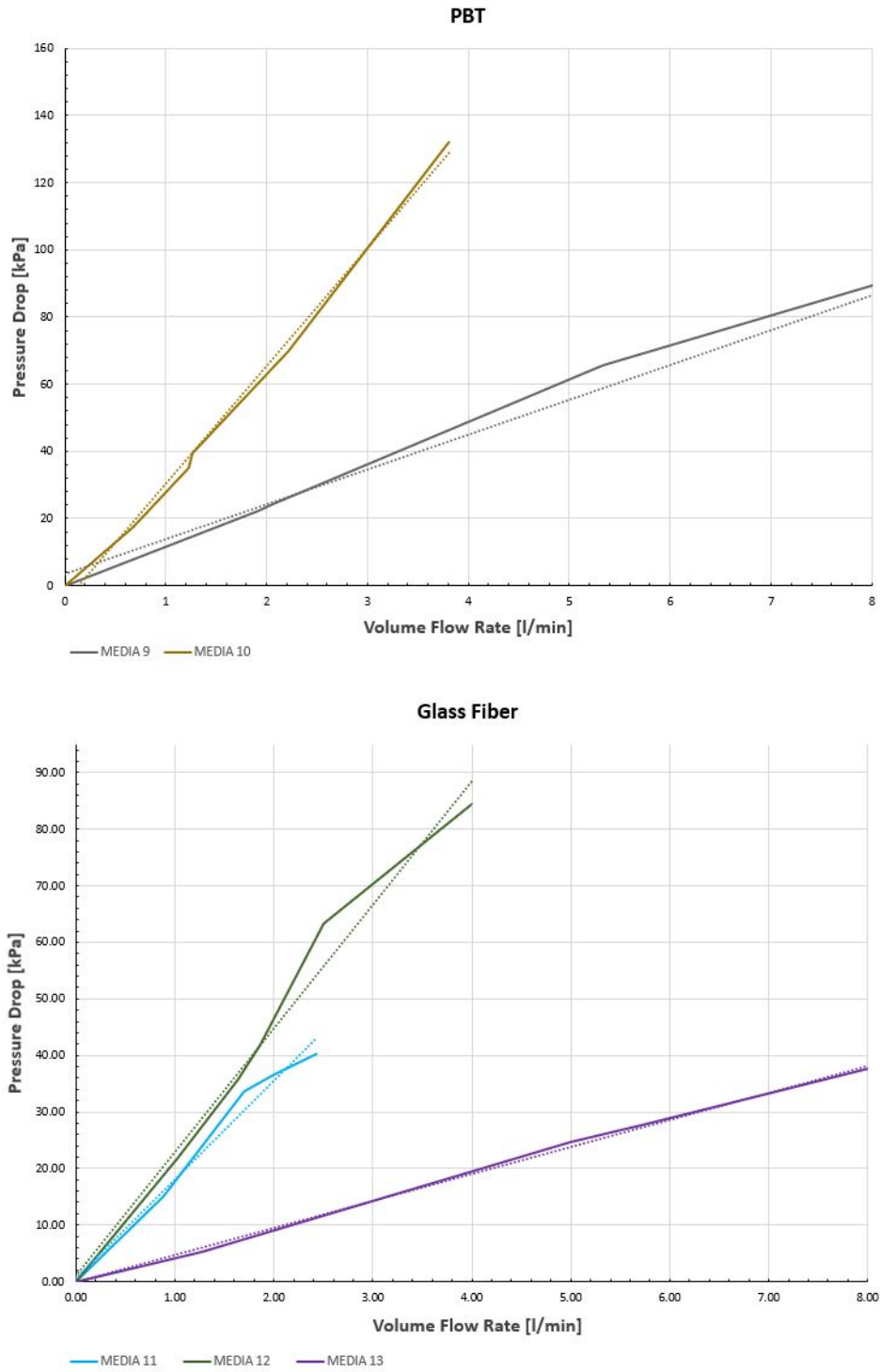


Figure 5.22: Different media permeability curves; MEDIA 16 is the selected media

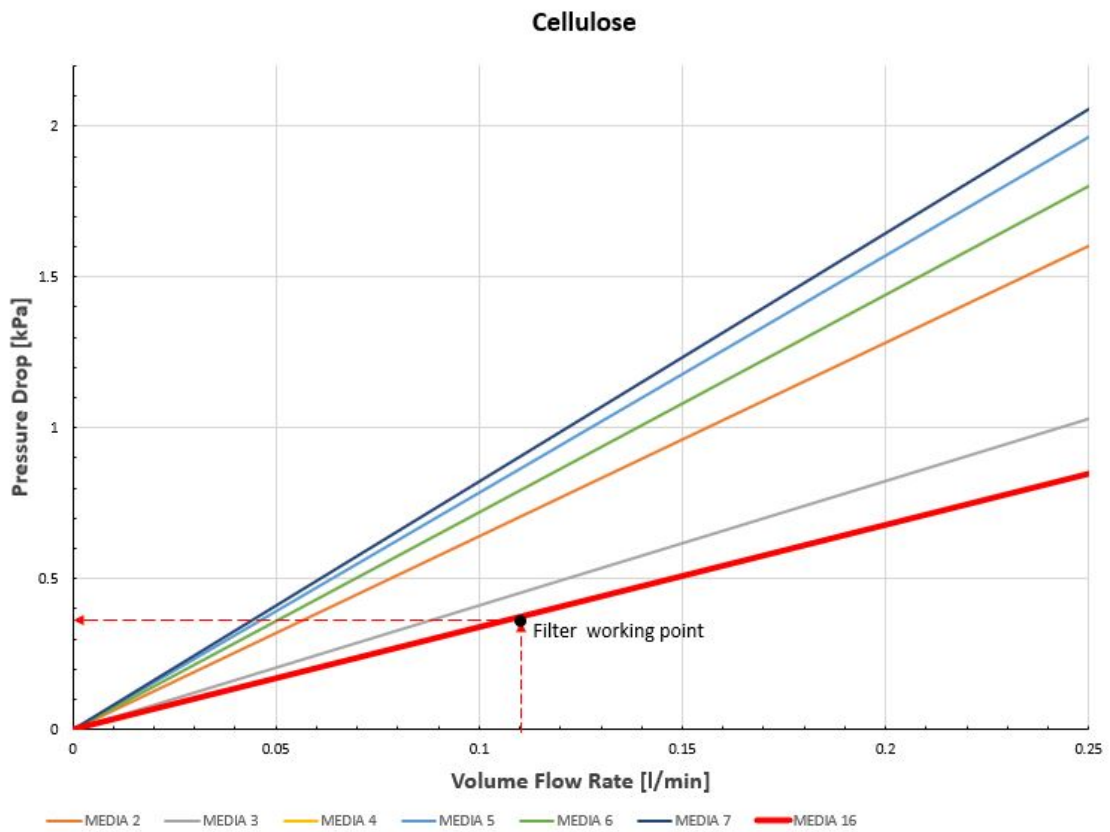


Figure 5.23: Zoomed view of cellulose media classification

5.5 Domain

The geometry is completely axial-symmetric, but due to the porous medium presence, FloEFD cannot apply the axial-symmetric condition to the selected CAD model. Moreover, the component is mirrored both in the frontal and the lateral plane (Figure 5.24). Therefore, the domain (green region) can be limited to only a quarter part of the component giving the possibility to describe the selected region in more precise way and to minimise the computational time by taking advantage of the symmetry conditions. Later on, lids will be created by selecting the planar surface that needs to be closed, and the software will automatically recognizes the fluid control volume involved in the simulations (Figure 5.25).

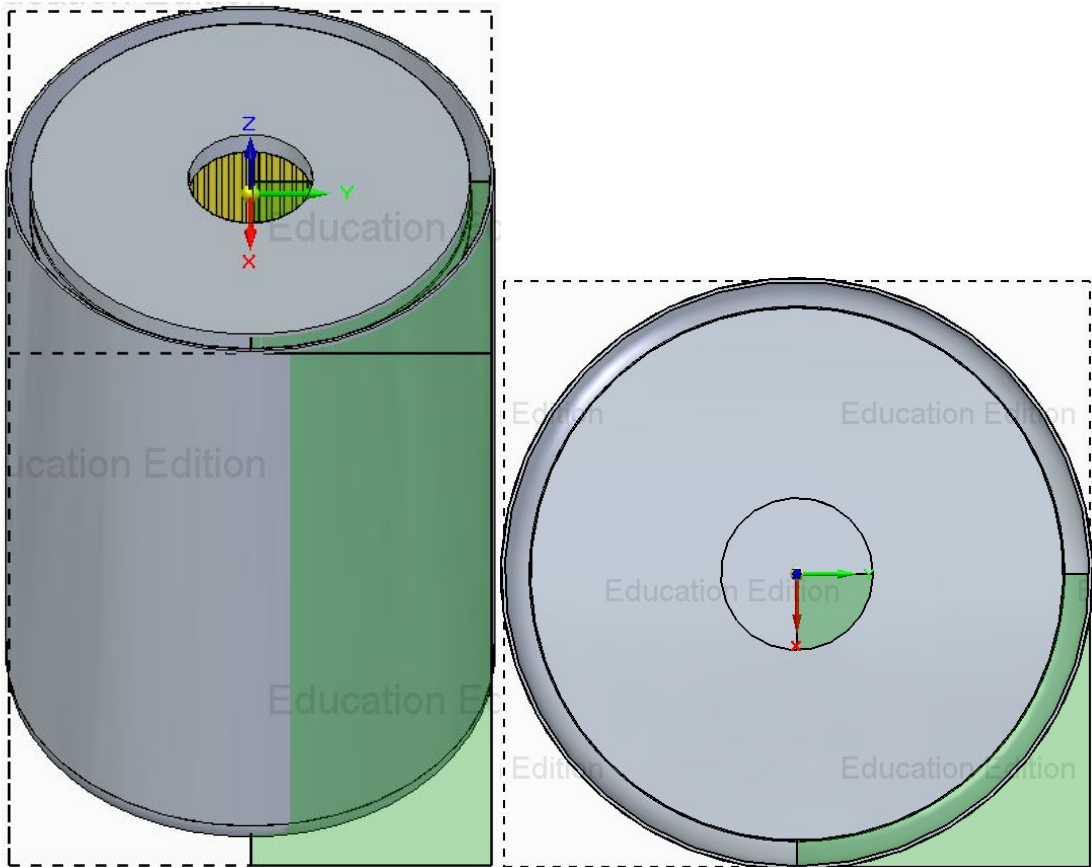


Figure 5.24: Filter medium computational domain

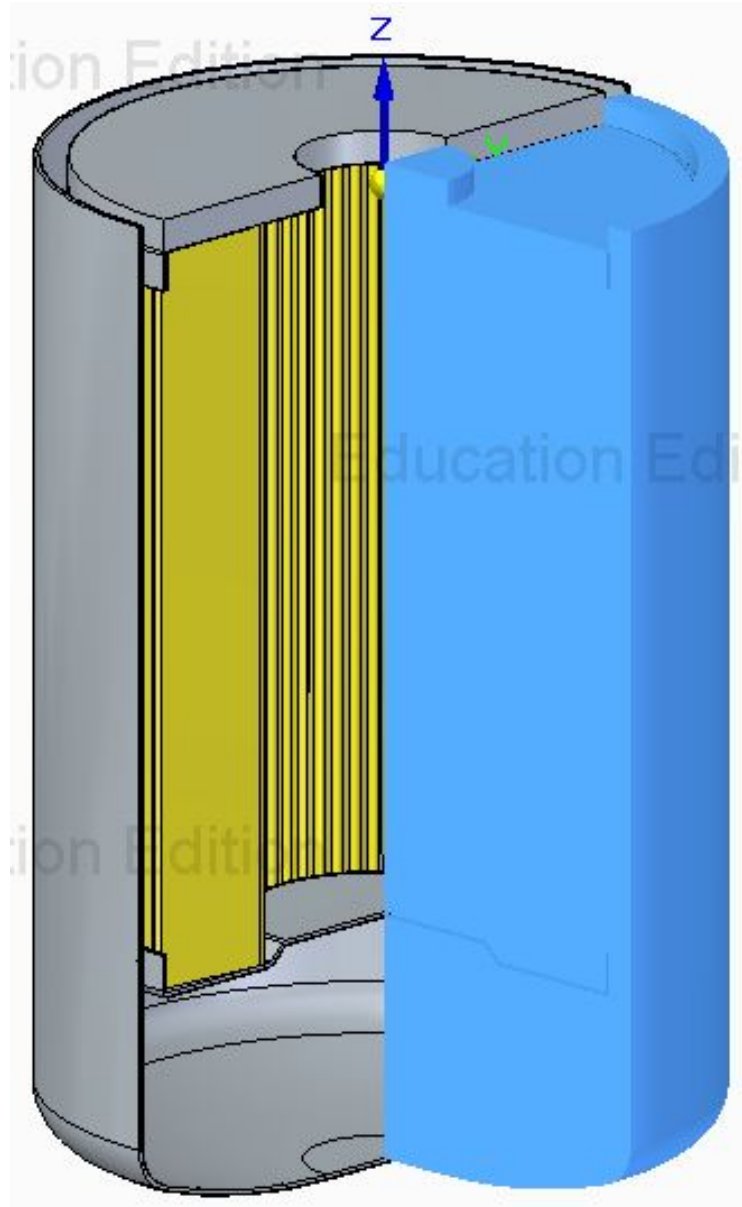


Figure 5.25: Filter medium fluid domain

5.6 Boundary Conditions

The hypothesis mentioned in section 4.3 are also valid for the filter medium CFD model under examination. Once the geometry and the model are defined, it is required to set up the boundary conditions required to perform the simulations. They are highlighted in Figure 5.26 and Figure 5.27:

- Volume Inlet Flow: $Q = 25 \frac{1}{\text{min}}$
- Static Outlet Pressure: $p_{out} = 101,325 \text{ Pa}$
- Isotropic porous media

The inlet volumetric flow rate is assigned to the inner surface of the intake lid because the volume flow rate is considered from the surface crossed by the fluid flow, while static pressure condition is considered from the inner surface of the outlet lid. Isotropic porous media is applied to the filter medium component of the assembly. Furthermore, it is important to remember that the volumetric flow rate at which the component operates is 100 l/min, but the input value of the boundary condition is divided by four because it is related to the selected domain. The boundary conditions are completed by the setting of the simulation goal. The definition of an equation goal is, precisely, the difference between the surface inlet total pressure goal and the surface outlet total pressure goal (Equation 5.6). Moreover, the equation goal is considered as the convergence criteria for finishing the simulation.

$$\Delta p_{goal} = p_{in,lid} - p_{out,lid} \quad (5.6)$$

5.7 Mesh

The generation of the mesh, that is the discretization of the control volume, is always a crucial aspect from the computational fluid dynamic point of view. In the first part (chapter 4), the mesh refinement was eased by applying the axial-symmetric domain to only one hole. This time, the subdivision of the computational domain in four symmetric parts, facilitates the mesh creation by focusing the maximum possible number of cells in only one quarter of the component. The choice of an appropriate mesh to discretize the control volume is never trivial. The presence of the porous medium generates complex patterns of the fluid flow with consequent high gradient velocity spots, especially within the pleats. This complexity presents a problem because it is difficult to create a suitable mesh for the selected component by means of the default automatic global mesh and local mesh region which can be represented by simple geometric shapes such

as a sphere, a cylinder or a cube. The most sensible course of action to take in order to have an optimal mesh for the simulations is to apply the local mesh settings to a solid body. To apply the local mesh settings to a solid component it is needed to specify this region as a solid part or sub-assembly and then disable this part in the *component control dialog*. The criterion used to define the geometry of the local mesh is based on the following procedure:

- Step 1: Define a basic global mesh
- Step 2: Start a solution-adaptive refinement: an auto-refined mesh is obtained (Figure 5.28)
- Step 3: Create a solid body based on the auto-refined mesh
- Step 4: Apply the local mesh settings to the solid body
- Step 5: Copy the same refinement level of the auto-refined mesh
- Step 6: Create the total mesh: global automatic and local mesh
- Step 7: Start the *Mesh Independence Study*

Once the basic global mesh is defined, through the solution-adaptive refinement the computational mesh cells are split until the specified refinement level is satisfied. On one hand, the use of the auto-refining option provided by FloEFD, returns good quality solutions, on the other hand it dramatically increases the number of cells and makes it so that the available RAM will not be enough for running the calculations. The only way to overcome this problem, is to manually create a local mesh that adapts itself to the auto-refined mesh.

Particular bodies are added to the assembly in order to define the regions where the mesh is going to be local and refined. Such components are drawn by considering the previous mesh as base background. Three bodies have been modeled because of the different refinement levels and they are shown in Figure 5.29. The choice of the final total mesh is carried out from the mesh independence study. The parameters changed during the study are the global refinement level and the local refinement level in the regions of interest. In Figure 5.30 it is possible to observe that the selected mesh is a good trade off between pressure drop value and computational time. Moreover, Figure 5.31 and Table 5.4 display the grade refinements of the entire component. The final chosen mesh for the simulations has:

$$N_{elements} = 1,086,664 \text{ cells}$$

Mesh	Type	Refining Grade	Small Solid	Curv.	Tol.
Global	Automatic	4	4	4	4
Local Body 1	Local	6	4	4	5
Local Body 2	Local	5	4	4	5
Local Body 3	Local	4	4	4	5

Table 5.4: Mesh specifications of filter medium

5.8 Results

In the following section all of the simulations results will be reported such as the velocity gradient plot (Figure 5.32), the pressure gradient plot (Figure 5.33) and the flow trajectories (Figure 5.34). All plots are referred to the x-y, x-z and y-z planes relating to the reference system of the assembly.

From the simulations plot, it is possible to notice that the most crucial part where pressure loss happens is at the inlet. This is due to the small area that fluid has to cross, which means that it will reach high velocities, resulting in a drop of the pressure. Moreover, there is a difference of gradient velocity plots between the y-z and z-x planes. This is due to the fact that in the first case, the cutting plane considers the inner part of the pleat while in the second it considers the external one.

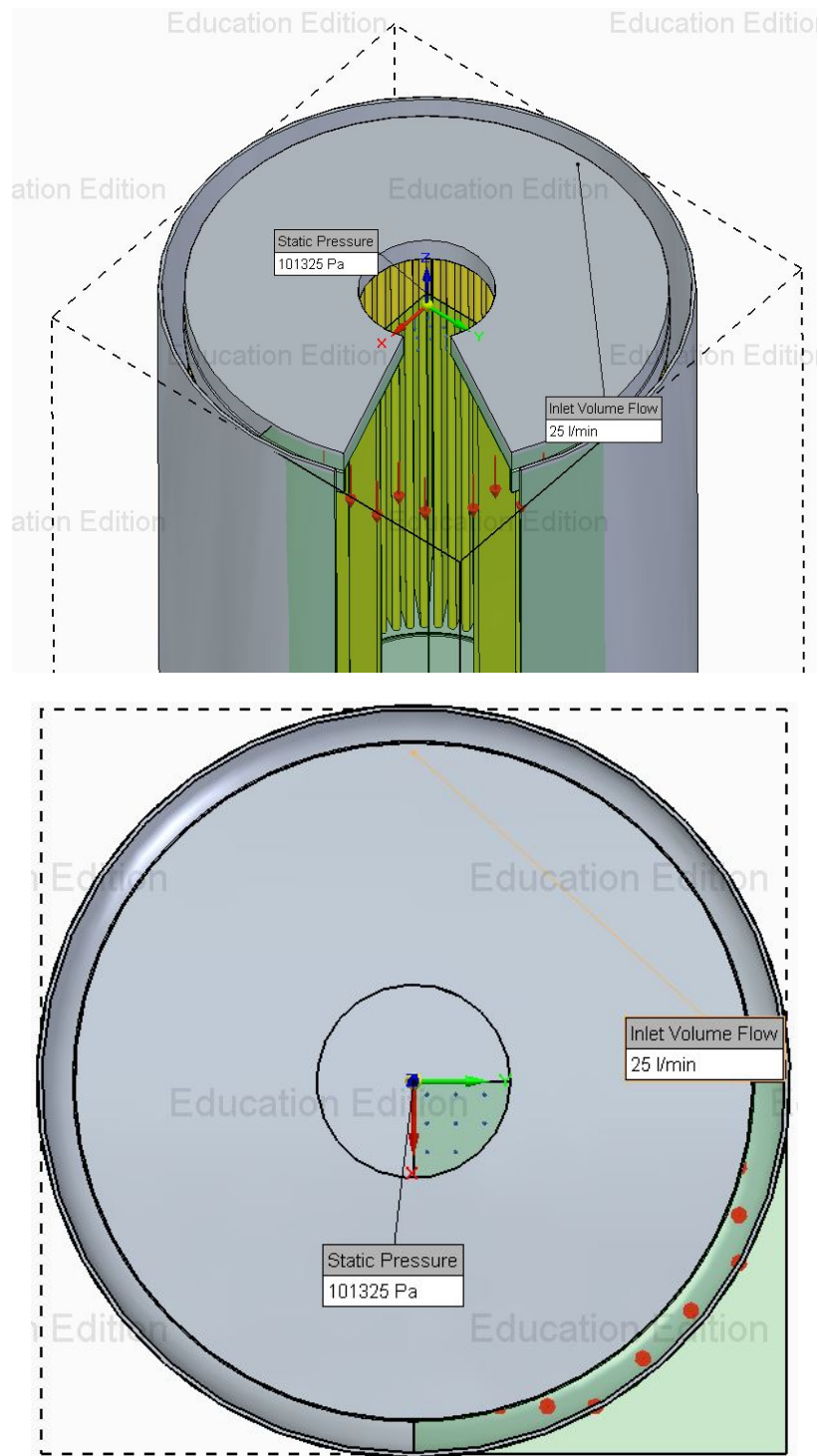


Figure 5.26: Filter medium CFD model in section and top view with boundary condition in evidence

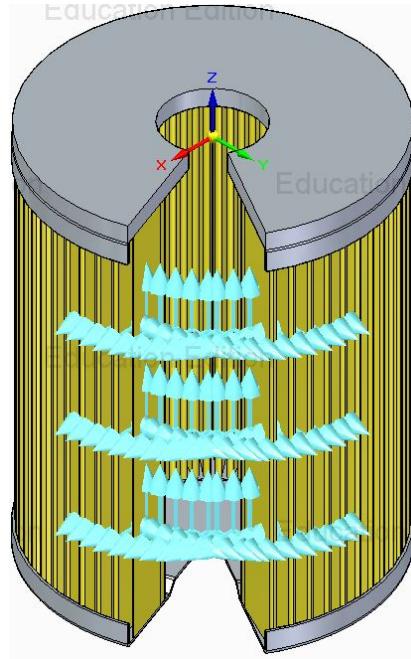


Figure 5.27: Filter medium CFD model in section with isotropic porous media condition in evidence

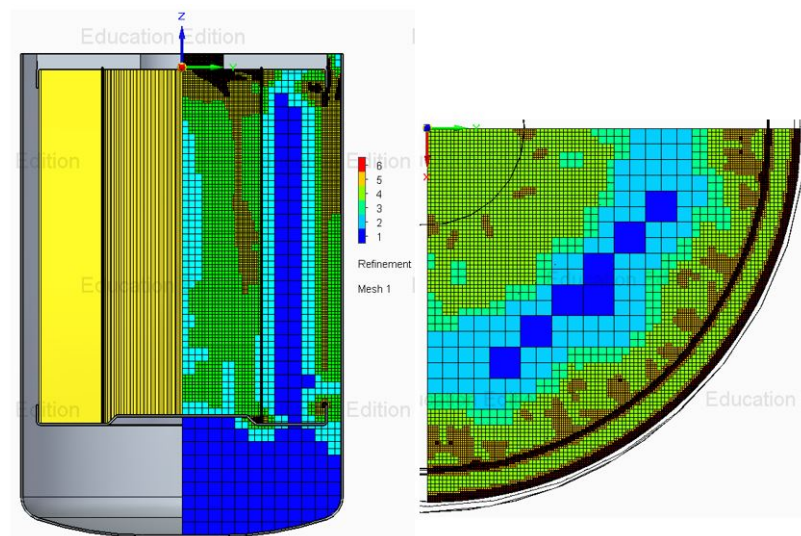


Figure 5.28: Lateral and top views of the obtained auto-refined mesh

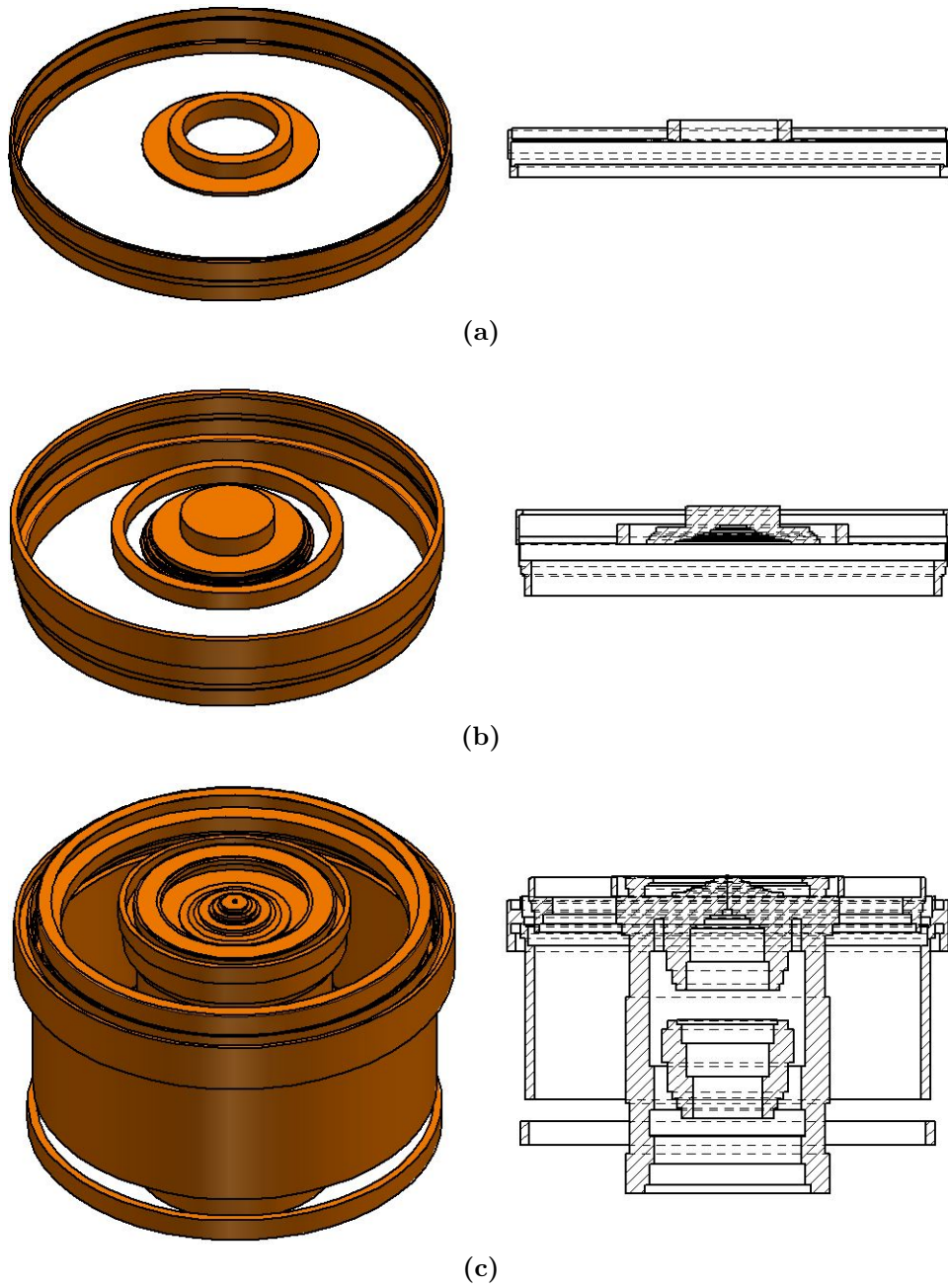
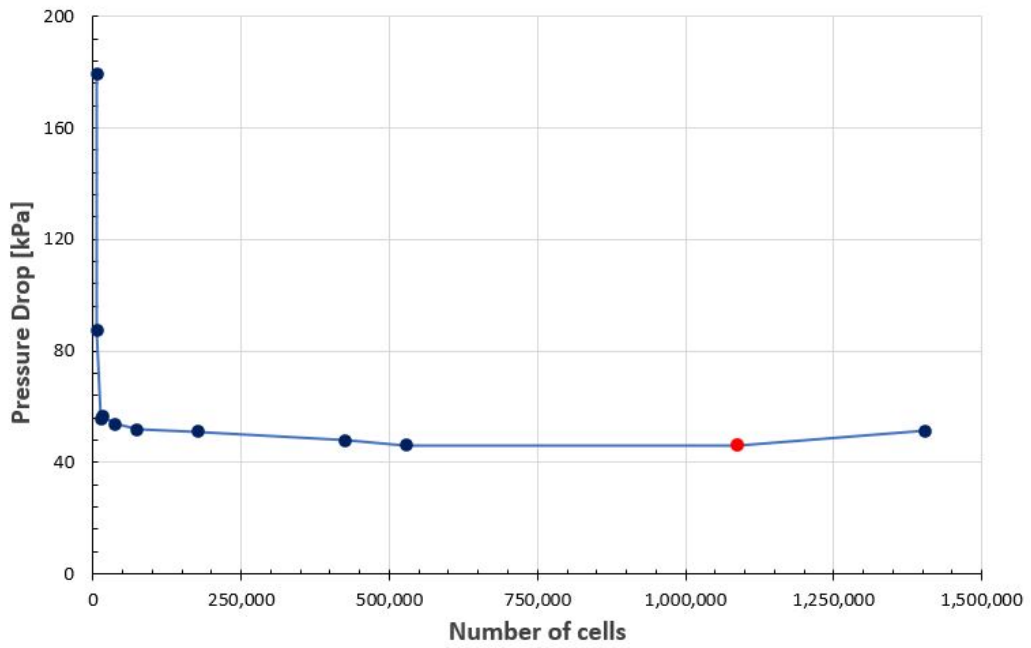
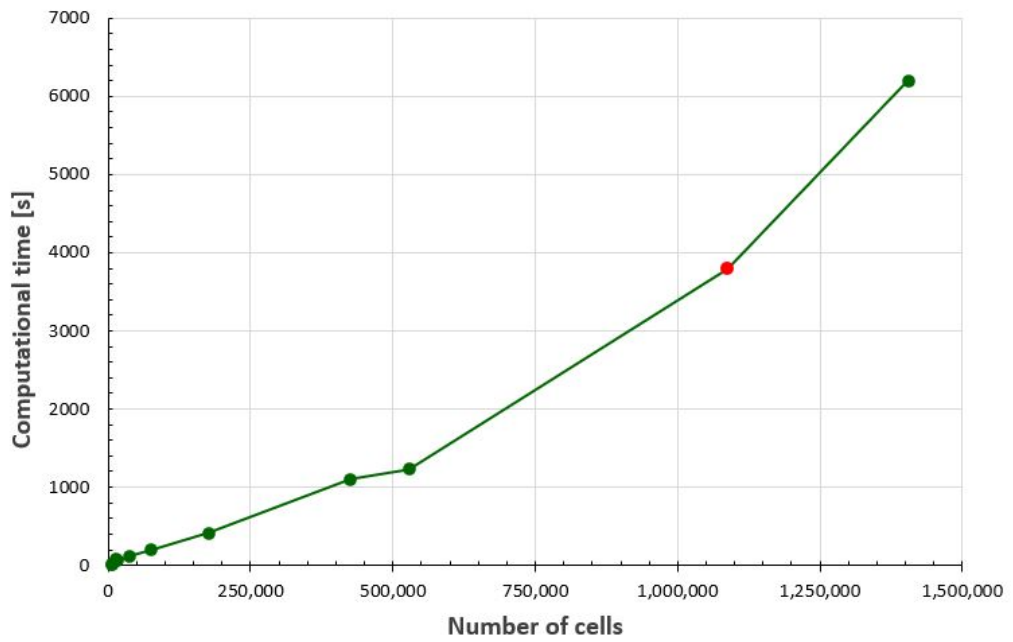


Figure 5.29: Additional bodies used to define local mesh regions
(a) Ref.level = 6 , (b) Ref.level = 5, (c) Ref.level = 4



(a)



(b)

Figure 5.30: Plots of the mesh convergence study for filter medium:
(a) Pressure loss in function of number of elements
(b) Computational time in function of number of elements

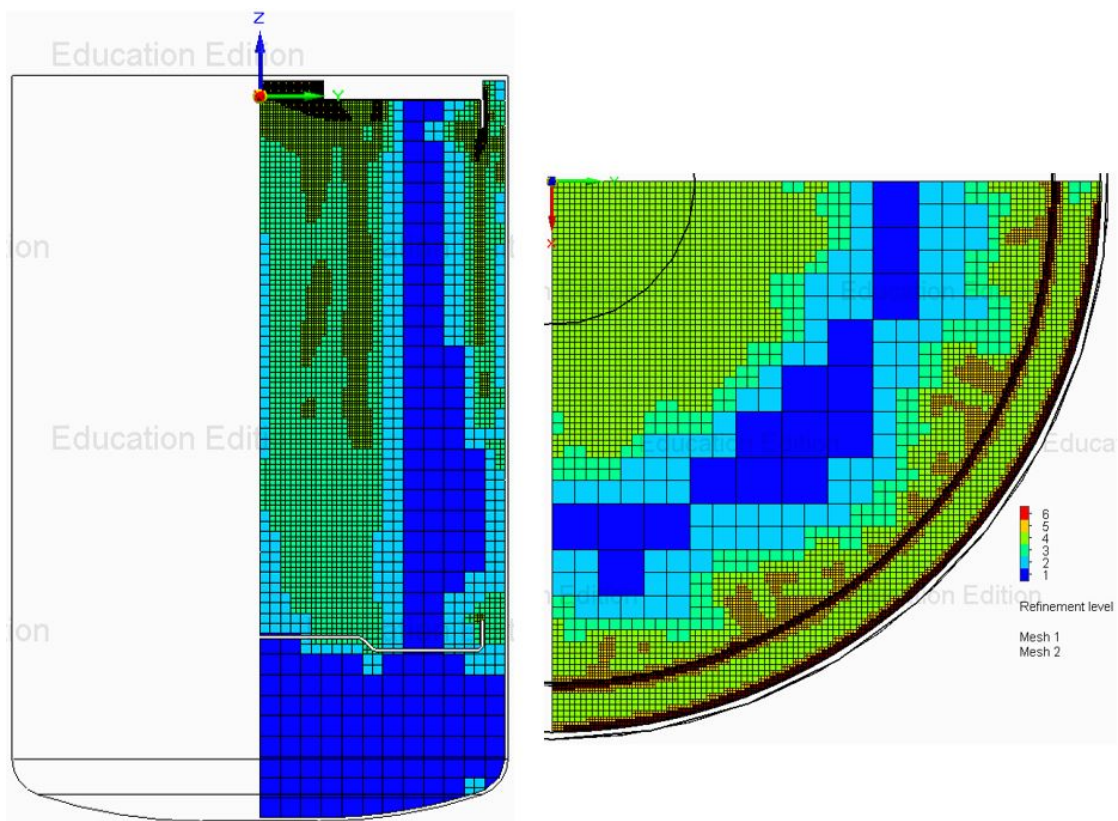


Figure 5.31: Mesh Refinement

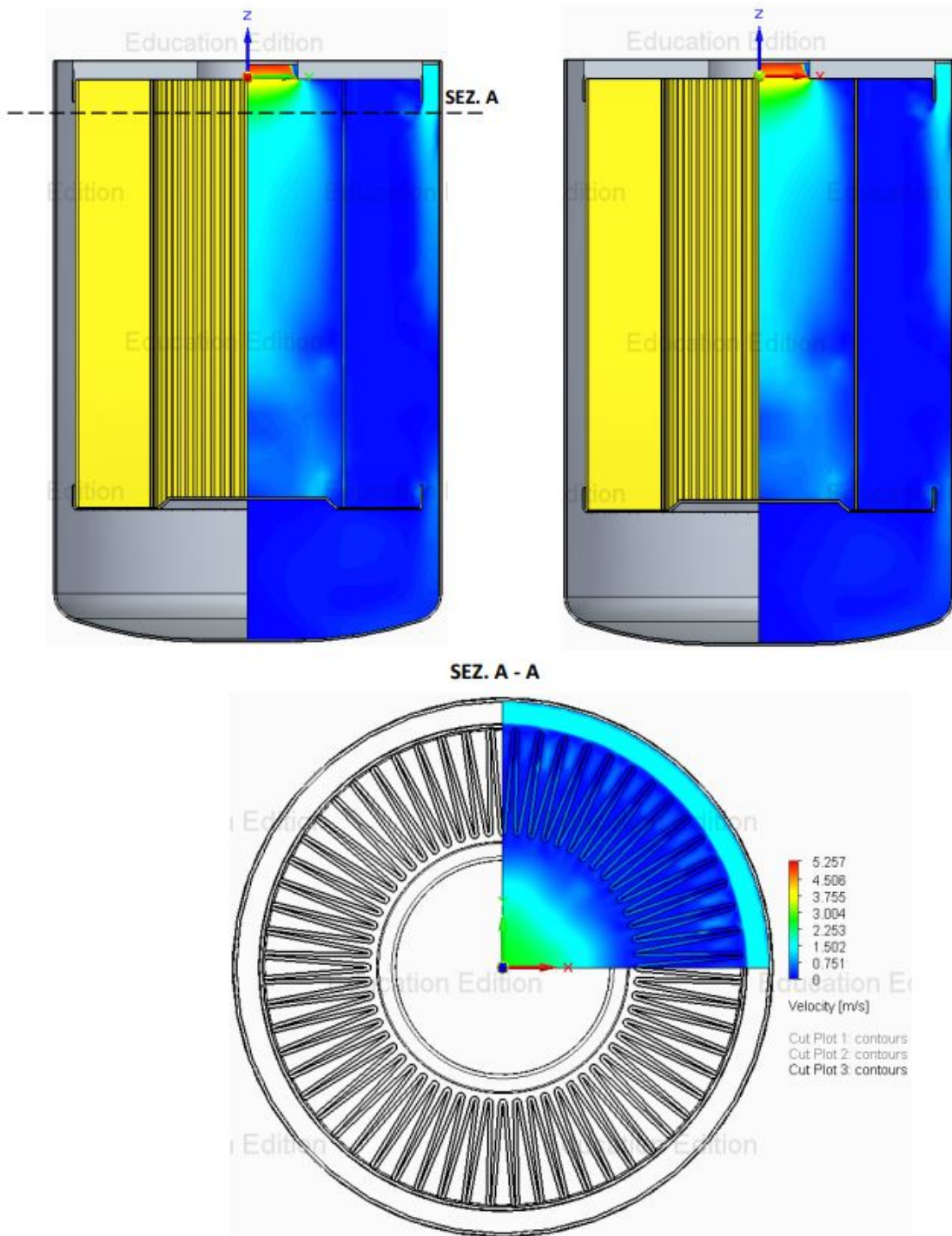


Figure 5.32: Filter medium velocity gradient cut plot

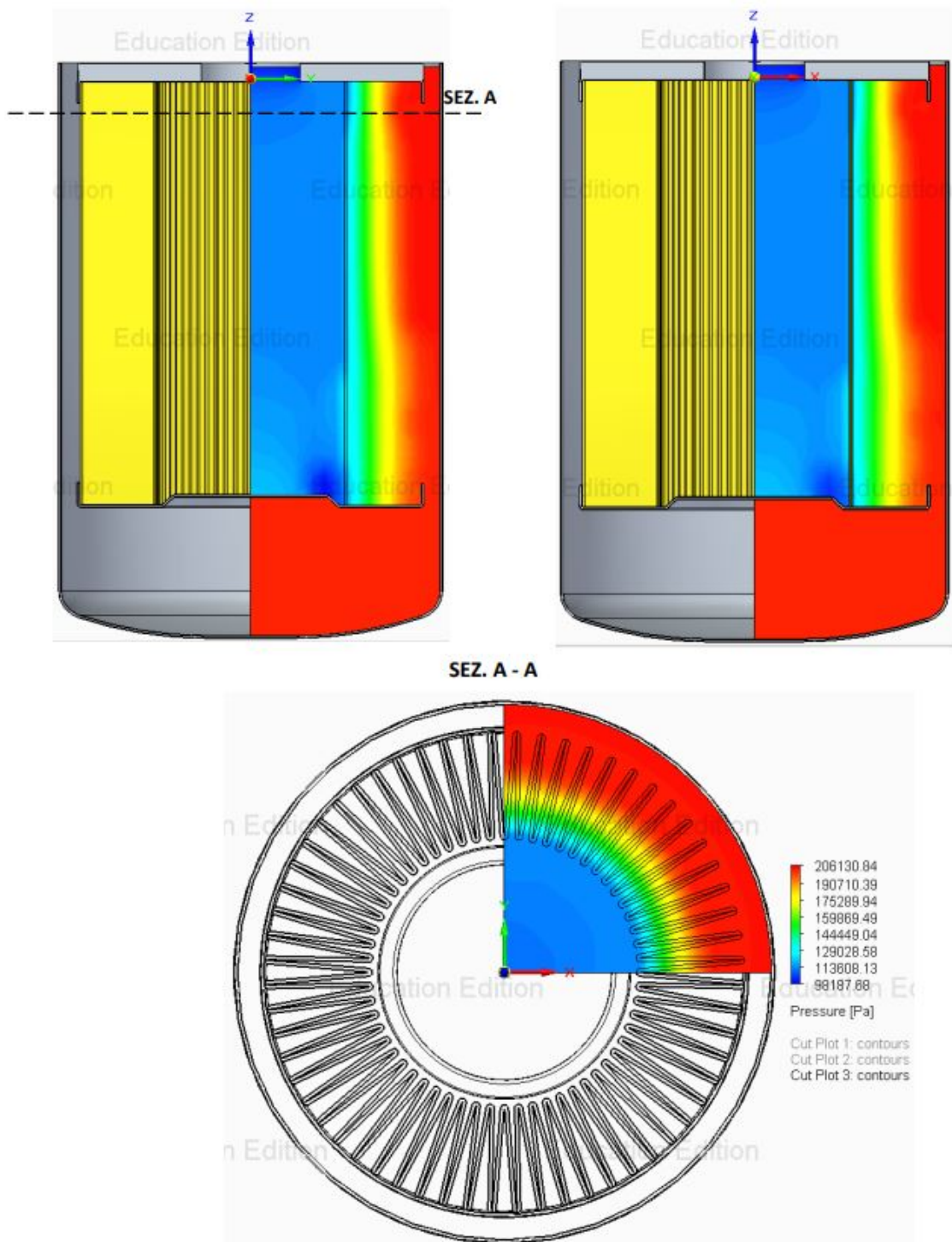


Figure 5.33: Filter medium pressure gradient cut plot

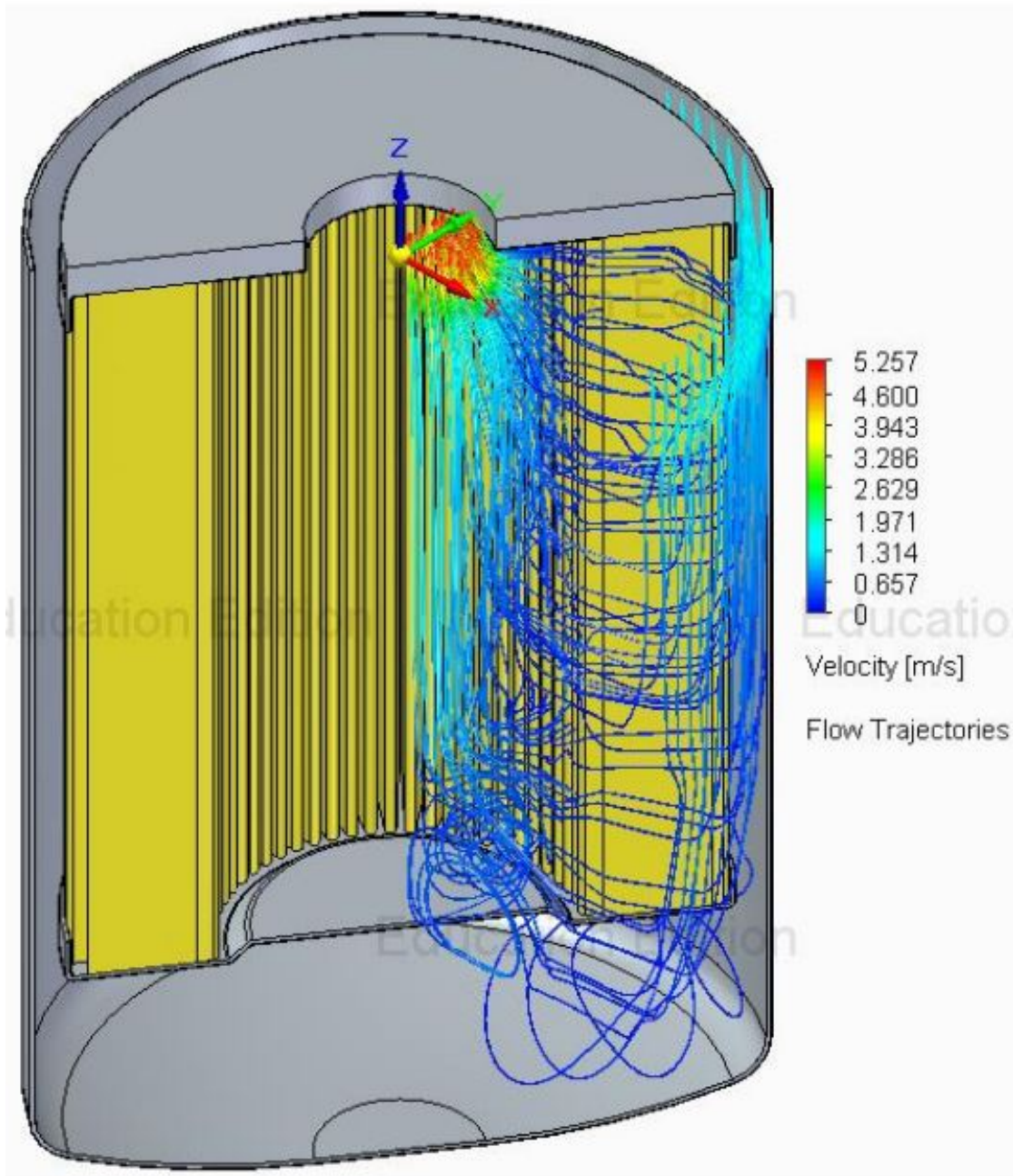


Figure 5.34: Filter medium flow trajectories

Chapter 6

Part III: Perforated Support

The third and last part that remains to be simulated of the oil filter objective of this work, is the exit port considering the metal perforated support for the filter medium. Since it is impossible to isolate and simulate only the perforated support, the only way is to consider the component analysed in the previous chapter.

The contribution on the pressure loss, will consider both the filter medium and the perforated support, i.e:

$$\Delta p_{partIII} = \Delta p_{support} + \Delta p_{medium}$$

6.1 Geometry

The real perforated support of the selected oil filter has a geometry that is difficult to draw in Solid Edge. Therefore, it is chosen an easier CAD model to design and simulate, which is different from the real one. From experimental data, the more complex support (Figure 6.1) has a value of pressure drop lower than the chosen one, which means that the CFD simulations will overestimate the pressure loss of the entire filter. The CAD geometry of the support is a cylinder perforated with 330 holes and each hole is located 9 mm equidistant from the others on both x and z axes. The model was sketched as a honeycomb, therefore there are 165 holes in a step of 9 mm and 165 more half step below the previous

ones. The structure has the following parameters:

$$\begin{aligned} D_{hole} &= 3 \text{ mm} \\ h_{supp} &= 105 \text{ mm} \\ D_{supp} &= 45.5 \text{ mm} \\ Step &= 9 \text{ mm} \\ N_{holes,x} &= 15 \\ N_{holes,z} &= 11 \end{aligned}$$

Figure 6.2 shows a section of the perforated component, while Figure 6.3 displays the full assembly section.



Figure 6.1: Perforated support of the real filter

6.2 Domain

The model and domain (both computational and fluid) definition is the same as the one in the previous chapter (section 5.5). Therefore, only 1/4 of the component will be simulated. The only difference is the presence of the perforated support in the assembly, which implies an increase of control volume that has to be discretized and an increase of the computational time.

Figure 6.4 shows the computational domain considered, while Figure 6.5 shows the volume occupied by the ASF 41 fluid.

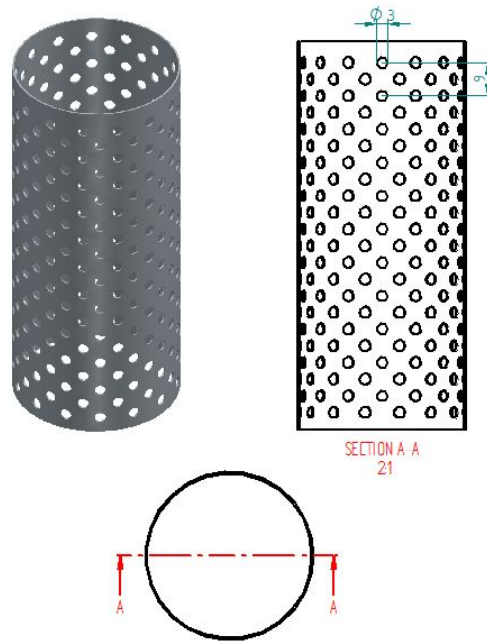


Figure 6.2: Section of the perforated support

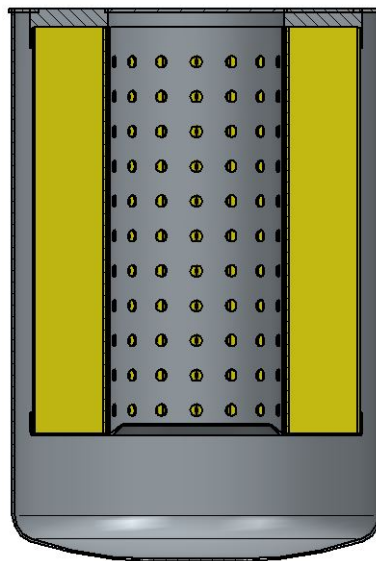


Figure 6.3: Section of the perforated support with filter medium

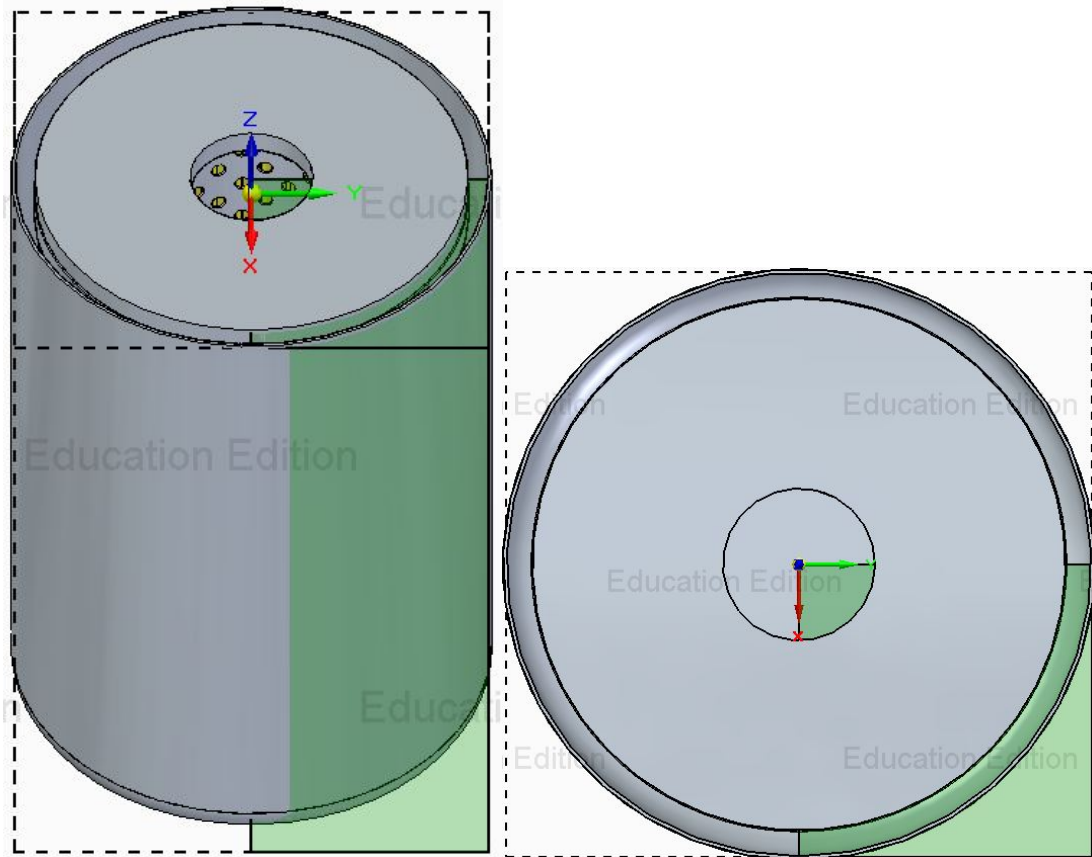


Figure 6.4: Perforated support computational domain

6.3 Boundary Conditions

The boundary conditions set-up is performed in the same way as it is done in filter medium model. In order to compute the pressure loss between the same inlet and outlet lids, an inlet volumetric flow rate is assigned to the internal surface of the intake lid, and static pressure level is assigned to the internal surface of the outlet lid (Figure 6.6). This model's equation goal is defined as Equation 5.6 as well.

6.4 Mesh

Since the geometry of the domain is changed (due to the metallic support), the control volume discretization will be different. It is expected that the regions with the most critical points will be close to the exhaust holes because of the

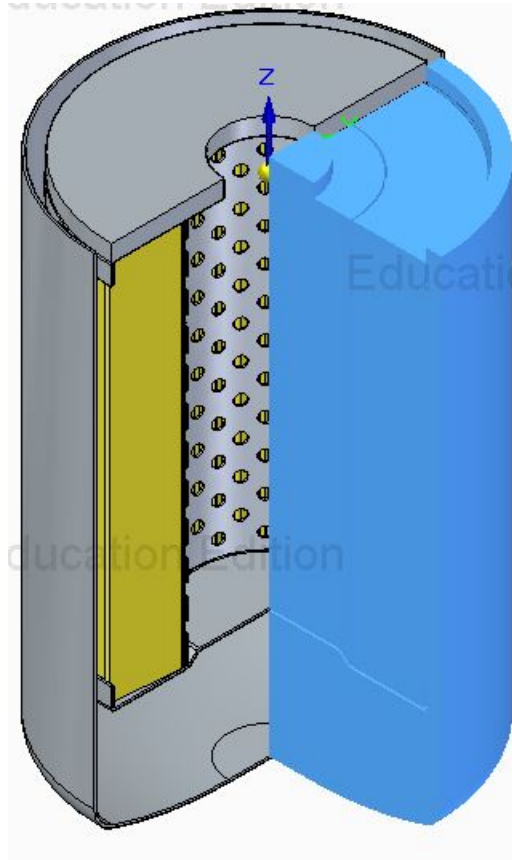


Figure 6.5: Section view of the perforated support fluid domain

suddenly reduction of the area. Therefore, it is not possible to apply the mesh in Figure 5.31. In order to define an appropriate mesh to the selected component, the same refinement principle used in the previous chapters is adopted, which means:

- Step 1: Define the basic global mesh
- Step 2: Start a solution-adaptive refinement: an auto-refined mesh is obtained
- Step 3: Create a solid body based on the auto-refined mesh
- Step 4: Apply the local mesh settings to the solid body
- Step 5: Copy the same refinement level of the auto-refined mesh
- Step 6: Create total mesh: global automatic and local mesh

Step 7: Start the *Mesh Independence Study*

The auto-refined mesh obtained from the FloEFD solution-adaptive refinement is illustrated in Figure 6.7, it shows both the lateral view and a section top view of the first hole (Figure 6.8). In this case, it is important to observe that the higher grade of refinement is located where the exhaust holes are present. The addition of the solid bodies (Figure 6.9) is needed to discretize better the control volume near the holes. Once the local mesh is defined, the mesh independence study is performed (Figure 6.10) and the following mesh is obtained with the specific grade of refinements listed in Table 6.1 and:

$$N_{elements} = 1,651,106 \text{ cells.}$$

Mesh	Type	Refining Grade	Small Solid	Curv.	Tol.
Global	Automatic	4	4	4	4
Local Body 1	Local	5	4	4	5
Local Body 2	Local	4	4	4	5

Table 6.1: Mesh specifications of perforated support case

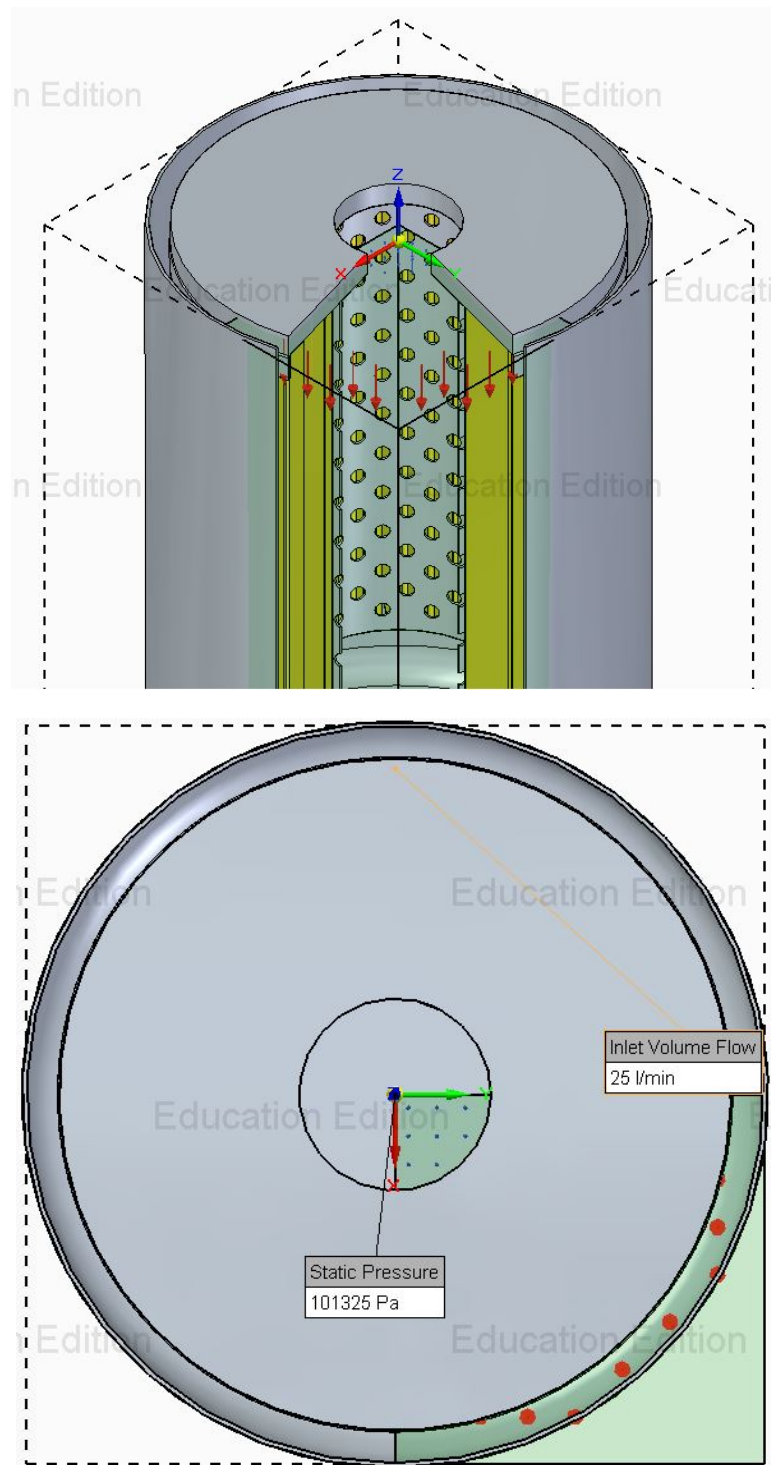


Figure 6.6: Perforated support model in section and top view with boundary condition in evidence

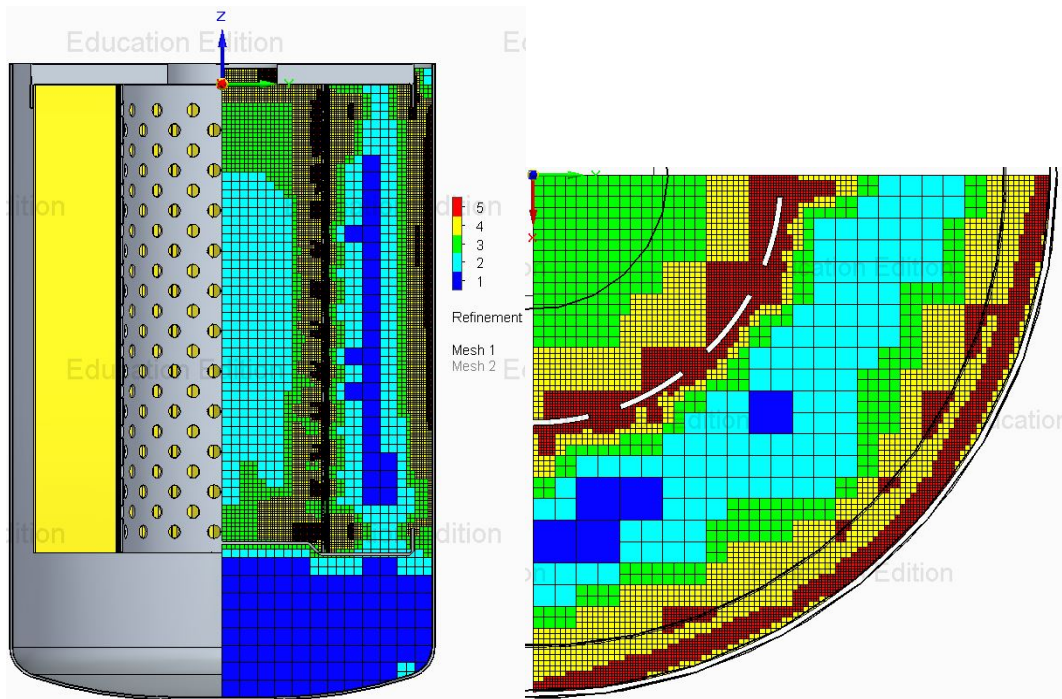


Figure 6.7: Perforated support model in section and top view with boundary condition in evidence

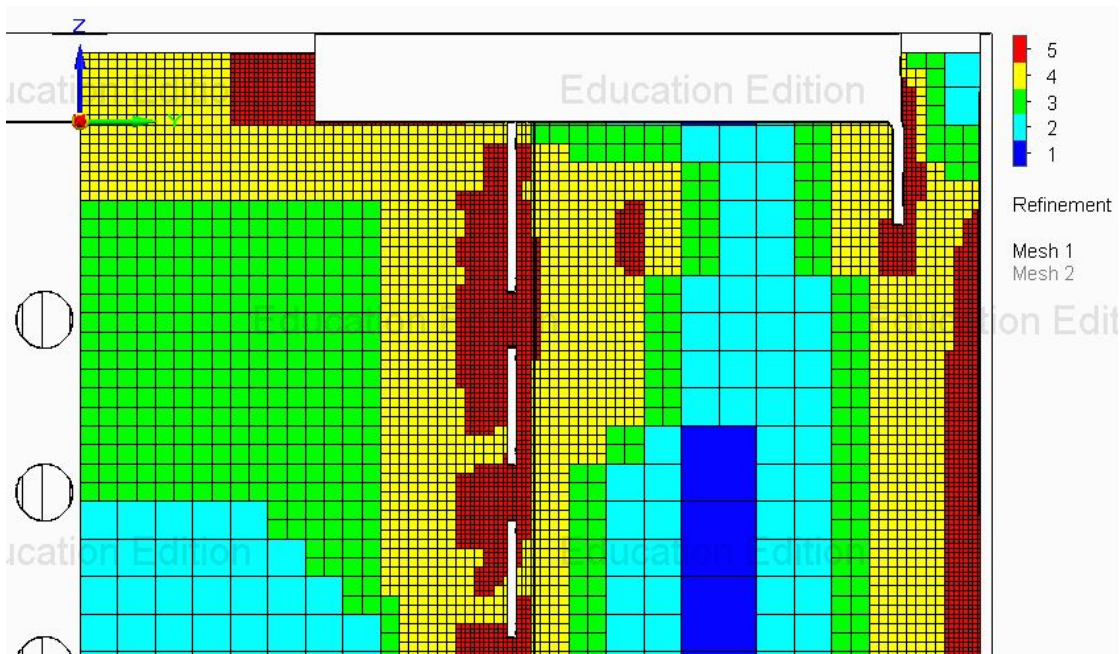


Figure 6.8: Detail of mesh refinement of a hole

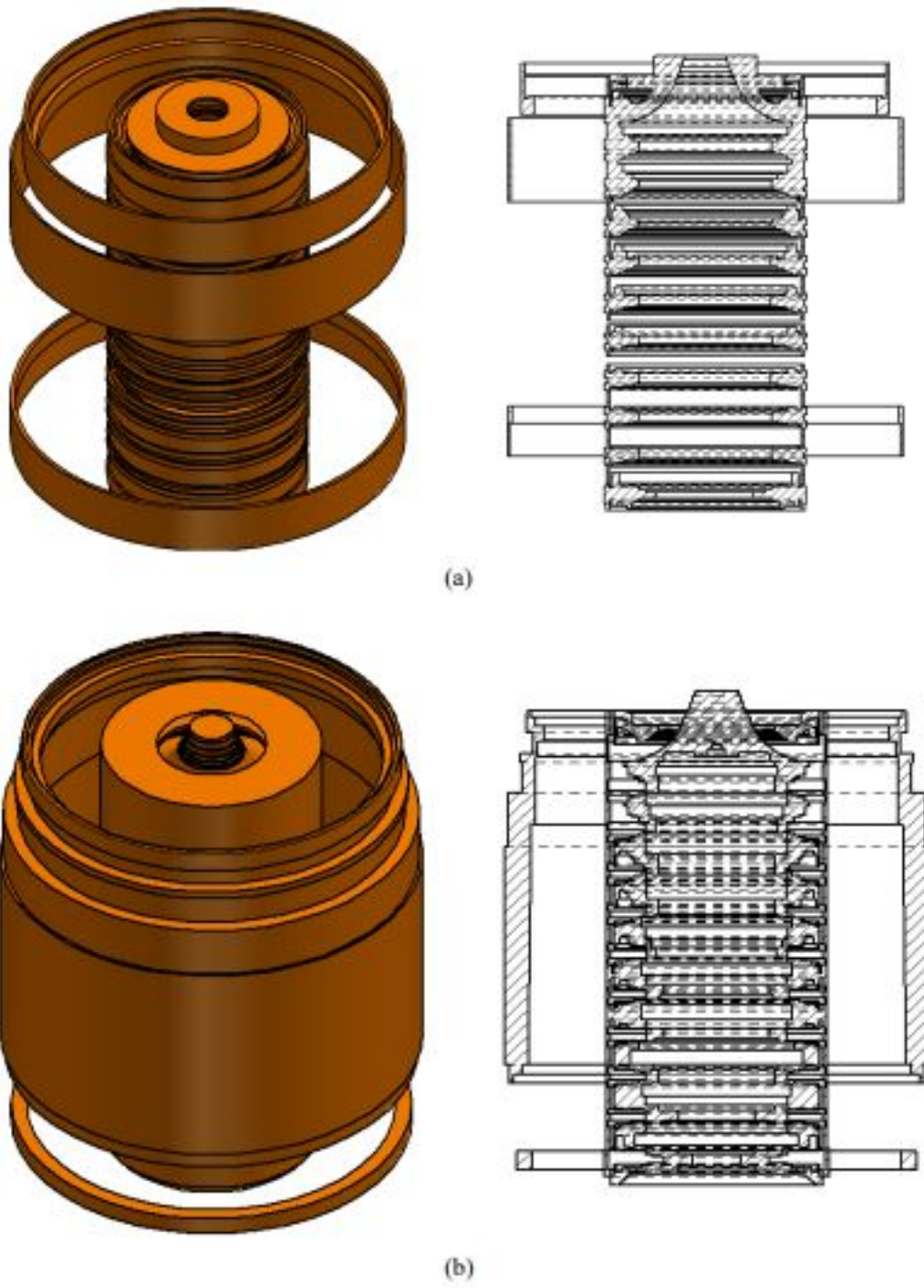
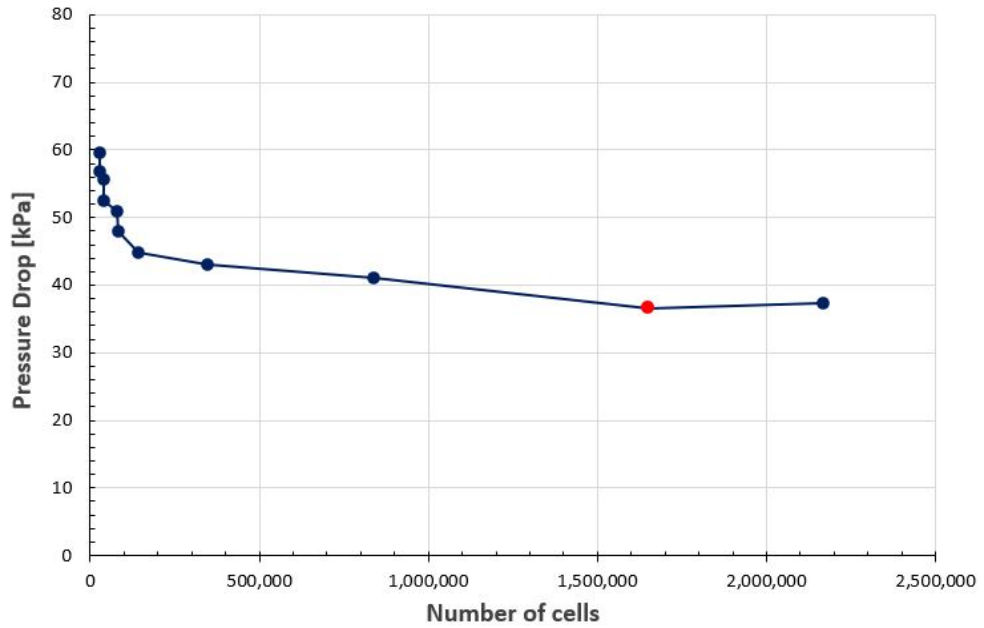
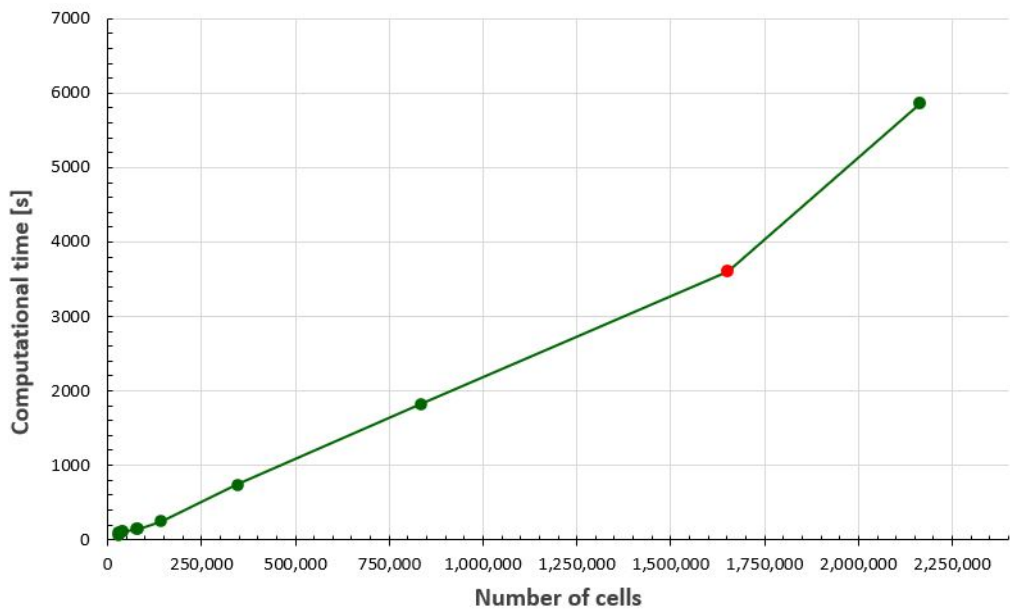


Figure 6.9: Solid bodies added as local mesh
(a) Ref.level = 5, (b) Ref.level = 4



(a)



(b)

Figure 6.10: Plots of the mesh convergence study for perforated support case:
(a) Pressure loss in function of number of elements
(b) Computational time in function of number of elements

6.5 Results

This section aims to show the results of the fluid dynamic simulations of this thesis work's third case. All plots are referred to the three reference planes, which are x-y, x-z and y-z. They are represented in Figure 6.11, Figure 6.12, Figure 6.13 and Figure 6.14 . For this case, it is possible to observe the difference between the cutting planes of filter medium pleats and metallic perforated support. The plane y-z represents the behaviour of the fluid that is passing through the holes particularly well. Finally, the value of pressure loss caused by the presence of the metallic perforated support with the filter medium at 100l/min is:

$$\Delta p_{partIII} = 36.609 \text{ kPa}$$

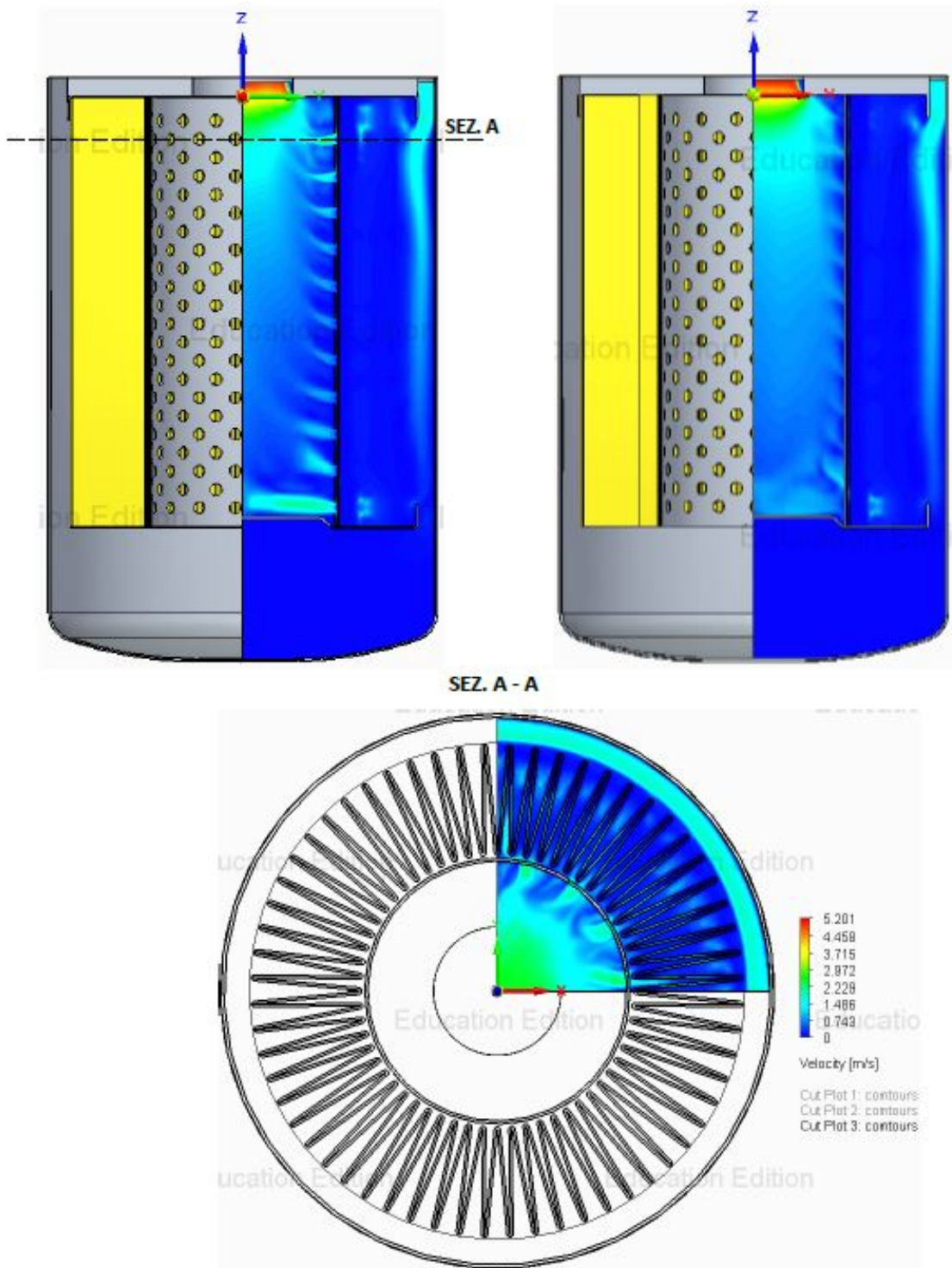


Figure 6.11: Perforated support case velocity gradient cut plot

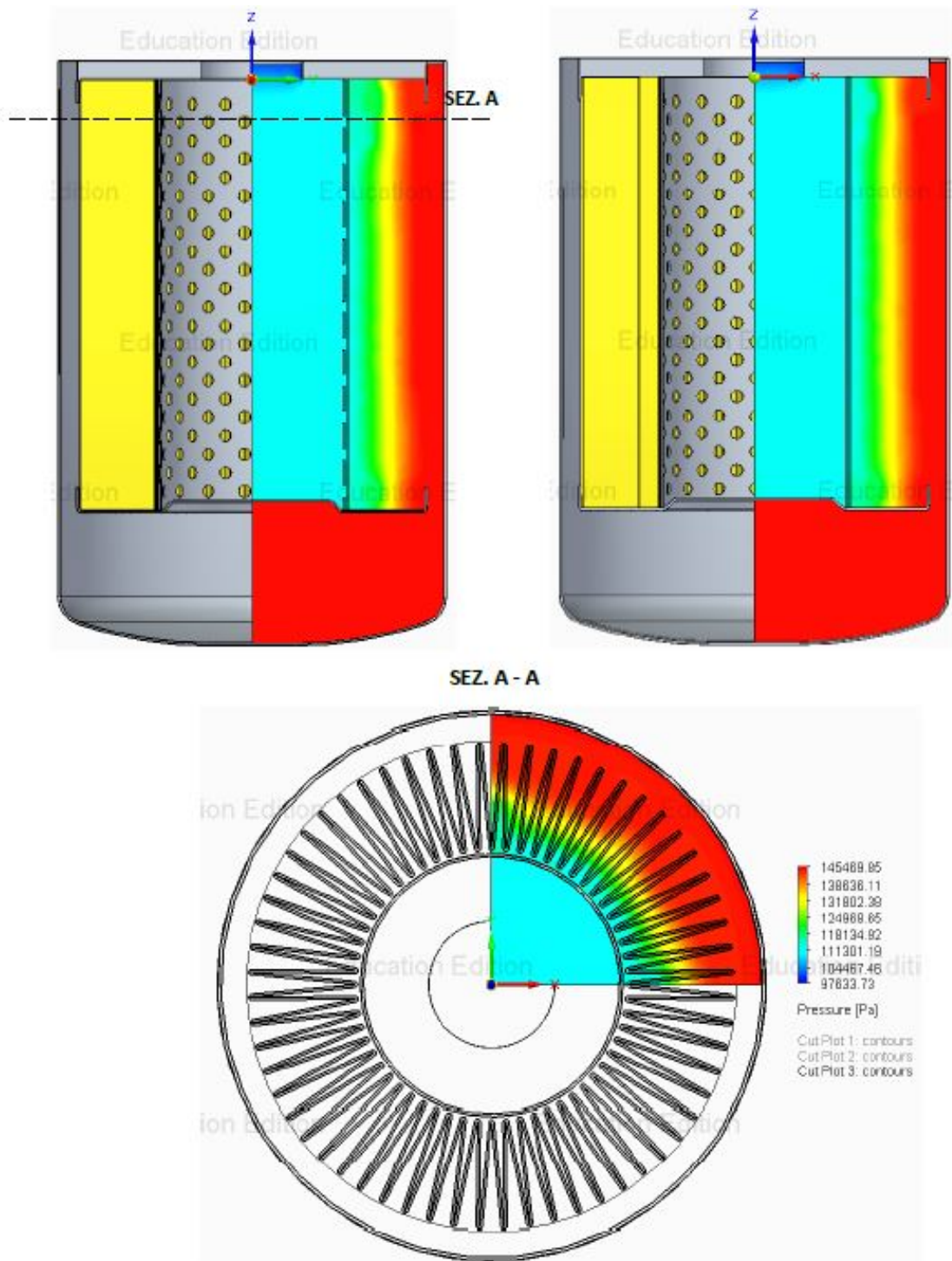


Figure 6.12: Perforated support case pressure gradient cut plot

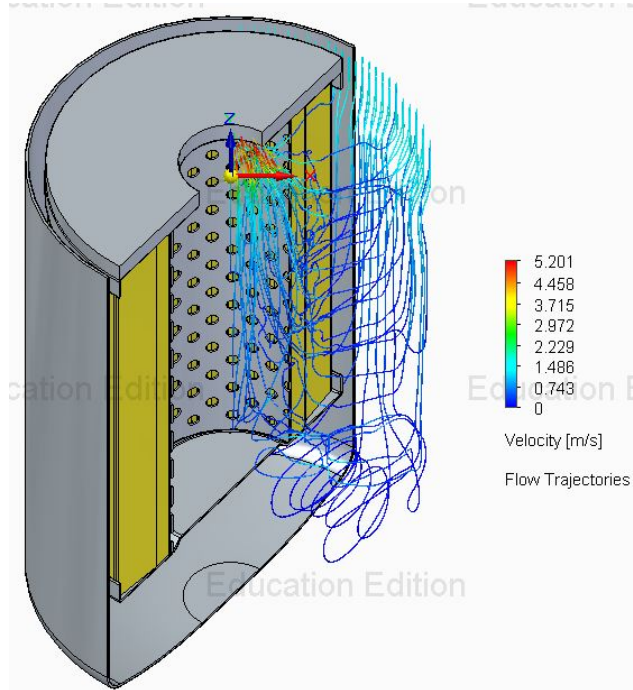


Figure 6.13: Velocity flow trajectories of the perforated support case

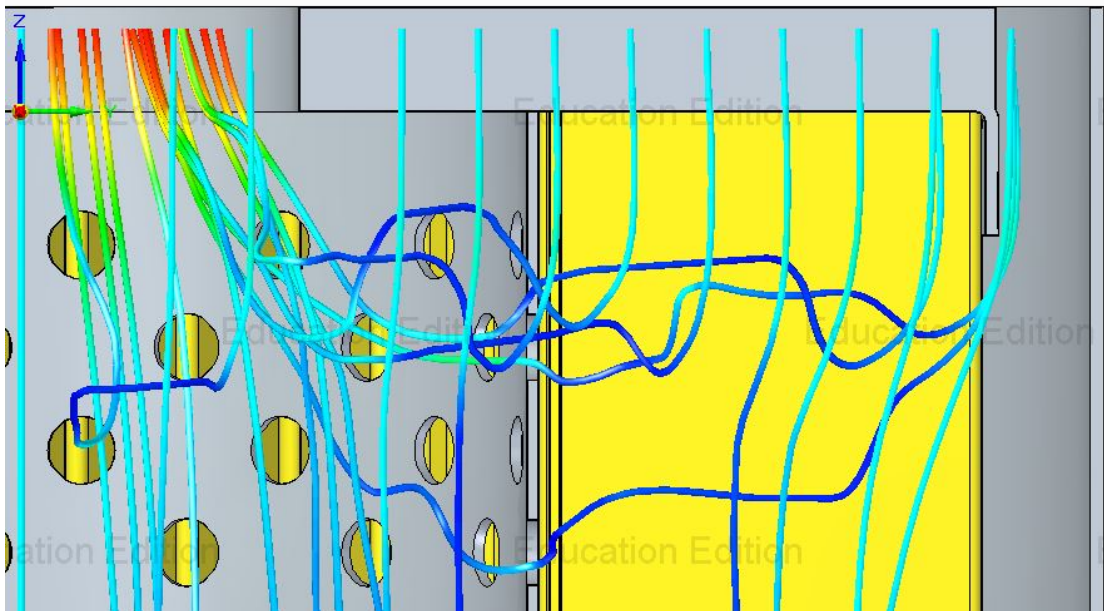


Figure 6.14: Zoom of fluid flow through a hole

Chapter 7

Experimental test equipment

The last part of this thesis work is the validation of the fluid dynamic model of the oil filter. In order to do this, a comparison between the characteristic curve obtained from the chapter 4, chapter 5, chapter 6 and the real characteristic curve is required.

The appropriate equipment and the procedure for evaluating differential pressure versus flow rate characteristics of the chosen hydraulic filter are depicted in this chapter.

7.1 Description

The test bench that the company DELGROSSO S.R.L provides for the experimental tests is named "*Multipass Test Bench*". Its identification data are:

- Manufacturer: SAE IMPIANTI S.R.L.
- Model: BANCO PROVA MULTIPASS
- Serial Number: BPM01
- Year: 2007
- Nominal Power: 47 kW
- Nominal Tension: 400 V
- Frequency: 50 Hz

The construction of the test bench (Figure 7.1) has been realized according to the following desired tests to perform:

- Evaluation of the filter efficiency with the closed circuit filtration method (fluid power filter) according to ISO 16899
- Filtration efficiency and contaminant trap capacity using counting particle (Diesel, fuel and lubrication oil filter for ICE) according to ISO 19438 and ISO 4548/12



Figure 7.1: DELGROSSO S.R.L Multipass Test bench

Two main circuits can be highlighted and taken into account for the experimental tests interested and they are:

1. Circuit S1: $Q = 1 \div 131/\text{min}$
2. Circuit S2: $Q = 13 \div 1301/\text{min}$

As it was mentioned in the first chapters, since the oil filter under discussion, operates with a maximum volumetric flow rate of $Q = 1001/\text{min}$, the circuit S2 is selected to conduct the experimental tests.

7.2 Hydraulic circuit

The functional scheme of the hydraulic circuit of the test bench includes a high number of sub circuits according to their experimental purpose and they are [11]:

- S1
- S2
- Contaminants injection
- Recirculating and Tank emptying
- Particle counter
- Dilution
- Recirculating, load and unload of tank test and contaminants
- Oil storage and cleaning
- Cooling water
- Air tools

Since, the test that will be performed consider the filter medium free of contaminants, only the S2 circuit will be used. Its functional scheme is illustrated in Figure 7.2 and all its components are listed in Table 7.1.

The control unit is installed at the rear of the test bench and include an emergency circuit-breaker in order to secure the equipment in case of maintenance. While on the front of the test bench there is the workstation of the test filters (Figure 7.3). It is equipped with a transparent *lexan* window with a door in order to keep track of the activities, properly filter support to facilitates the installation and an exhaust stainless steel tank. On the side of the workstation, there are all circuit S2 valves.

7.3 Evaluation of experimental characteristics

Before proceeding with the experimental test, the filter test component needs to be set-up inside the workstation and it has to be connected to the selected hydraulic circuit. The provided and analyzed oil filter is represented in Figure 7.4 and it is identical to the simulated one. Since the test bench cannot calculate the pressure drop contribution of each filter part, the experimental test will

S2 CIRCUIT EQUIPMENT		
Item	Description	Model
PIPES	$D_{pipes} = 1''$	-
S2	Tank volume: $Q_1 = 10\text{l} \mid Q_2 = 130\text{l}$	-
P2	Electric gear pump: $Q_{max} = 150\text{l}/\text{min}$	KRACHT KF3/112
TT2	Temperature transducer: $T = -50 \div 500^\circ$	-
TP2	Pressure transducer: $p = 0 \div 2,000\text{ kPa}$	-
TDP2	Diff. Pressure transducer: $p = 0 \div 1,000\text{ kPa}$	-
MR2	Flow rate meter: $Q = 1 \div 250\text{l}/\text{min}$	KRACHT VC5 F1PS
RM2	Regulator Valve	-
RM4	Regulator Valve	-
SC2	Heat Exchanger	ALFALAVAL DOC27-50H
VM2	Liquid sampling point	-
VM4	Liquid sampling point	-
YV10	Three-way valve	-
YV11	Three-way valve	-
YV13	Three-way valve	-

Table 7.1: Components of the hydraulic circuit S2

be performed considering three oil filters with the same filter media but different metal threaded plate and another with an empty oil filter (without a filter medium). Thanks to the empty filter, it is possible to minimize (not to completely reset) the extra pressure loss due to the hydraulic circuit, because the upstream and downstream pressure transducers are located afar from the test filter and are not directly connected to it. In particular, the assessments of the pressure drop through the Multipass test bench is carried out considering the following filters:

- Empty Oil Filter $8 \times 10\text{ mm}$
- Oil Filter $8 \times 6\text{ mm}$
- Oil Filter $8 \times 8\text{ mm}$
- Oil Filter $8 \times 10\text{ mm}$

All measurements are carried out according to the test normative ISO 3968 with the following operating points:

- Working fluid: ASF 41
- Working temperature: 38°

- Viscosity: 15 cSt

Once the installation of the filter test is done, the experimental tests can start.



Figure 7.3: Filter test workstation



Figure 7.4: Experimental Oil Filter

7.3.1 Procedure

The procedure used to carry out the measurements is described below.

- Step 1: Choose the suitable connector for the filter interface
- Step 2: Screw the nipple with the correct thread dimension
- Step 3: Screw the test filter
- Step 4: Close the relief valve
- Step 5: Start the software
- Step 6: Start the flushing within the filter for about 120 s
- Step 7: During the flushing process, open the relief valve in order to release all of the air
- Step 8: Stop the flushing
- Step 9: Verify the following valves: RM4 open, S4/S5 needs to be selected and the relief valve has to be closed
- Step 10: Start the test
- Step 11: Stop when the test is concluded
- Step 12: Extract the results from the software

As it was previously mentioned, the differential pressure upstream and downstream of the filter under test is measured through a differential pressure transducer (TDP2), while the flow rate with a flow rate meter (MR2). On one hand, the data contribution of the empty filter is subtracted from the full filter data. On the other hand, the simulated curve that represents the entire oil filter is obtained by considering the superposition principle, which means:

$$\Delta p_{tot} = \Delta p_{partI} + \Delta p_{partIII}$$

7.4 Data analysis

Figure 7.5, Figure 7.6 and Figure 7.7 show the differential pressure versus volume flow rate characteristic evaluated from the experimental tests. It is possible to compare the experimental curves with the simulated ones in order to evaluate the quality of the computational fluid dynamic simulations. These curves are:

- Pressure drop vs Volume flow rate. Experimental (8×6 mm) vs simulated (8×6 mm) characteristic in Figure 7.8
- Pressure drop vs Volume flow rate. Experimental (8×8 mm) vs simulated (8×8 mm) characteristic in Figure 7.9
- Pressure drop vs Volume flow rate. Experimental (8×10 mm) vs simulated (8×10 mm) characteristic in Figure 7.10
- Pressure Drop vs Hole diameter. Experimental vs simulated characteristic in Figure 7.11 and Figure 7.12 as a percentage

Figure 7.8 shows the comparison of the data obtained from the experiments with the simulated one of the 8×6 mm case. There is a specific value of the flow rate, around 50 l/min, at which the value of the pressure drop of the simulated case goes from overestimated to underestimated in regards to the experimental case. This particular behaviour can be due to the fact that the gradient velocity at high volume flow rates is more relevant, therefore the turbulent effects have a higher impact on the pressure drop characteristic, this is especially true in a real case scenario where other aspects can influence the results.

In Figure 7.9 (8×8 mm case) and Figure 7.10 (8×10 mm case) the pressure loss is always overestimated and the curves are not completely parabolic. The reason for this is the fact that in these cases the gradient velocity is lower and the turbulence effect is not as relevant, however the laminar behaviour prevails. Figure 7.11 shows a comparison between the simulated and experimental curves for the diameter parametric study. In fact, in this figure the three different cases can be clearly seen, in particular for the 8×8 mm case and 8×10 mm case where the trend of the experimental data is the same as the simulated one with a constant pressure differential (overestimated).

The overestimation of Δp can happen for different reasons, such as:

- The utilization of a different perforated metal support as it empirically has a lower pressure drop
- The slight geometrical difference of the cartridge model
- The possibility of different number of folds (60 ± 3)

- The fact that the pressure transducers cannot immediately measure the pressure drop upstream and downstream the test filter
- The possibility to have slight chemical and physical differences of the working fluid
- The smaller outflow area due to the presence of the nipple
- The non perfect accuracy and repeat-ability of the test bench
- The non perfect accuracy of the CFD simulations because of the high number of approximations

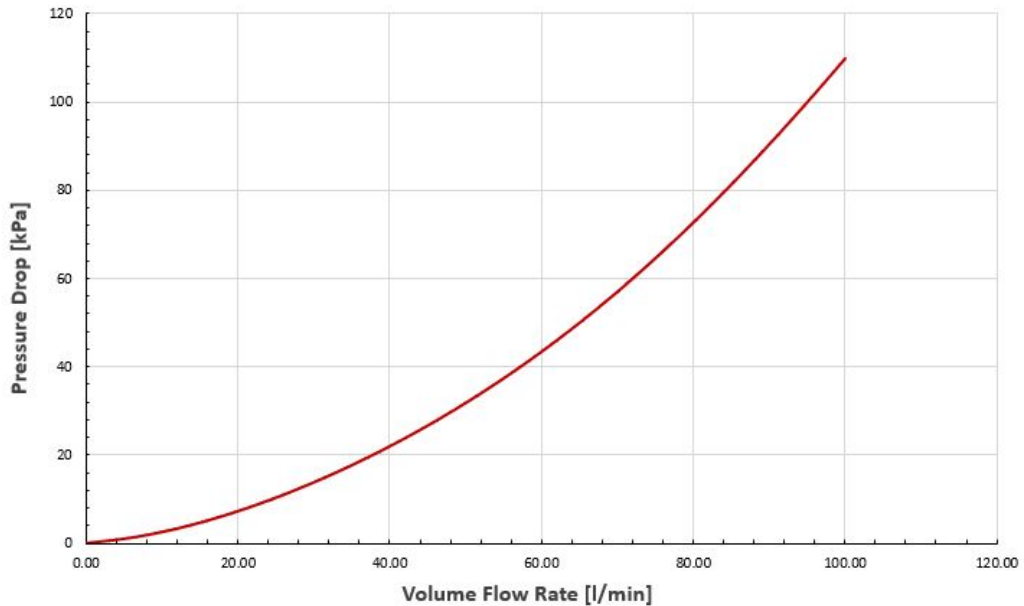


Figure 7.5: Filter 8×6 mm experimental curve

Figure 7.13 shows a comparison between the experimental and simulated data on a pressure drop vs velocity graph. Moreover, the abscissa represents the single hole local velocity. From this graph, it can be possible to observe how the simulation data passes at a certain point from an overestimation to an underestimation due to the reasons previously mentioned. Therefore, the graph may be used as a starting design rule for future filters, by considering only the safety region, i.e. the area in which the simulation data are higher than the experimental one.

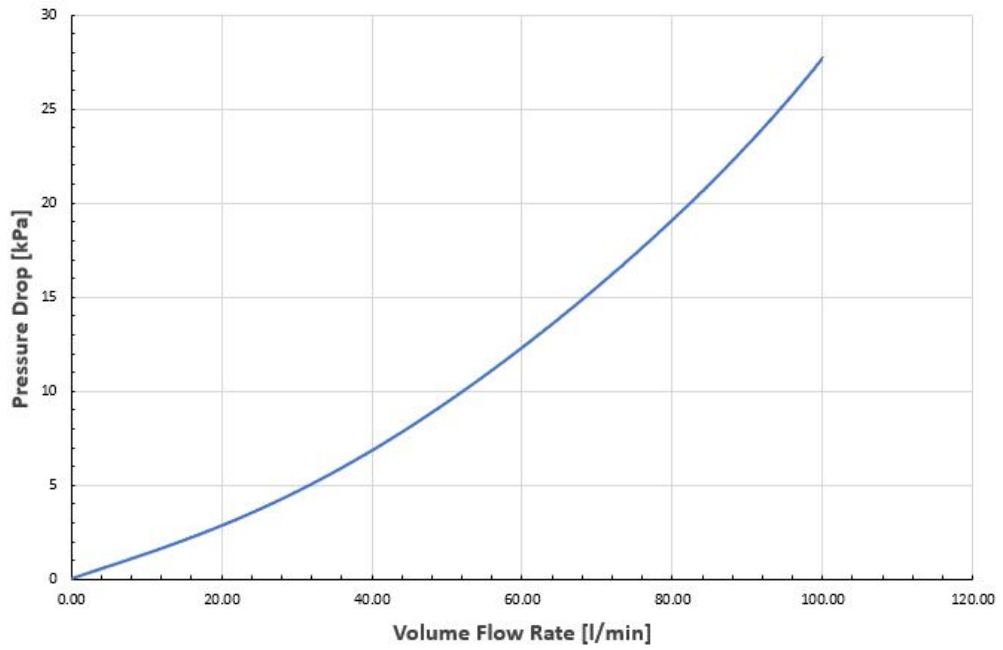


Figure 7.6: Filter 8 x 8 mm experimental curve

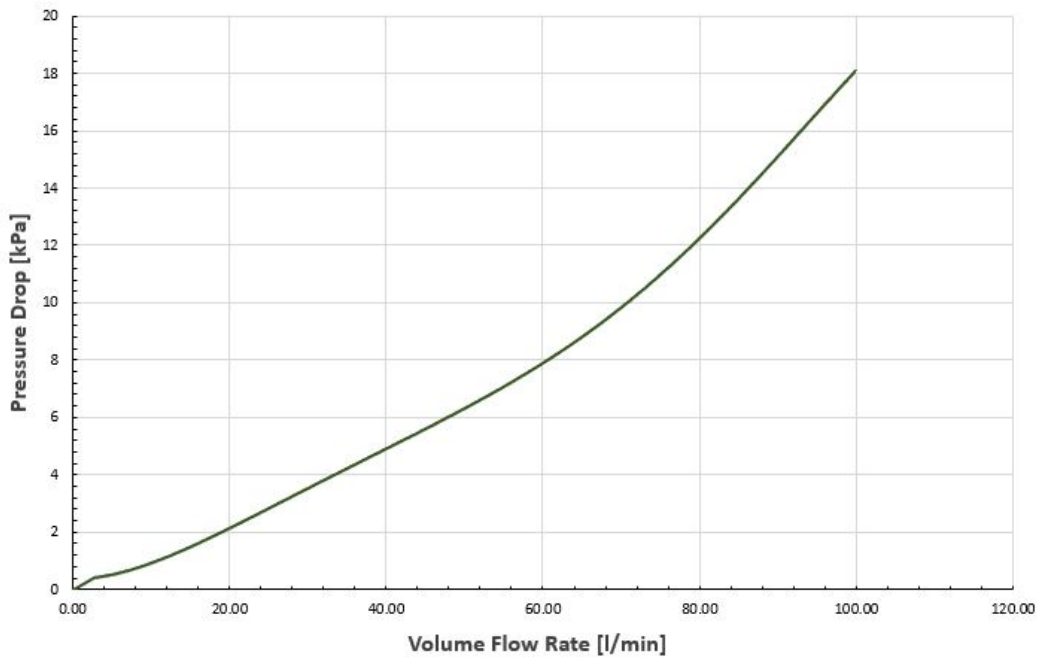


Figure 7.7: Filter 8 x 10 mm experimental curve

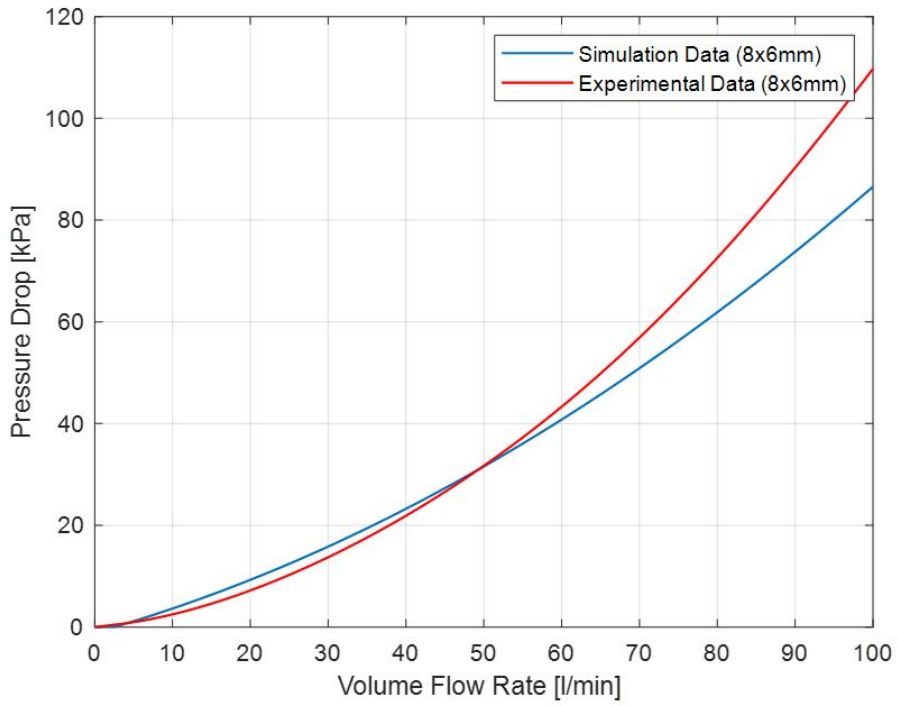


Figure 7.8: Experimental data vs Simulated data of filter 8 × 6 mm

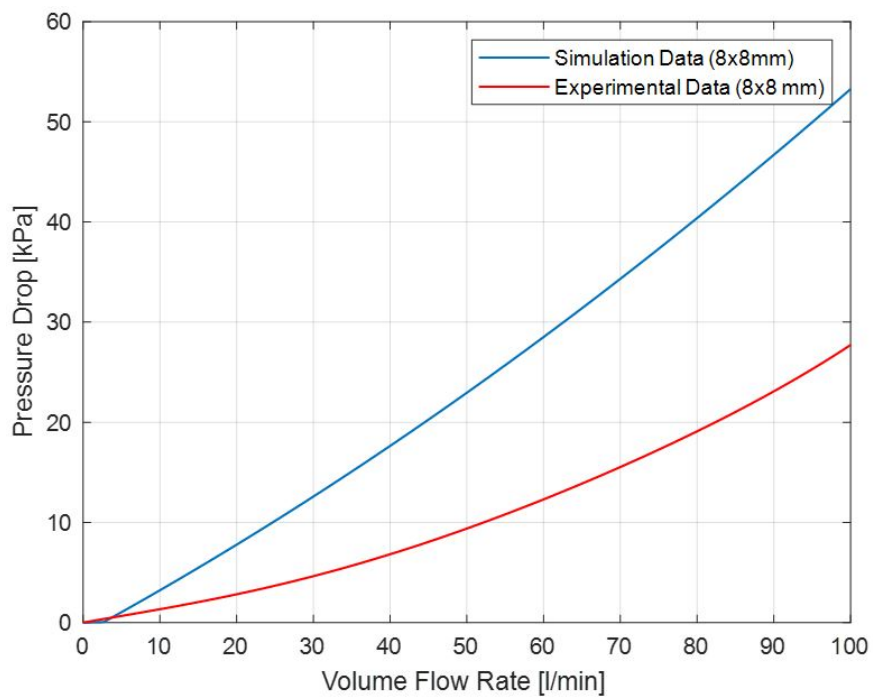


Figure 7.9: Experimental data vs Simulated data of filter 8 × 8 mm

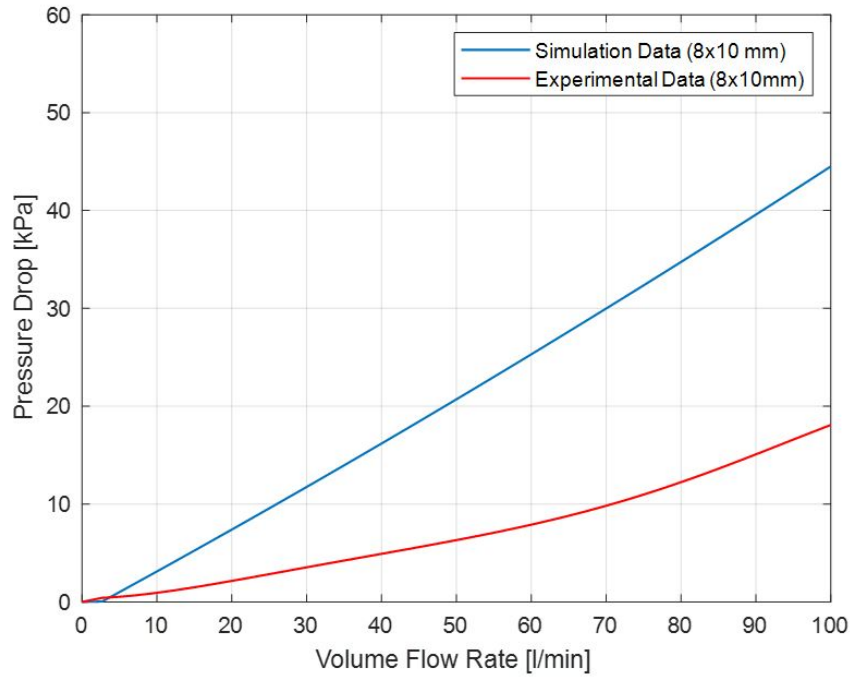


Figure 7.10: Experimental data vs Simulated data of filter 8×10 mm

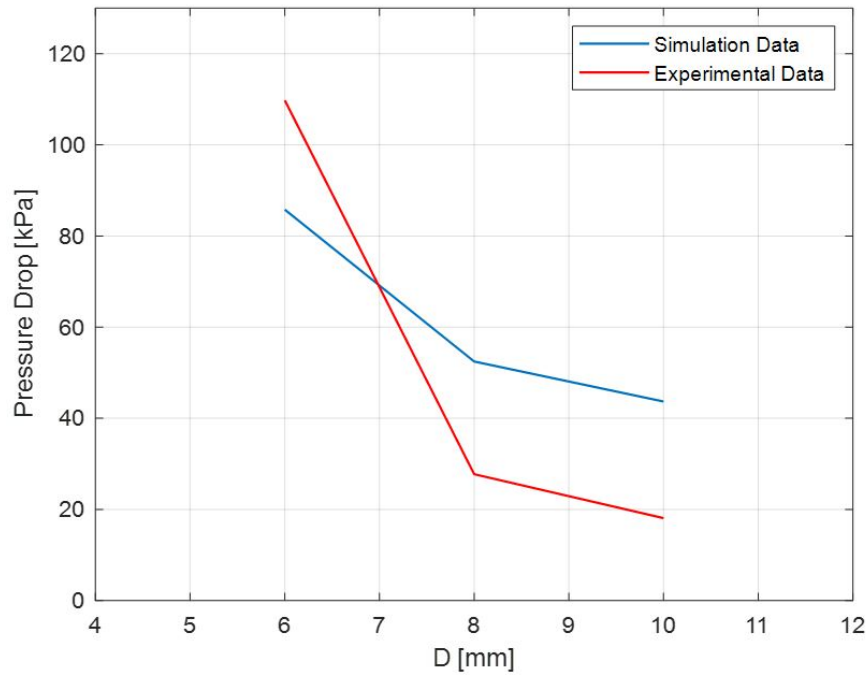


Figure 7.11: Parametric comparison between experimental and simulated data at 100l/min

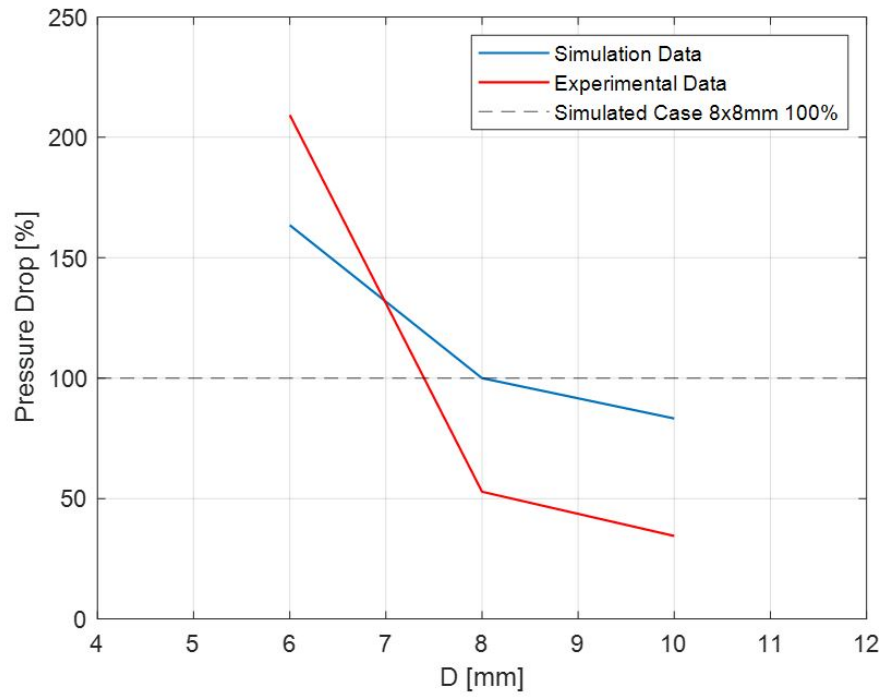


Figure 7.12: Parametric comparison between experimental and simulated data as a percentage

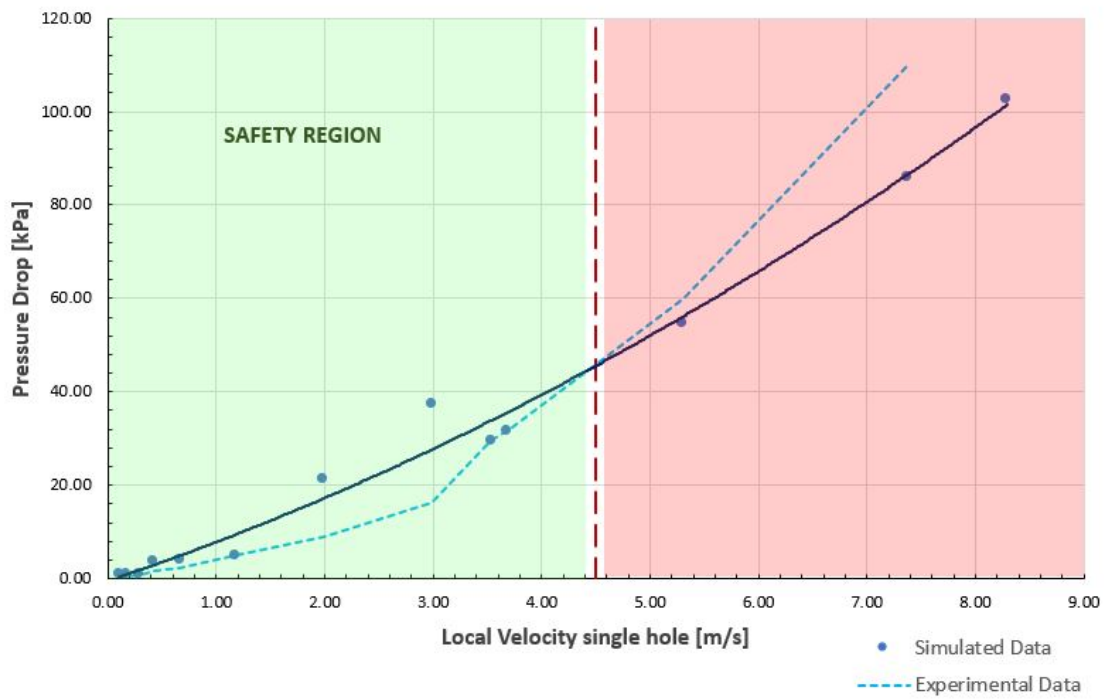


Figure 7.13: Pressure drop vs velocity of a single hole plot

Chapter 8

Conclusions

In this thesis work, an in-depth study was carried out on the filtration process inside an oil filter provided by DELGROSSO S.R.L, developing a fluid-dynamics simulation model by varying some parameters of the component's geometry. The component's modelling was divided in three parts because of its complexity. First and foremost the CFD model of the head filter has been realized in order to estimate the pressure loss due to the different diameters of the inlet holes. Secondly, the cartridge model was made and the last part was a cartridge model with the perforated metal support included. Several challenges were encountered and overcome during the development of this work. The hardest one was to deal with the lacking knowledge of the parameters that describe the filter medium behaviour. In order to solve this problem, a measurement device, called *permeabilimeter*, has been designed and realized. The developed simulation model provided particularly interesting results, which allowed to better understand the fluid dynamic phenomenon and the influence of parameters such as the diameter and the number of inlet holes of the oil filter under discussion. The experimental tests show that the pressure drop is slightly lower than the theoretical one, this development is influenced by: the complex geometry of the real component, the issues of the test bench that do not take into account the hydraulic head loss, by the slightly different real cartridge due to the production errors and by the limited computational power resources. It is pretty obvious that the accuracy of the results is limited by the approximations that have been made and by the software used. However, since the obtained results tend to overestimate the real value of pressure drop, they can be used as a starting design rule for future oil filters. Future developments of this work could be the simulation of the entire component, the heat effects, a parametric study of the working fluid viscosity and a microscopic particle study of the contaminants inside the filter medium.

Appendix A

Operating fluid properties: AeroShell Fluid 41

AEROSHELL HYDRAULIC FLUIDS

AEROSHELL FLUID 41

AeroShell Fluid 41 is a mineral hydraulic oil manufactured to a very high level of cleanliness, and possesses improved fluid properties. AeroShell Fluid 41 contains additives which provide good low temperature fluidity, anti-wear, oxidation-corrosion inhibition and shear stability. In addition metal de-activators and foam inhibitors are included in this high viscosity index fluid to enhance performance in hydraulic applications. AeroShell Fluid 41 is capable of wide temperature range operation.

AeroShell Fluid 41 is dyed red.

APPLICATIONS

AeroShell Fluid 41 is intended as a hydraulic fluid in all modern aircraft applications requiring a mineral hydraulic fluid. AeroShell Fluid 41 is particularly recommended where use of a "superclean" fluid can contribute to improvements in component reliability, and can be used in aircraft systems operating unpressurised between -54°C to 90°C (-65°F to 194°F) and pressurised between -54°C to 135°C (-65°F to 275°F).

AeroShell Fluid 41 should be used in systems with synthetic rubber components and must not be used in systems incorporating natural rubber. Refer to the General Notes at the front of this section for further information.

AeroShell Fluid 41 is compatible with AeroShell Fluids 4, 31, 61 and LGF.

Chlorinated solvents should not be used for cleaning hydraulic components which use AeroShell Fluid 41. The residual solvent contaminates the hydraulic fluid and may lead to corrosion.

Due to its properties, it is also used in several industrial applications.

SPECIFICATIONS

U.S.	Approved MIL-PRF-5606J
British	Approved DEF STAN 91-048 Grade Superclean* (European production only) Meets DEF STAN 91-048 Grade Normal (European production only) Equivalent to DEF STAN 91-048 Grades Superclean* & Normal (U.S. production only)
French	Approved DCSEA 415/A
Russian	Analogue to AMG-10
NATO Code	H-515* (equivalent H-520 (Obsolete))
Joint Service Designation	OM15* (equivalent OM-18)
COMAC	Approved QPL-CMS-OL-104

*Superclean grades

The British specification DEF STAN 91-048 covers two grades (normal and superclean) of mineral hydraulic fluid which differ only in their cleanliness limits. AeroShell Fluid 41 is manufactured to meet the superclean requirements and thus it also meets the requirements of the normal grade.

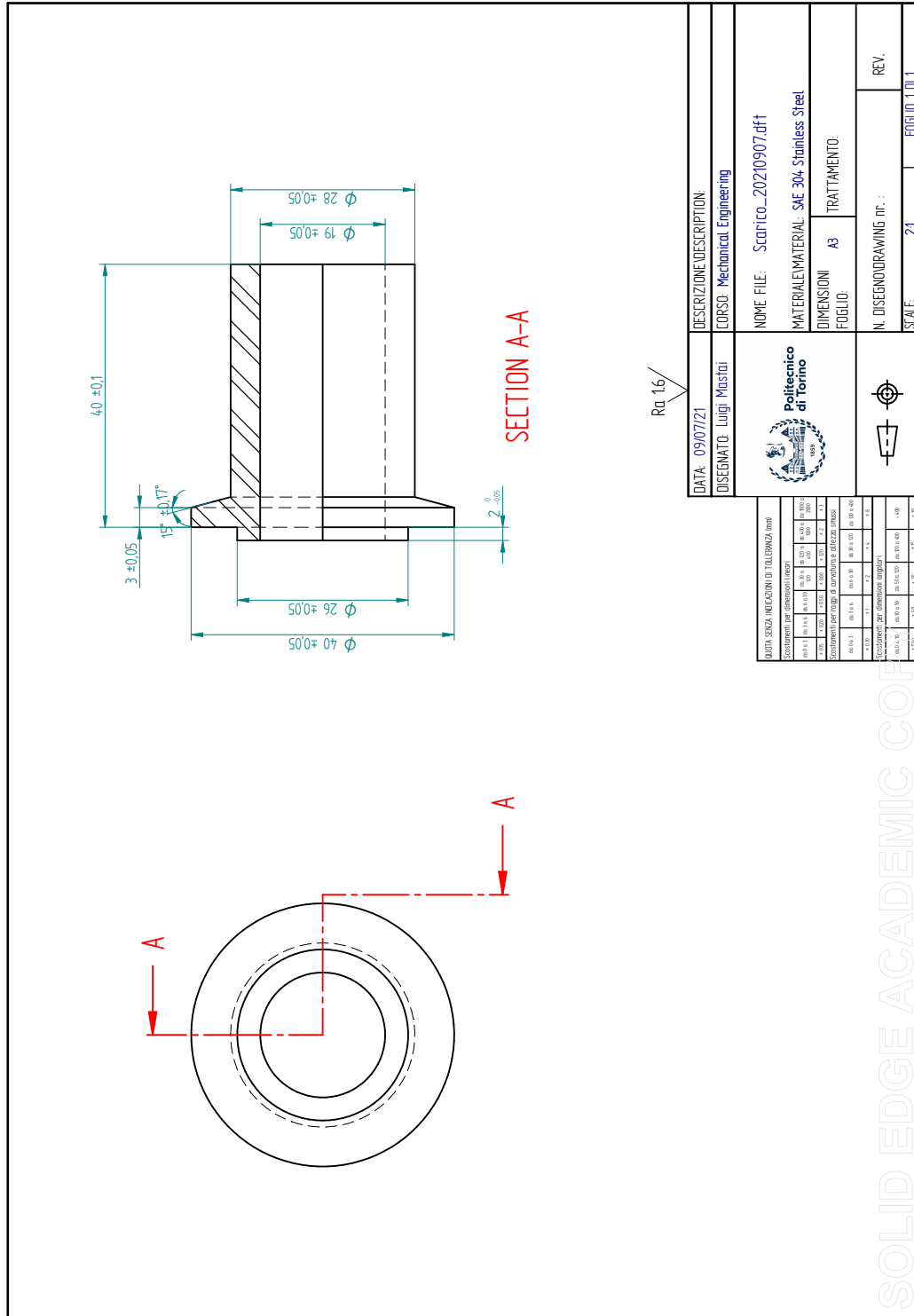
AEROSHELL HYDRAULIC FLUIDS

PROPERTIES	MIL-PRF-5606J	TYPICAL
Oil type	Mineral	Mineral
Kinematic viscosity	mm ² /s	
@ 100°C (212°F)	4.90 min	4.9 - 5.30
@ 40°C (104°F)	13.2 min	13.2 - 14.3
@ -40°C (-40°F)	600 max	460 - 600
@ -54°C (-65°F)	2500 max	2200 - 2500
Flashpoint	°C (°F)	
	82 (179) min	90 - 95 (194 - 203)
Pourpoint	°C (°F)	
	-60 (-76) max	-60 (-76) max
Total acid number	mgKOH/g	
	0.20 max	0.02 - 0.05
Evaporation loss 6 hrs		
@ 71°C (160°F)	%m	
	20 max	10 - 15.4
Water content	ppm	
	100 max	50 - 75
Relative density @ 15.6°C (60°F)	Report	0.868 - 0.873
Colour	Red	Red
Particle contamination, number of particles per 100ml in size range		
5 to 15 µm	8000 max	1200 max
16 to 25 µm	1425 max	1425 max
26 to 50 µm	253 max	253 max
51 to 100 µm	45 max	45 max
over 100 µm	8 max	8 max
Particle count	5	5 max
Copper corrosion	2e max	2b
Steel on steel wear scar diam	mm	
	1.0 max	0.6 - 0.95
Rubber swell, L rubber		
168 hrs @ 70°C (158°F)	%	
	19 to 30	Passes
Low temperature stability		
72hrs @ -54°C (-65°F)	Must pass	Passes
Gravimetric analysis	mg/100ml	
	1.0 max	Passes
Foaming tendency	Must pass	Passes
Barium content	ppm	
	10 max	Nil

A viscosity/temperature curve is shown at the end of this section.

Appendix B

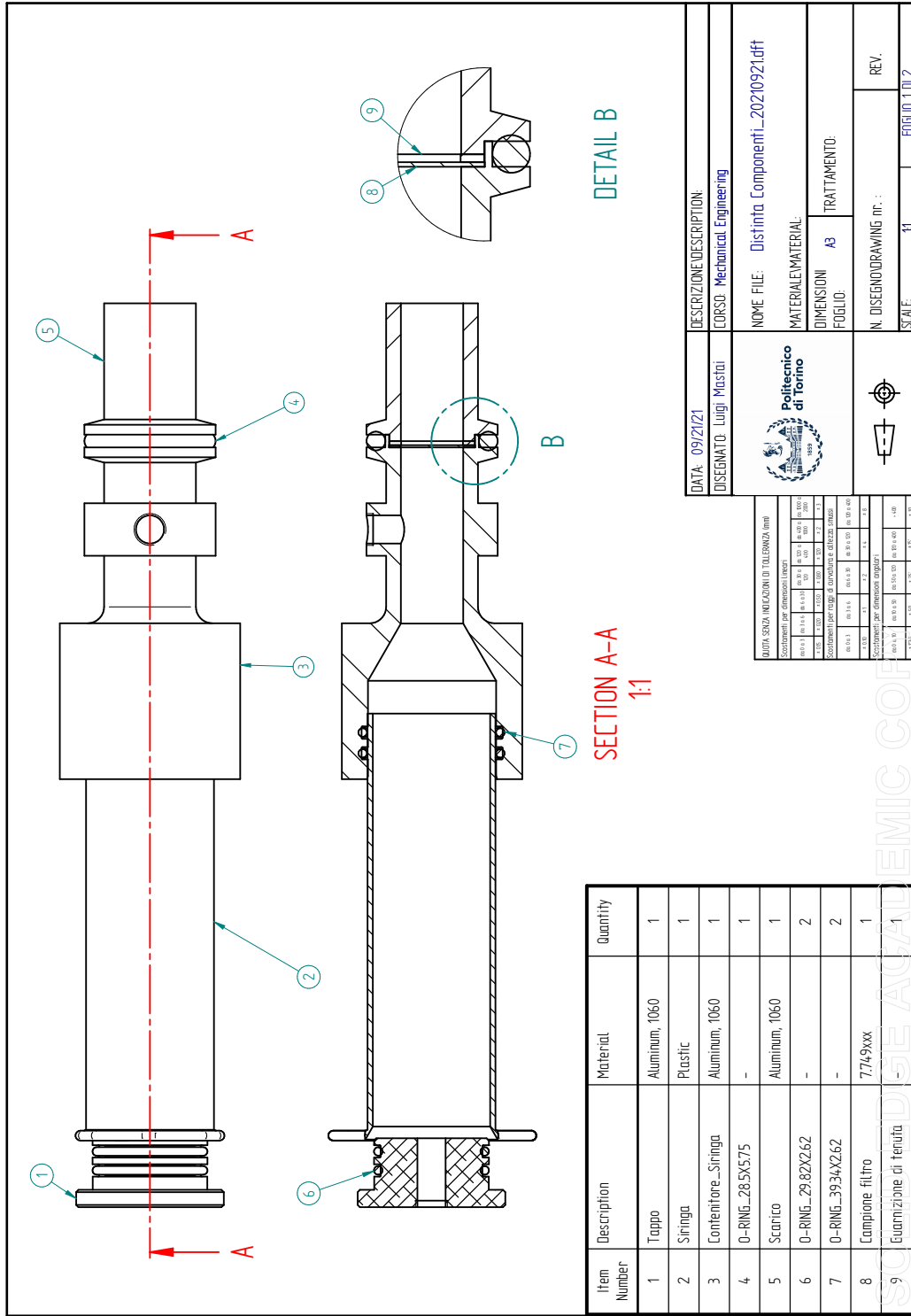
Permeabilimeter: Technical drawings



DATA: 09/07/21	DESCRIZIONE/DESCRIPTION:
DISEGNATO: Luigi Mastoi	CORSO: Mechanical Engineering
 Politecnico di Torino	
NOME FILE: Scario_20210907.dft	MATERIALE/MATERIAL: SAE 304 Stainless Steel
DIMENSIONI	TRATTAMENTO:
FOLIO:	A3
N. DISEGNO/DRAWING nr.:	REV.
SCALE: 2:1	FOLIO: 1 DI 1

DATI SCELTI IN FUNZIONE DI TOLLERANZE (mm)	
Scostamenti per dimensioni (mm)	
h6/h7	0.005
H7/g6	0.005
H7/g7	0.005
H7/g8	0.005
H7/g9	0.005
H7/g10	0.005
H7/g11	0.005
H7/g12	0.005
H7/g13	0.005
H7/g14	0.005
H7/g15	0.005
H7/g16	0.005
H7/g17	0.005
H7/g18	0.005
H7/g19	0.005
H7/g20	0.005
H7/g21	0.005
H7/g22	0.005
H7/g23	0.005
H7/g24	0.005
H7/g25	0.005
H7/g26	0.005
H7/g27	0.005
H7/g28	0.005
H7/g29	0.005
H7/g30	0.005
H7/g31	0.005
H7/g32	0.005
H7/g33	0.005
H7/g34	0.005
H7/g35	0.005
H7/g36	0.005
H7/g37	0.005
H7/g38	0.005
H7/g39	0.005
H7/g40	0.005
H7/g41	0.005
H7/g42	0.005
H7/g43	0.005
H7/g44	0.005
H7/g45	0.005
H7/g46	0.005
H7/g47	0.005
H7/g48	0.005
H7/g49	0.005
H7/g50	0.005
H7/g51	0.005
H7/g52	0.005
H7/g53	0.005
H7/g54	0.005
H7/g55	0.005
H7/g56	0.005
H7/g57	0.005
H7/g58	0.005
H7/g59	0.005
H7/g60	0.005
H7/g61	0.005
H7/g62	0.005
H7/g63	0.005
H7/g64	0.005
H7/g65	0.005
H7/g66	0.005
H7/g67	0.005
H7/g68	0.005
H7/g69	0.005
H7/g70	0.005
H7/g71	0.005
H7/g72	0.005
H7/g73	0.005
H7/g74	0.005
H7/g75	0.005
H7/g76	0.005
H7/g77	0.005
H7/g78	0.005
H7/g79	0.005
H7/g80	0.005
H7/g81	0.005
H7/g82	0.005
H7/g83	0.005
H7/g84	0.005
H7/g85	0.005
H7/g86	0.005
H7/g87	0.005
H7/g88	0.005
H7/g89	0.005
H7/g90	0.005
H7/g91	0.005
H7/g92	0.005
H7/g93	0.005
H7/g94	0.005
H7/g95	0.005
H7/g96	0.005
H7/g97	0.005
H7/g98	0.005
H7/g99	0.005
H7/g100	0.005

SOLID EDGE ACADEMIC COPY



Item Number	Description	Material	Quantity
1	Tappo	Aluminum, 1060	1
2	Siringa	Plastic	1
3	Contenitore_Siringa	Aluminum, 1060	1
4	O-RING_28,5X5,75	-	1
5	Scartico	Aluminum, 1060	1
6	O-RING_29,82X2,62	-	2
7	O-RING_39,34X2,62	-	2
8	Componente filtro	7,749xxx	1
9	Guarnizione di tenuta	-	1

QUOTA SINGOLA INDICAZIONI DI TOLLERANZE (mm)

Scostamenti per dimensioni (mm)

0-0,25	0,12	0,25	0,50	0,75	1,00	1,50	2,00	3,00	4,00	5,00	6,00	8,00	10,00	12,00	15,00	20,00	30,00	40,00	50,00	60,00	80,00	100,00	
±0,012	±0,015	±0,020	±0,025	±0,030	±0,035	±0,045	±0,050	±0,060	±0,070	±0,080	±0,090	±0,100	±0,120	±0,150	±0,180	±0,220	±0,280	±0,350	±0,450	±0,550	±0,700	±0,900	±1,100

Scostamenti per forme e posizioni (mm)

0-0,25	0,25-0,50	0,50-1,00	1,00-1,50	1,50-2,00	2,00-3,00	3,00-4,00	4,00-6,00	6,00-10,00	10,00-15,00	15,00-20,00	20,00-30,00	30,00-50,00	50,00-80,00	80,00-120,00	120,00-180,00	180,00-250,00	250,00-350,00	350,00-500,00	500,00-700,00	700,00-1000,00
±0,010	±0,012	±0,015	±0,020	±0,025	±0,030	±0,035	±0,045	±0,055	±0,065	±0,080	±0,100	±0,120	±0,150	±0,180	±0,220	±0,280	±0,350	±0,450	±0,550	±0,700

DATA: 09/21/21	DESCRIZIONE/DESCRIPTION:
DISEGNATO: Luigi Mastoi	CORSO: Mechanical Engineering
	
NOME FILE: Distinta Componenti_20210921.dff	
MATERIALE/MATERIAL:	
DIMENSIONI	FOLIO: A3
TRATTAMENTO:	
N. DISEGNO/DRAWING nr.:	
SCALE: 1:1	REV.:
FOGLIO 1 DI 2	

Appendix C

How to import porosity and permeability parameters to FloEFD

This appendix wants to show the procedure that has been followed for the simulation of the filter element. The work has been performed by using both Solid-Edge for the CAD model and FloEFD for the CFD simulations. It is sufficient to click on *conditions* and select the option *Porous Medium* (Figure C.1). After that, the solid body has to be selected on the *porous medium window* and subsequently the *Create/Edit* option has to be clicked (Figure C.2). Once the *Engineering Database* window is opened, click on *Porous media > User defined*, right-click on a blank space under in the item window and select *New Item*. Finally, it is possible to import all filter media parameters, the *Length* and *Area* values need to be the same as the ones used in the specific sample in chapter 5. The resistance calculation formula has to be "Pressure Drop, Flow rate, Dimensions" (Figure C.3), After that, "Pressure Drop vs Flow rate" has to be clicked (Figure C.4), this will open a table in which the values can be manually inputted. Once that is done, the simulation can start.

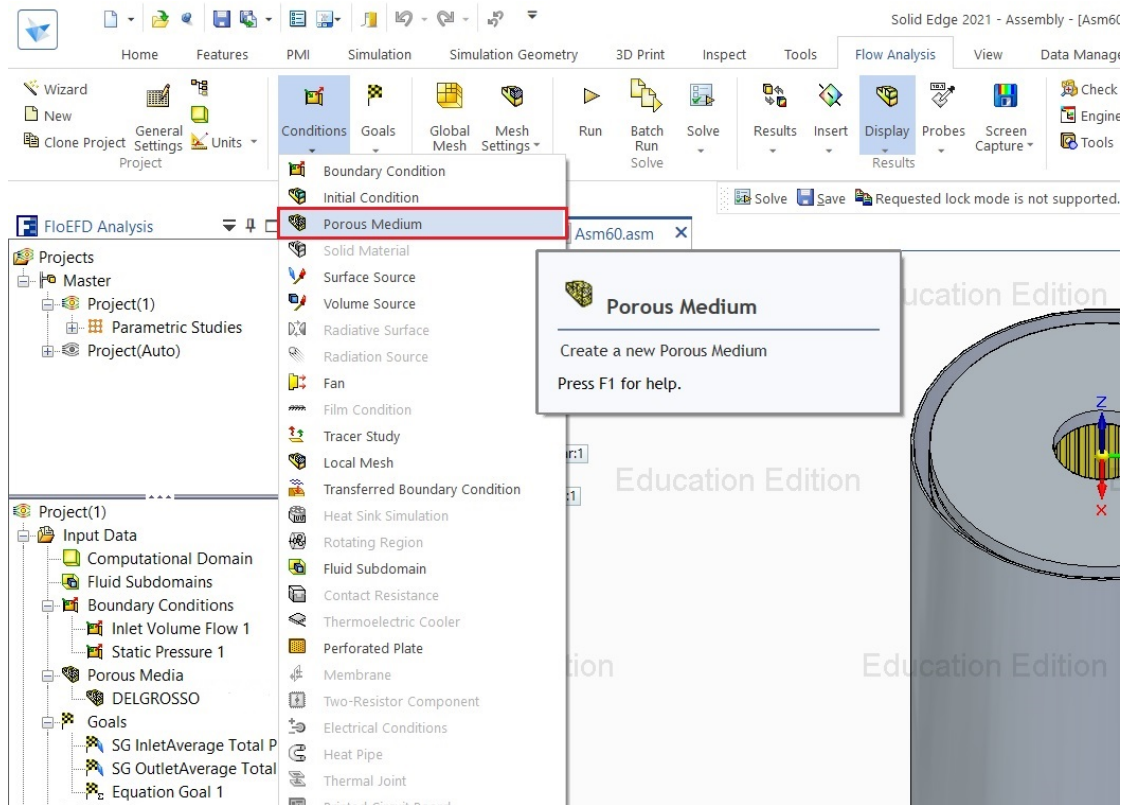


Figure C.1: Insert Porous Medium condition tool

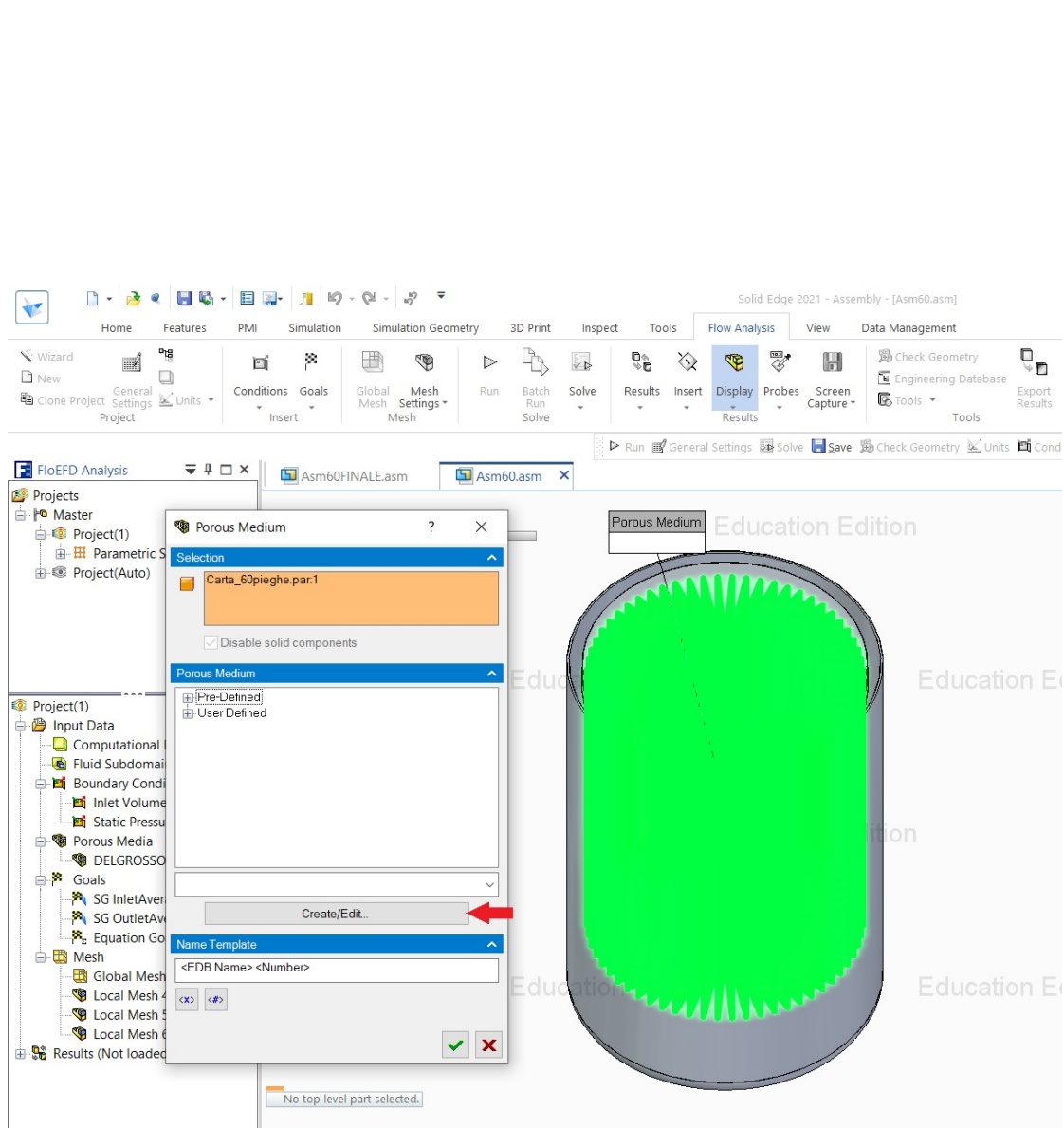


Figure C.2: Porous media: Create/Edit tool

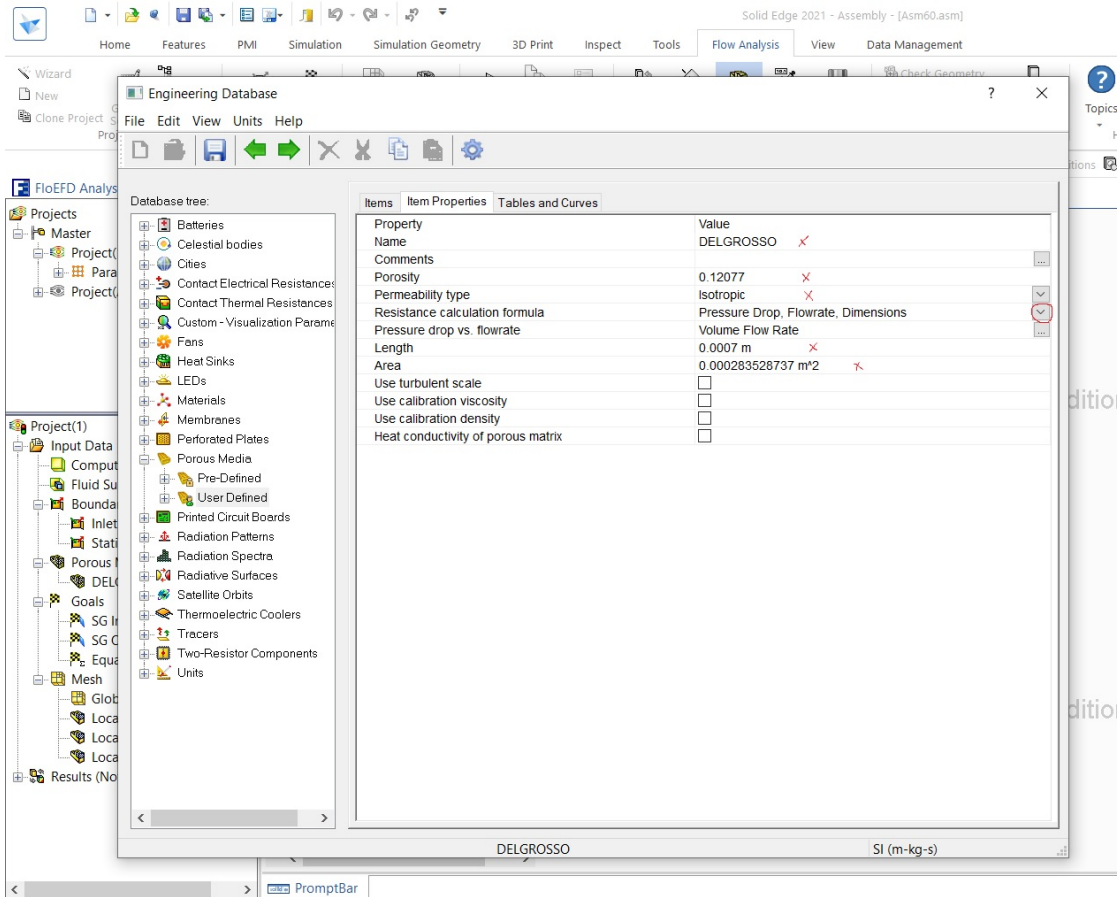


Figure C.3: Porous media: Inserting parameters

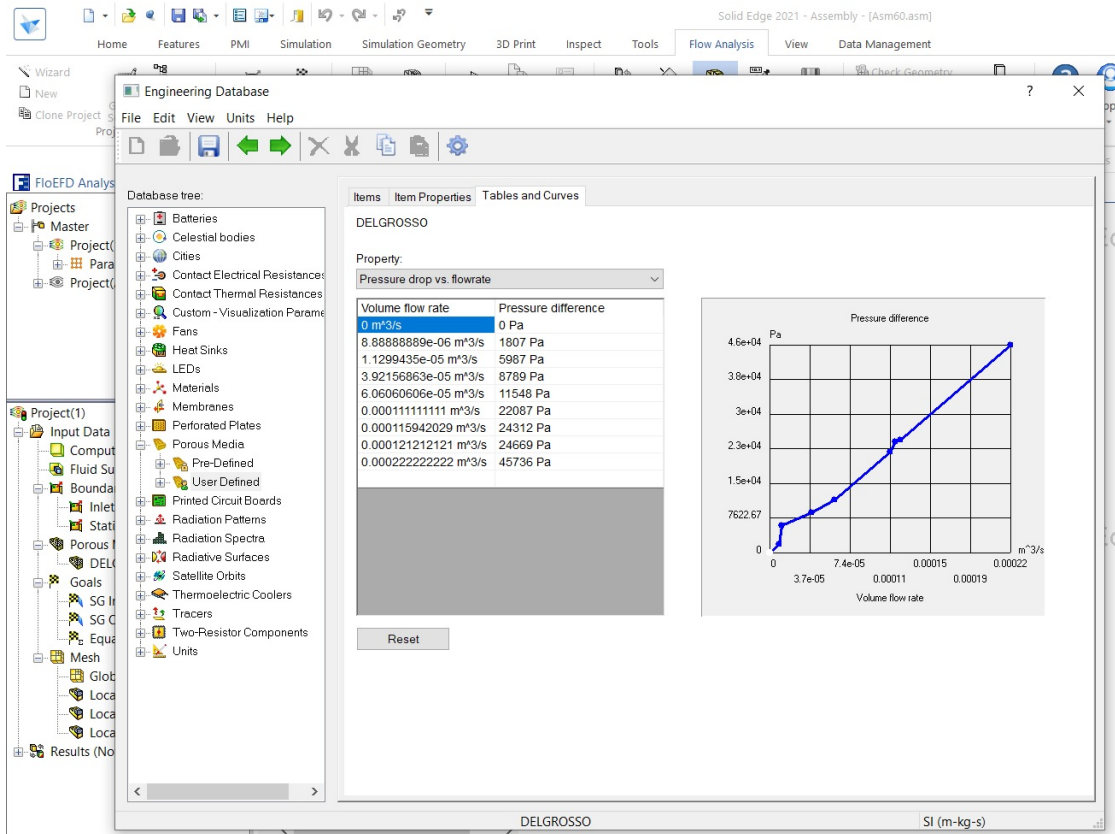


Figure C.4: Porous media: Inserting permeability curve

Bibliography

- [1] Ken Sutherland. *Filters and Filtration Handbook*. Linacre House, Jordan Hill, Oxford OX2 8DP, UK 30 Corporate Drive, Suite 400, Burlington, MA 01803, USA: Butterworth-Heinemann, 2008 (cit. on pp. 1, 5, 6).
- [2] *Hydraulic Filtration Product Guide*. Donaldson Filtration Solution (cit. on p. 2).
- [3] *Hydraulic Filtration Products*. MPFILTRI (cit. on pp. 3, 4).
- [4] Shell Aviation. *The Aeroshell Book*. Ed. by © 2021 Shell International Petroleum Company Limited. Twentieth. www.shell.com/aviation, 2021 (cit. on p. 10).
- [5] W. Malalasekera H. K. Versteeg. *An introduction to computational fluid dynamics. The finite volume method*. Longman House, Burnt Mill, Harlow Essex CM20 2JE, England: Longman Scientific & Technical, 1995 (cit. on p. 12).
- [6] Richard H. Pletcher John C. Tannehill Dale A. Anderson. *Computational Fluid Mechanics and Heat Transfer*. Ed. by Carol Edwards Christine Williams. Second. 1101 Vermont Avenue, NW, Suite 200 Washington, DC 20005-3521: Taylor&Francis, 1997 (cit. on p. 13).
- [7] *FloEFDTM Technical Reference*. Mentor. 2018 (cit. on p. 15).
- [8] Yuanle Ma Zhangxin Chen Guanren Huan. *Computational Methods for Multiphase Flows in Porous Media*. Southern Methodist University, Dallas, Texas, USA: SIAM, 2005 (cit. on p. 15).
- [9] Irwin Hutten. *Handbook of Non-Woven Filter Media*. Elsevier Science & Technology Books, 2007 (cit. on pp. 25, 26, 28, 33).
- [10] T. J. Ptak. «Chapter 4: Gas filtration media». PhD. Columbia Industries, Inc. (cit. on p. 32).
- [11] *Manuale di istruzione per banchi prova Multipass per filtri olio e gasolio*. SAE Impianti S.R.L. 2007 (cit. on p. 82).